PONTIFICIA UNIVERSIDAD CATOLICA DE CHILE

ESCUELA DE INGENIERIA

PERFORMANCE OF PYRAMID WAVEFRONT SENSORS UNDER ELONGATED LASER STAR SPOTS

FRANCISCO ANTONIO OYARZÚN LIRA

Thesis submitted to the Office of Research and Graduate Studies in partial fulfillment of the requirements for the Degree of Master of Science in Engineering

Advisor:
ANDRÉS GUESALAGA

Santiago de Chile, (July, 2022)

PONTIFICIA UNIVERSIDAD CATOLICA DE CHILE
ESCUELA DE INGENIERIA

PERFORMANCE OF PYRAMID WAVEFRONT SENSORS UNDER ELONGATED LASER STAR SPOTS

FRANCISCO ANTONIO OYARZÚN LIRA

Members of the Committee:

ANDRÉS GUESALAGA

CLEMENTINE BECHET

BENOIT NEICHEL

JOSÉ CARDEMIL

Thesis submitted to the Office of Research and Graduate Studies in partial fulfillment of the requirements for the Degree of Master of Science in Engineering

Santiago de Chile, (July, 2022)

To my family, loved ones, friends, and teachers that made me who I am.

ACKNOWLEDGEMENT

Special thanks to Benoit Neichel, Andrés Guesalaga, Thierry Fusco, Vincent Chambouleyron, Jean-Francois Sauvage, Clémentine Béchet, Felipe Pedreros, Camilo Weinberger, and Esther Soria for their guidance in the process of making this thesis.

We thank the Chilean Agency for Research and Development (ANID) for supporting this work (grants Fondecyt 1190186 and Millennium Nucleus ACIP Science Initiative Program - NCN19_161), and the *Laboratoire d'Astrophysique de Marseille* (LAM) for giving me the opportunity to obtain hands-on experience with real adaptive optics equipment.

CONTENTS

LIST OF FIGURES

RESUMEN

En este trabajo se estudia el desempeño de un sensor de frente de onda piramidal para la medición de las distorsiones del frente de onda utilizando como guía una estrella láser (LGS) en telescopios con diametros entre 8 y 40 m. Usando una caja de herramientas de código abierto para Matlab llamada OOMAO se estudiaron ganancias ópticas, linealidad, rango dinámico, sensibilidad y funcionamiento en lazo cerrado de un PWFS y luego se comparó el rendimiento entre una estrella guía natural (NGS) y un LGS. Los resultados indican que para una LGS es posible actualizar la matriz de interacción para optimizar el reconstructor a la estructura dinámica de la capa de sodio, pero la caída de sensibilidad en la LGS puede generar el mismo efecto en SNR que bajar el brillo de una NGS hasta 5 magnitudes. Finalmente, se muestra que es posible cerrar el lazo de control en una LGS con una calibración completa empleando una fuente puntual (como un simulador de telescopio), pero la caída en la sensibilidad necesitaría una LGS brillante, lo que podría no ser factible en la realidad.

Esto sugiere que el sensor de frente de onda piramidal no sería adecuado para la medición de las distorsiones del frente de onda usando LGS para los nuevos telescopios extremadamente grandes.

Palabras clave: AO, óptica adaptativa, sensor de frente de onda, sensor de frente de onda piramidal, LGS.

ABSTRACT

In this work, the performance of a pyramid wavefront sensor for laser guide star (LGS) wavefront sensing is studied for telescopes with diameters between 8 and 40 m. Using an open source toolbox for Matlab called OOMAO, optical gains, linearity, dynamic range, sensitivity, and closed-loop operation of a PWFS were studied, and then compared the performance between a natural guide star (NGS) source and a LGS. The results indicate that for a LGS, it is possible to update the interaction matrix to optimize the reconstructor for the structure of the sodium layer, but the sensitivity drop in the LGS may generate the same effect in SNR than to lower the brightness of an NGS up to 5 magnitudes. Finally, it is shown that it is possible to close the loop on a LGS with a complete point source calibration for the telescope, but the drop in sensitivity would need a bright LGS, which might not be feasible in reality.

This suggests that the pyramid wavefront sensor would not be suitable for LGS wavefront sensing for the new extremely large telescopes.

Key words: AO, adaptive optics, wavefront sensor, pyramid wavefront sensor, LGS.

NOTATION AND SYMBOLOGY

	Definition
AO	Adaptive optics
WFS	Wavefront sensor
DM	Deformable mirror
SH	Shack-Harmann
PWFS	Pyramid wavefront sensor
RMS	Root mean square
NGS	Natural guide star
LGS	Laser guide star
PSC	Point source calibration
ESC	Elongated source calibration
λ	Observed wavelength
k	Wavenumber
$\delta\theta$	Amplitude of modulation
ϕ	phase of electromagnetic field
D	Diameter of telescope
Φ	Orthonormal basis matrix
A	Orthonormal basis mode amplitudes vector
$\mathbb{I}_p$	Pupil indicator function
$\langle x \rangle$	Expected value of random variable x
IMat	Interaction matrix
N	Size of matrix (N$\times$ N)
$\mathcal{R}$	Reconstruction matrix
ψ	Electromagnetic field function
ψ'	Electromagnetic field function propagated once
ψ''	Electromagnetic field function propagated twice
Δz	Distance of propagation
(x_p, y_p)	coordinates in the pupil plane
(x_i, y_i)	coordinates in the image plane
(x_d, y_d)	coordinates in the detector plane
$\mathcal{F}[(f_x, f_y), (x, y)]\{\}$	Fourier transform from (x,y) coordinates to (f_x, f_y)
r_0	Fried parameter
V	Signal of the PWFS
$\sigma()$	Standard deviation function
σ_ϕ	Standard deviation of ϕ

1. INTRODUCTION

1.1 Description of an adaptive optics system

Adative optics (AO) is a technique that allows the correction of phase aberrations of incoming wavefronts from astronomical objects, produced by turbulent layers in the atmosphere. Using one or more stars, the AO system is capable of measuring the phase distortions using a **wavefront sensor** and correct it using a **deformable mirror** (Babcock, 1953). Figure 1.1 shows a classical scheme of the application of an AO loop.

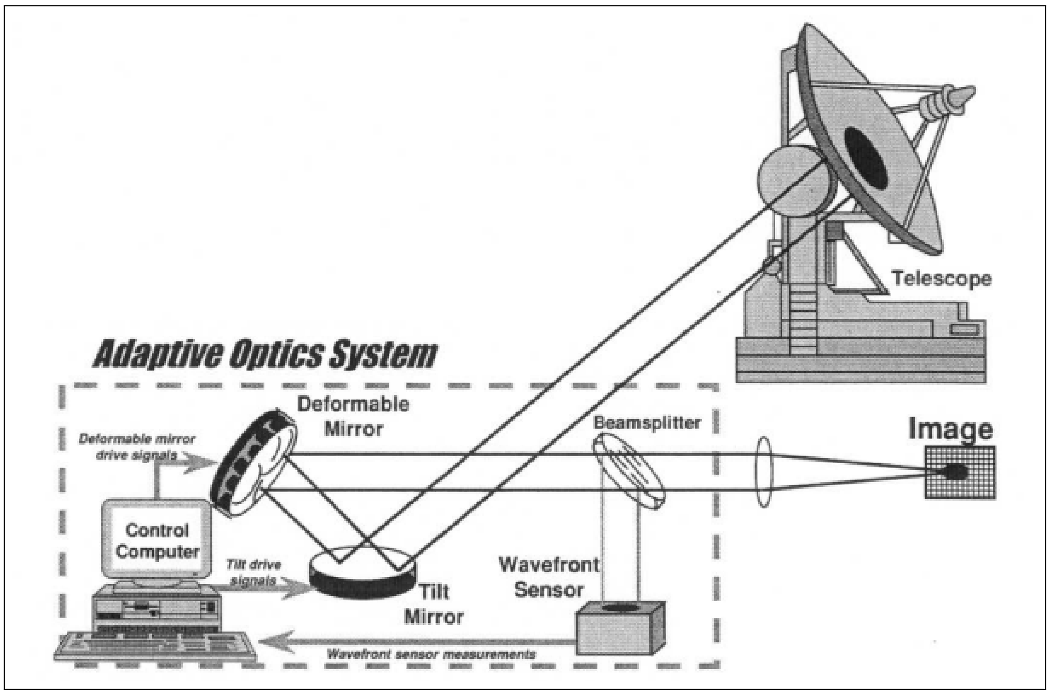

Figure 1.1: Classic scheme of AO system. (Credit Tyson (2000))

Figure 1.2: Example of an AO system in use. Left panel: image of Neptune with AO; right panel: no AO. (Credits: ESO)

A classic AO system is built using tree main components: a deformable mirror, a wavefront sensor and a control computer.

1.1.1 Deformable mirror

A deformable mirror (DM) is capable of modifying its reflective surface, which allows it to correct phase distortions of the incoming wavefront. This deformation is achieved through the use of actuators, which move a section of the mirror up or down. There are mainly two types of DMs: segmented surface and continuous surface (see figure 1.3). The former has advantages such as the independence of the segments and a precise control of the shape of the mirror. One of the disadvantages is that due to the segmentation there are sharp edges, which generates light losses due to diffraction effects. The latter has advantages such as a smooth surface that minimizes diffraction losses. A disadvantage is that there is coupling between the actuators. As an example, figure 1.4 shows a diagram of a DM correcting a distorted wavefront.

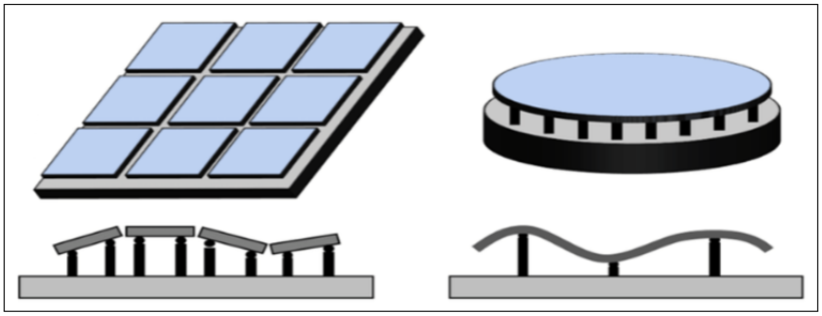

Figure 1.3: Types of deformable mirrors. Left panel: a deformable mirror with a segmented surface; right panel: a continuous mirror. (Credits Park (2018)).

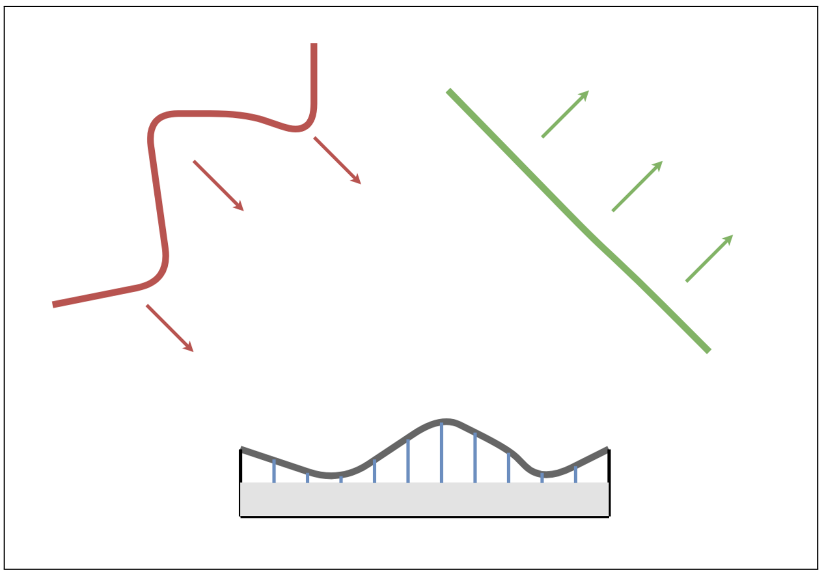

Figure 1.4: Working principle of a DM. The distorted incoming wavefront is corrected by the DM and the corrected wavefront follows its way to the rest of the AO system

Besides the type of surface, another important parameter for the deformable mirror is the number of actuators. A greater number of actuators means having a better spatial resolution to be able to correct phase errors, but it also means controlling a greater number of objects, which increases the computational demand and therefore the time necessary to process the information. For this work, a 21×21 Cartesian grid of actuators is used in a continuous surface DM.

1.1.2 Wavefront sensor

The wavefront sensor (WFS) is responsible for measuring the phase distortions of the wavefront. It consists of an optical element (a grid of lenses for a Shack-Hartmann type sensor, a glass pyramid for a pyramid type sensor) followed by a detector. Usually, the optical element allows transforming the phase distortions into an intensity signal that is then measured with the detector.

A wavefront sensor has the following fundamental characteristics:

- Amount of subapertures: Entrance pupil samples for wavefront measurement.
- Sensor type: The sensors can be subdivided into three categories depending on the relationship between the measurement and the phase of the wavefront: 1) direct, that is, it directly measures the phase, 2) gradient or slope, which measures the first spatial derivative of the phase and 3) curvature, which measures the second derivative of the phase of the wavefront.

1.1.2.1 Shack-Hartmann (SH) wavefront sensor

The SH sensor is currently the most widely used and works using an array of lenses, which produce images of the guide star. The difference in the position of neighbouring spots provides the local gradient of the wavefront, so the signal obtained is related to the derivative of the wavefront. For this reason the SH falls into the category of gradient sensors. Figure 1.5 shows a diagram of the SH wavefront sensor.

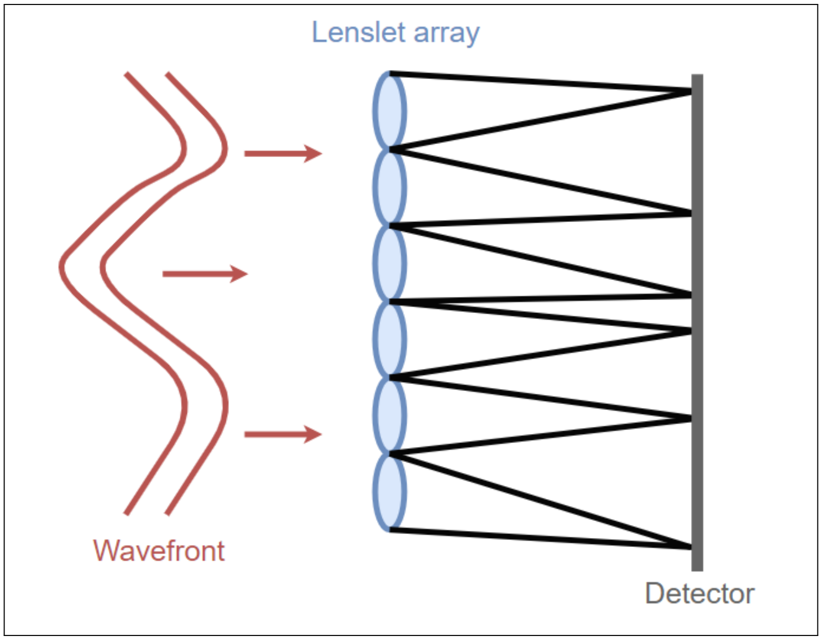

Figure 1.5: Working principle of the SH WFS. The distorted wavefront goes through the lenslet array and the local gradient of the wavefront is encoded in the position of each of the images of the guide star in the detector

To do a position measurement, the simplest way is to use a four pixel array. The signal level in each of them is compared to determine the centroid of the star. Let I_i be the intensity registered in the pixel S_i of size d_{pix}, represented in the figure 1.6. The center of the star (x_c, y_c) at each subaperture can be approximated by

$$
\begin{aligned}
x_c &= \frac{d_{pix}}{2} \frac{I_2 + I_4 - (I_1 + I_3)}{I_1 + I_2 + I_3 + I_4} \\
y_c &= \frac{d_{pix}}{2} \frac{I_1 + I_2 - (I_3 + I_4)}{I_1 + I_2 + I_3 + I_4}
\end{aligned} \tag{1.1}
$$

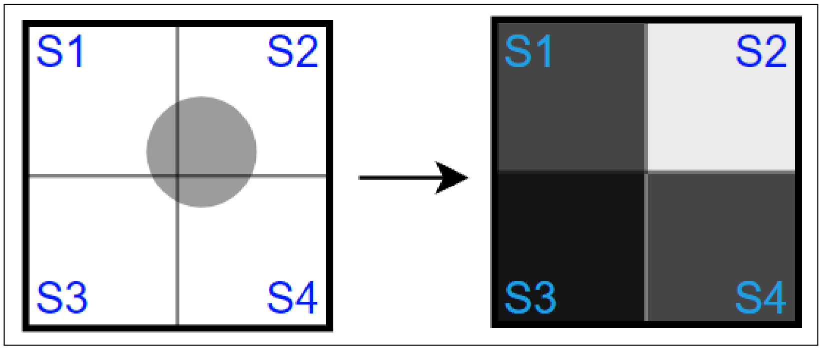

Figure 1.6: Left panel: the image of an off-center star (gray circle) in an array of four pixels. Each pixel is denoted as S_i. Right panel: the intensity recorded by each pixel on a gray scale

Then, the local gradient of the wavefront will be proportional to the position of the center of the star. The constant of proportionality will be a function of the size of the pixels and the optics used. This measurement is made in parallel for the entire wavefront. The portion of the entrance pupil that each lens measures is called the subaperture. Figure 1.7 shows what a wavefront measurement looks like using an SH sensor.

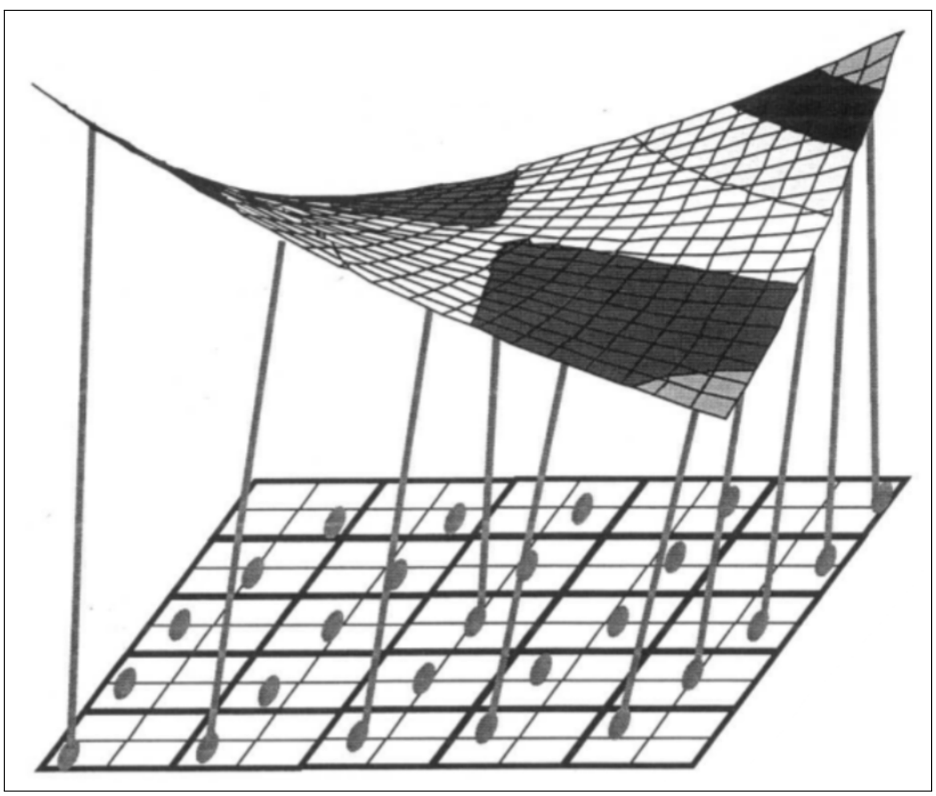

Figure 1.7: Measurement of a wavefront using an SH sensor (Credits Tyson (2000)).

As can be seen in figure 1.6, if the star falls on only one or two of the quadrants, then the sensor saturates (that is, there are no changes in intensity even when the star changes its position) and stops measuring. If the image of the star has a shape other than a circle (an ellipse for example) or is a resolved object (binary system, planet), the structure can interfere with the measurement, so in the case that you want to determine the center of the star more precisely or increase the dynamic range of the instrument, it is necessary to increase the number of pixels that are used to sample the image.

Once built, the SH sensor has fixed pupil sampling (subapertures), sensitivity, and dynamic range, as these depend on the physical parameters of the lens array and detector used.

1.1.2.2 Pyramid wavefront sensor (PWFS)

The pyramid wavefront sensor was proposed by Ragazzoni (1996). This sensor works on the same basic principle as the Foucault optical test (knife-edge test), where wavefront phase aberrations cause light rays to take different paths than the case without aberration. Then, by incorporating some kind of filter in the image plane, this path difference can be transformed into an intensity signal. An example of this optical test can be seen in the figure 1.8, where the phase aberration is transformed by a filter into an intensity signal in the image of the pupil.

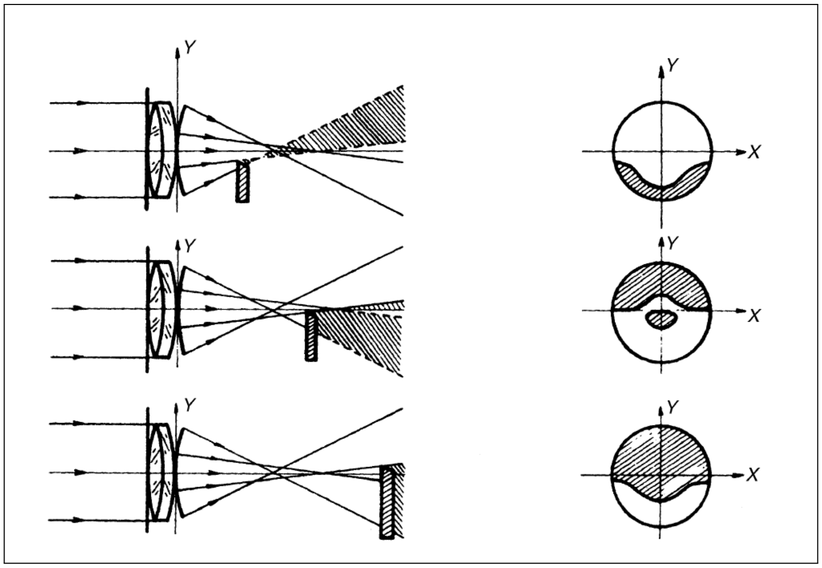

Figure 1.8: Foucault optical test example. In this case, the filter used is a knife blade that blocks light rays that take different paths due to aberrations. The figure shows three cases with knives in different positions on the left and on the right the image of the pupil obtained (Credits Malacara (2007)).

The pyramid sensor uses a glass pyramid with at least three faces to achieve a similar effect as the Foucault test. In the case of this investigation, a four-sided pyramid will be used, but it is possible to use other numbers, as shown in Fauvarque et al. (2017). Unlike the optical knife test, the pyramid does not block part of the light, but generates several images of the entrance pupil with different intensity patterns, thus reducing the loss of light. Figures 1.9 and 1.10 show the pyramidal sensor operation for some common types of aberrations.

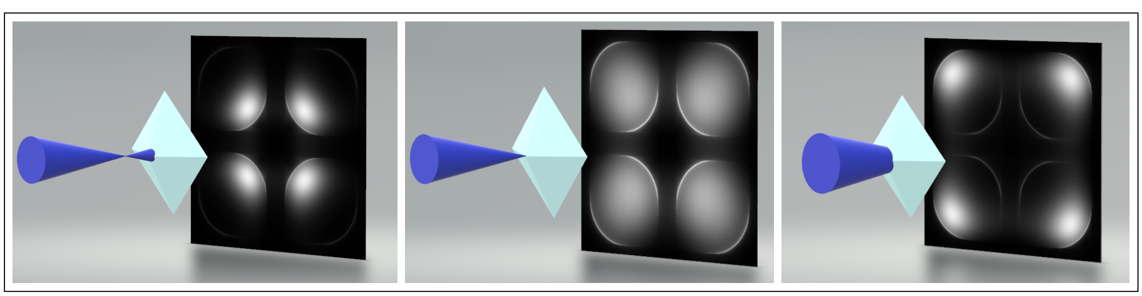

Figure 1.9: Pyramid type wavefront sensor operation. The beam of light hits the pyramid with varying degrees of focus aberration. Light is refracted in the pyramid and then continues its journey until it reaches the detector, which receives images of the entrance pupil with different illumination patterns. Left panel: Negative focus; middle panel: No distortion; right panel: Positive focus

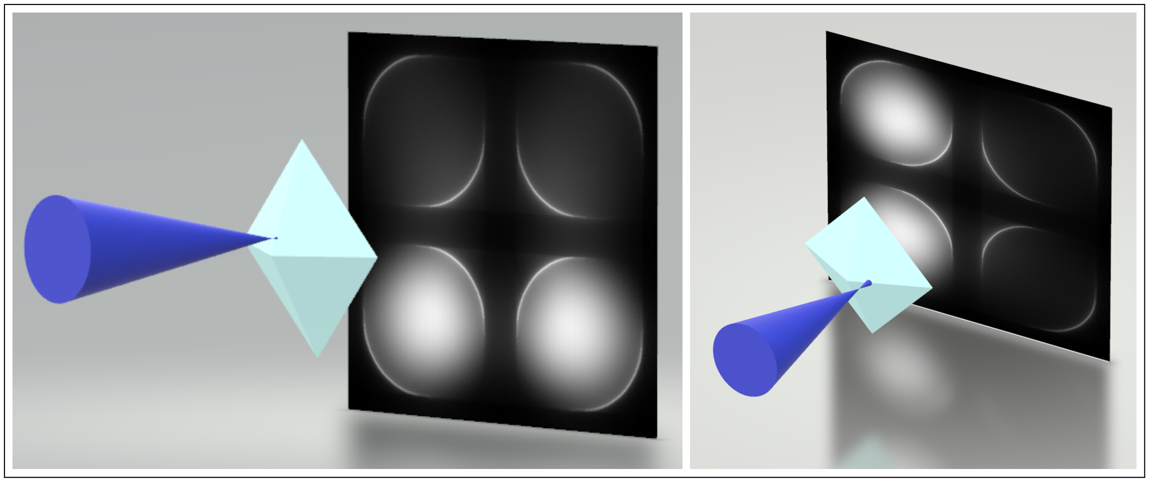

Figure 1.10: Pyramid type wavefront sensor operation. The beam of light hits the pyramid with different degrees of aberration of tip (left image) and tilt (right image) and the images of the entrance pupil show different illumination patterns.

As can be seen in the figure 1.10, when the image of the star is no longer centered, the light no longer interacts with two or even three of the four faces of the pyramid, so the sensor saturates. This is why a spatial modulation is introduced, which makes the image of the star travel through the pyramid, while the detector is integrating. This can be achieved, for example, with a tip & tilt mirror. Figure 1.11 shows what it looks like with and without modulation.

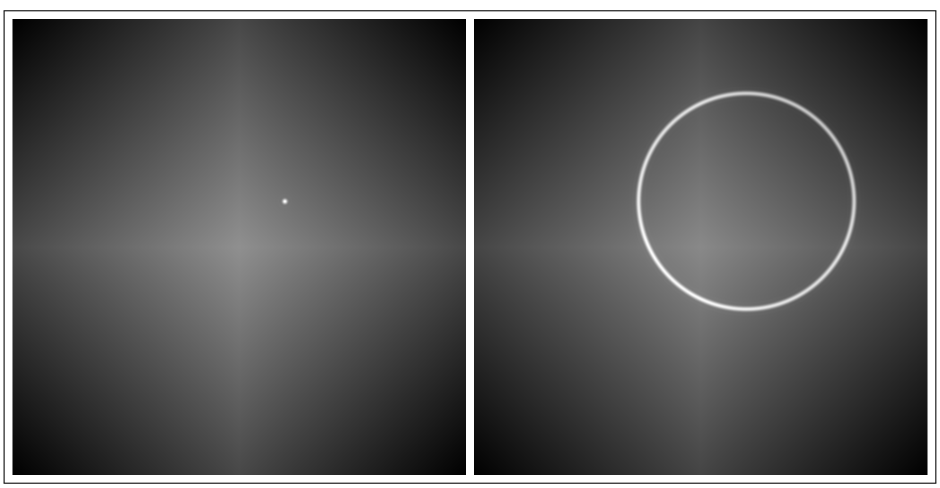

Figure 1.11: Images of the pyramid represented in grayscale, with an off-center star. Left panel: case without modulation, where the star (white point) falls on only one of the faces of the pyramid; right panel case with spatial modulation, where the white circle corresponds to the trajectory of the star above the pyramid.

As in the image on the right of the figure 1.11 the star passes through all the faces, then the sensor can continue to measure phase aberrations. This means that modulation increases the dynamic range of the instrument. Mathematically, this relationship can be understood as that the pyramid is able to measure phase distortions when the amplitude of the modulation angle, $\delta\theta$, is greater than the magnitude of the gradient of the wavefront at a given point (Riccardi et al., 1998), that is

$$\delta\theta > \left| \frac{\partial \phi}{\partial x}(P) \right| \tag{1.2}$$

By varying the modulation amplitude it is possible to adjust the sensitivity and dynamic range of the sensor. In addition, using a pair of lenses after the pyramid it is possible to change the sampling of the pupil by changing the size of its image in the detector. These features give the pyramid sensor flexibility; these parameters can be optimized for *seeing* conditions in real time.

The signal delivered by a PWFS can be obtained two ways: using slopes measurements or using the intensity maps.

Slopes measurements are obtained in a similar way to the SH sensor, but this time each of the four pixels is located in a different pupil, in the same relative position, as seen in figure 1.12. Each of these groups of four pixels corresponds to a subaperture. The total number of subapertures is given by the number of pixels in an image of the entrance pupil. Let I_i be the intensity of pixel S_i. The signal of each subaperture is obtained as

$$\begin{aligned} V_x &= \frac{1}{\delta\theta} \frac{I_2 + I_4 - (I_1 + I_3)}{I_1 + I_2 + I_3 + I_4} \\ V_y &= \frac{1}{\delta\theta} \frac{I_1 + I_2 - (I_3 + I_4)}{I_1 + I_2 + I_3 + I_4} \end{aligned} \tag{1.3}$$

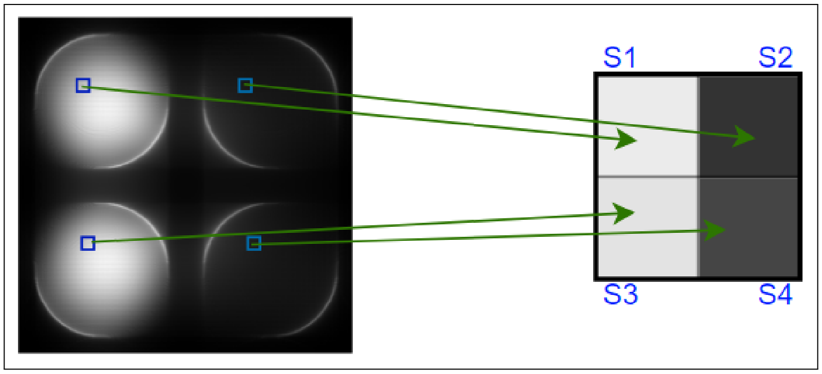

Figure 1.12: Left panel: the four images of the entrance pupil are observed with different intensities due to a tip aberration; right panel: the four pixels with the same relative position in each pupil, with the intensities recorded in gray scale.

Intesity maps are obtained using a **return to reference** operation (Fauvarque et al., 2017), represented in figure 1.13. Let I_0 be the normalized intensity detected in the detector when no aberration is present (Right image in figure 1.13), $I(\phi)$ the intensity detected when a phase ϕ is introduced and N_{ph} the number of photons in the image. The **meta intensity** is defined as

$$\Delta I(\phi) = I(\phi)/N_{ph} - I_0 \tag{1.4}$$

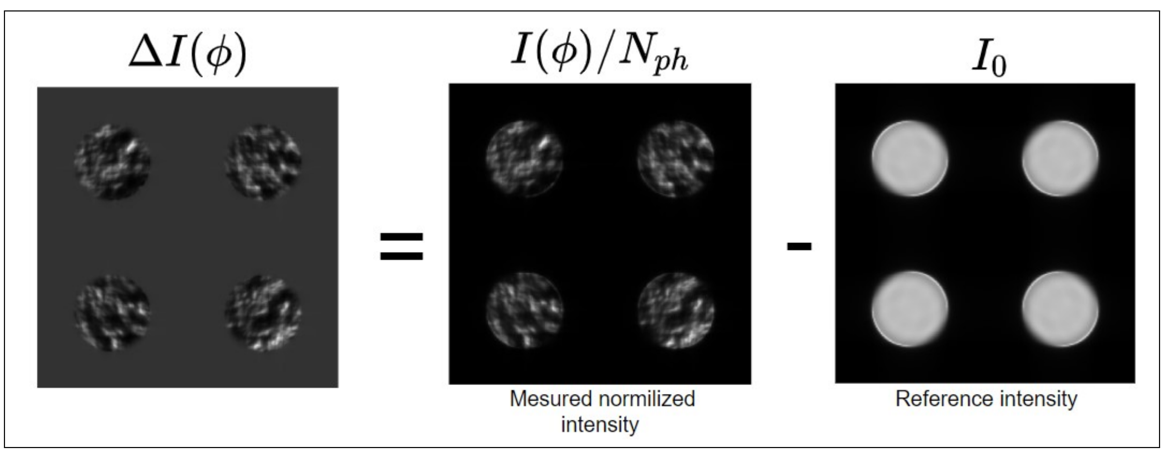

Figure 1.13: Diagram of the return to reference operation.

This meta intensity is vectorized using a mask with the shape four pupils (see figure 1.14) and recorded as the signal delivered by the sensor.

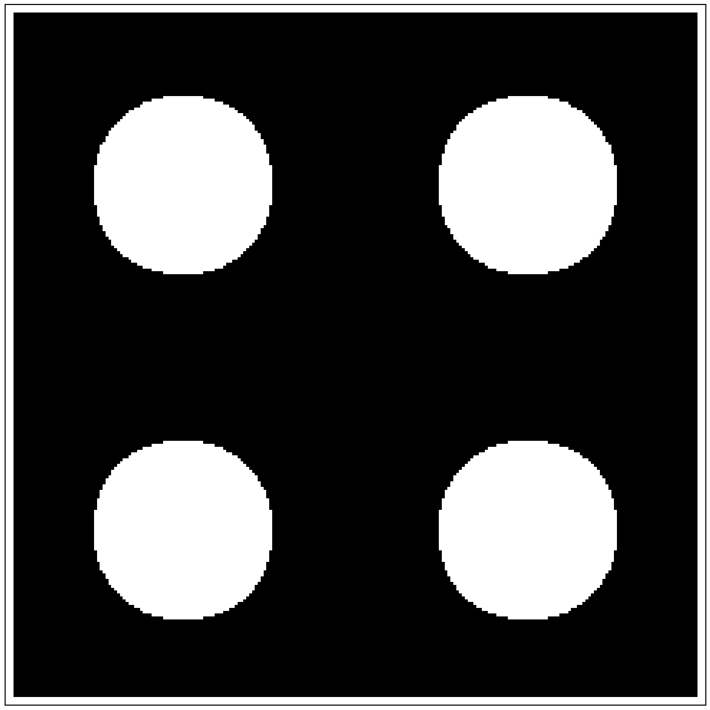

Figure 1.14: Mask used to extract the data from the meta intensity.

The intensity maps offer more flexibility when choosing the shape of the pyramid. As Fauvarque et al. (2017) showed, with this method it is possible to use different number of faces (3, 4, 6 or even ∞ as in a cone shape pyramid), pupils that overlap and interfere with each other, and use other kinds of Fourier filters, allowing room for optimization that was not possible with the slopes measurements. For this work, the intensity maps will be used as the signal produced by the PWFS.

Vérinaud (2004) demonstrated that the PWFS had a dual behavior. For low spatial frequencies ($f < \delta\theta/\lambda$, with λ the observed wavelength) it behaves like a gradient sensor, since its sensitivity increases proportionally with the spatial frequency. In this range, considering a telescope of diameter D and an angular amplitude modulation $\delta\theta$, the pyramidal sensor has a sensitivity gain of $\lambda/(2D\delta\theta)$ with respect to the SH sensor. For high spatial frequencies ($f > \delta\theta/\lambda$), its behavior is similar to that of a direct phase sensor, since its sensitivity remains constant, independently of the spatial frequency. As the sensitivity of the SH sensor continues to increase, the intersection point is at frequency $f = 1/(2D)$. For higher frequencies the SH sensor is more sensitive. Figure 1.15 shows a plot of this behaviour

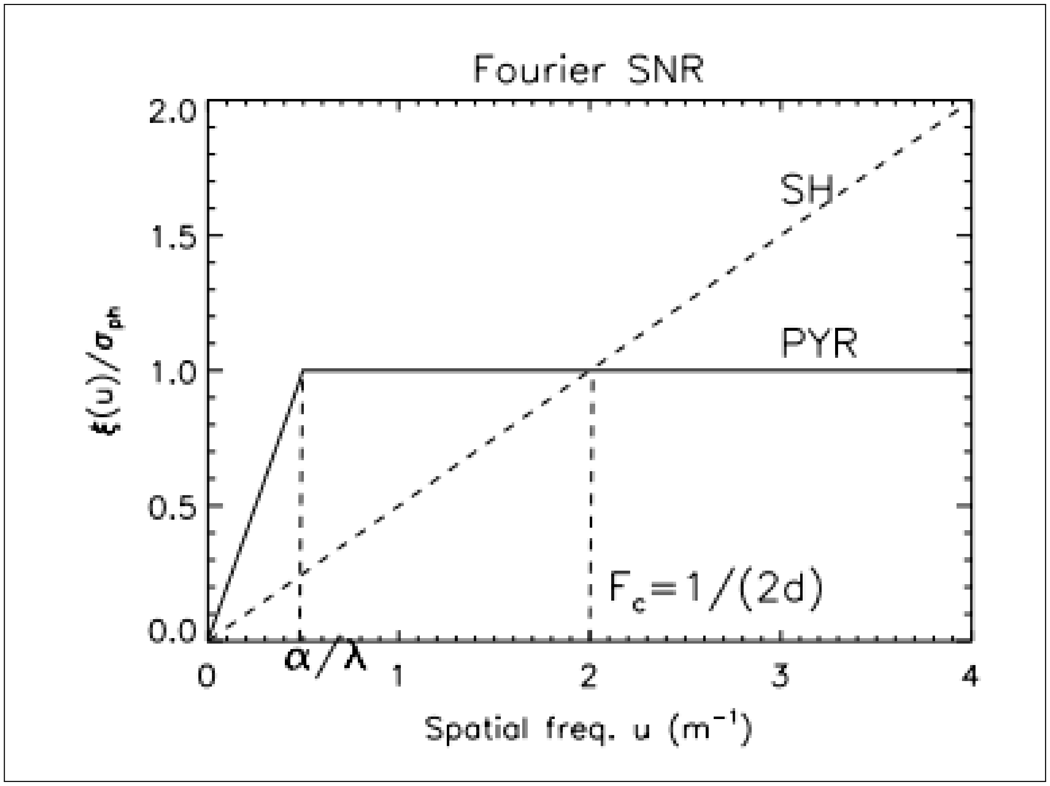

Figure 1.15: Sensitivity versus spatial frequency for PWFS and SH WFS. Here α is the modulation amplitude and d the telescope diameter (Credits Vérinaud (2004)).

1.1.3 Control computer

The control computer is in charge of recording the information delivered by the wavefront sensor, processing it, and sending the necessary commands to the deformable mirror in order to correct the wavefront. Due to discretization, this computer has to be able to evaluate matrix operations as quickly as possible, which is why the use of FPGAs and GPUs is common.

1.2 Atmospheric turbulence

The light from astronomical objects that reaches Earth travels practically unimpeded or distorted for up to millions of years and in the last fraction of millisecond, as it passes through Earth's atmosphere, the wavefront shape is distorted by the turbulent layers. This means that when taking an image, most of the high spatial frequencies get washed out. This impacts for example, the study of compact star clusters and exoplanet detection by direct imaging.

1.2.1 Physical and statistical description of turbulence

The physical description of the dynamics of the atmosphere was described by Kolmogorov (1941) and later improved by von Kármán (1948). The atmosphere is modeled as having air packages at different temperatures, which mix through convection processes, generating turbulence. The distortions start as large convective cells high up in the atmosphere with a size of the order of tens of meters, known as the outer scale (L_0). Because these cells are unstable, they decrease in size as they travel, until they reach a size of a few millimeters, known as the inner scale (l_0), and then dissipate due to viscosity effects. This process generates temperature gradients, which have effects on the refractive index of the air. These changes in the refractive index are what generate the phase distortions of the wavefront.

Due to the random nature of the process, it is helpful to use a statistical description of the process. A structure function is defined for each layer of the atmosphere as follows

$$D_n(\mathbf{r}, \mathbf{r'}) = \left\langle [n(\mathbf{r'}) - n(\mathbf{r'} + \mathbf{r})]^2 \right\rangle \tag{1.5}$$

with **r** y **r'** spatial coordinates in the plane at a given height and $\langle x \rangle$ the expected value of a random variable x. This function provides information about the spatial correlation that exists on the plane and therefore the level of distortion. If a stationary process is assumed, then it can be found that the correlation will only be a function of the distance and not of the direction ($|\mathbf{r}| \rightarrow r$) nor of the variable **r'** (Oboukhov, 1962). With this, a structure function is obtained as follows

$$D_n(r, h) = C_n^2(h) r^{5/3} \tag{1.6}$$

with C_n the structure constant of the refractive index, which characterizes the turbulence's force at each altitude.

1.2.2 Effect on the wavefront phase

As the wavefront passes through the atmosphere, different parts of it encounter different layers with varying index of refraction. The effect on the phase can be found using the following formula

$$\phi(r,\theta,h) = -\frac{2\pi}{\lambda}\int_{\infty}^{h}[n(r,\theta,h') - 1]\,dh' \tag{1.7}$$

Combining expression 1.7 with the statistical nature of the atmosphere, Tatarskii (1961) found that the structure function of the phase can be expressed as

$$D_{\phi}(r) = 6.88\left(\frac{r}{r_0}\right)^{5/3} \tag{1.8}$$

with r_0 Fried's parameter (Fried, 1966), which allows the estimation of the force of the turbulence along a column of air. It can be obtained as follows

$$r_0 = \left(0.423\,\frac{4\pi^2}{\lambda^2}\sec\gamma\int_{0}^{\infty} C_n^2(h)\,dh\right)^{-3/5} \tag{1.9}$$

with γ the zenith angle. This parameter is useful when describing the condition of the atmosphere, as it has the following interpretations:

- r_0 defines the diameter of the primary mirror of a telescope for which the modulation transfer functions of the telescope and the atmosphere are equal.
- r_0 is the distance on the primary mirror of a telescope for which the phase correlation has decreased by a factor 1/e.
- $(D/r_0)^2$ is approximately the number of degrees of freedom to be controlled / corrected by a AO system to recover the diffraction limit.

Using the Kolmogorov model it is possible to obtain a power spectral density (PSD) function for the phase introduced by the atmosphere

$$C_{\phi}(f) = 0.023\,r_0^{-5/3} f^{-11/3} \tag{1.10}$$

The problem with this PSD is that it diverges at spatial frequency $f \to 0$. This is why von Kármán (1948) introduced the outer and inner scales, arriving at

$$C_\phi(f) = 0.023\, r_0^{-5/3}\, \frac{e^{-(f/f_m)^2}}{(f^2 + f_0^2)^{11/6}} \tag{1.11}$$

with $f_m = 5.92/(2\pi l_0)$ the internal scale frequency and $f_0 = 1/L_0$ the external scale frequency.

1.2.3 Effect of the turbulence on image formation

Using diffraction theory, it is possible to obtain an expected shape for the point spread function (PSF) for a circular telescope of diameter D as

$$PSF(\theta) = I_0 \left(\frac{2J_1(x)}{x} \right)^2 \tag{1.12}$$

with $x = \frac{k\,D\theta}{2}$, θ being the angle of observation. Using expresion 1.12, it is possible to define Rayleigh's criterion for resolution, which implies that two point objects can be distinguished from one another if the peak of one object's PSF is at least further away than the first zero of the other object's PSF. Mathematically, the resolution can be found as

$$\Delta\theta = 1.22 \frac{\lambda}{D} \tag{1.13}$$

When the light passes through the atmosphere, the turbulence limits the optical transfer function so that the maximum equivalent diameter of a telescope is r_0, therefore the resolution is limited to

$$\Delta\theta_{atm} = 1.22 \frac{\lambda}{r_0} \tag{1.14}$$

As r_0 ranges from a few centimeters in poor sky condition to a few tens of centimeters at the best observatories (at 500 nm wavelength observations), a 40 m telescope has it's resolution worsen by a factor of at least 200. Figure 1.16 shows an example of the effect of the atmosphere in short and long exposures.

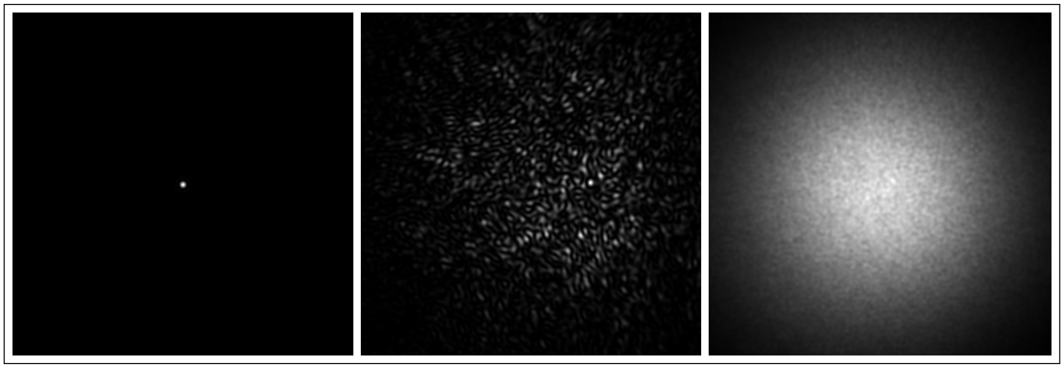

Figure 1.16: Left panel: image of a star without atmospheric turbulence with FWHM $= \frac{\lambda}{D}$; middle panel: a short exposure of a star with turbulence. The speckles in the image have a size comparable to that of the star; Right panel: a long exposure of a star with turbulence with FWHM $\approx \frac{\lambda}{r_0}$.

1.3 Modal representation of the wavefront

Due to the geometry of the optical elements, it is convenient to use an orthogonal base that allows us to represent a circular surface with only the associated modal coefficients. In a similar way to the Fourier base in rectangular space, Zernike (Zernike, 1934) or Karhunen-Loeve (Dai, 1995) basis allows any circular surface to be decomposed as an infinite sum of orthogonal basis.

Let $\phi(r, \theta)$ be any surface in polar coordinates and ϕ_j an orthogonal basis over the unit circle. Its modal expansion over a circle of radius R is

$$\phi(r, \theta) = \sum_j a_j \phi_j(r/R, \theta) \tag{1.15}$$

The coefficients a_j can be obtained using the orthogonality relation as

$$a_j = \int_{\mathbb{R}^2} dr^2\, w(r/R)\, \phi_j(r/R, \theta)\, \phi(r, \theta) \tag{1.16}$$

with $w(r)$ a weighing function defined in the unit circle.

When working with a finite number of samples discretizing the entrance pupil, this expression can be denoted in a matrix way as

$$\phi = \Phi \mathbf{A} \tag{1.17}$$

where ϕ is the vector corresponding to the surface values, Φ is a matrix where each column corresponds to a discretized orthogonal mode and $\mathbf{A}$ is the vector of coefficients of the decomposition. The maximum number of columns that the Φ matrix has is limited by the number of samples of the entrance pupil. This means that when discretizing, the modal representation corresponds only to an approximation of the original surface. This approximation tends to the original when the number of modes tends to infinity, but this means that the number of samples tends to infinity, so we are again in the continuous case. Figure 1.17 shows an example of the use of Zernike modes. In this case, an attempt is made to approximate the original image denoted by a letter "F" using different amounts of modes.

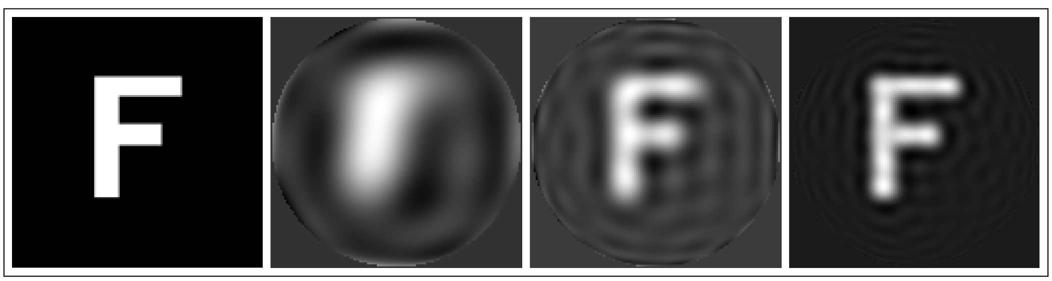

Figure 1.17: The original figure is on the left and shows a letter " F ". Then from left to right are images of the approximation using 50, 200 and 500 Zernike modes respectively.

Using only a few modes to approximate the original image loses most of the information. Then, if you increase the number of modes used, you begin to have a general idea of what was originally. Finally, when you use even more modes you can notice a better approximation to the original. The high-frequency components of the original image, such as corners or edges, are not well represented, which can be explained by the Nyquist sampling theorem (Nyquist, 1928).

1.3.1 Zernike basis

Zernike bases or polynomials (Zernike, 1934), usually denoted as $Z_j(r, \theta)$ with r and θ the polar coordinates, comply with the following orthogonality relation

$$\int_{\mathbb{R}^2} dr^2\, w(r)\, Z_j(\mathbf{r})\, Z_k(\mathbf{r}) = \delta_{jk} \tag{1.18}$$

with δ_{jk} Kronecker's delta and

$$w(r) = \begin{cases} 1/\pi & r \leq 1 \\ 0 & r > 1 \end{cases}$$

where the index j of the polynomials is indicates an arbitrary ordering of the polynomials, so different works may have different conventions. Noll (1976) arranged them so that the even j 's correspond to symmetric modes, defined by $\cos m\theta$ and the odd ones to anti-symmetric modes, defined by $\sin m\theta$. The ordering is done in such a way that, in general, increasing j increases the radial order and the azimuth frequency. This will be the ordering used in this work.

Following Noll (1976), Zernike bases or polynomials are generally expressed in their polar form and have the following expressions

$$\begin{aligned} Z_{j\,even,\,m\neq 0} &= \sqrt{n+1} R_n^m(r) \sqrt{2} \cos\, m\theta \\ Z_{j\,odd,\,m\neq 0} &= \sqrt{n+1} R_n^m(r) \sqrt{2} \sin\, m\theta \\ Z_{j,m=0} &= \sqrt{n+1} R_n^0(r), \end{aligned} \tag{1.19}$$

with

$$R_r^m(r) = \sum_{s=0}^{(n-m)/2} \frac{(-1)^s (n-s)!}{s![(n+m)/2-s]![(n-m)/2-s]!}\, r^{n-2s} \tag{1.20}$$

The values of n and m are always integers and comply with $|m| \leq n$ & $n - |m|$ even. Figure 1.18 shows the first ten Zernike polynomials.

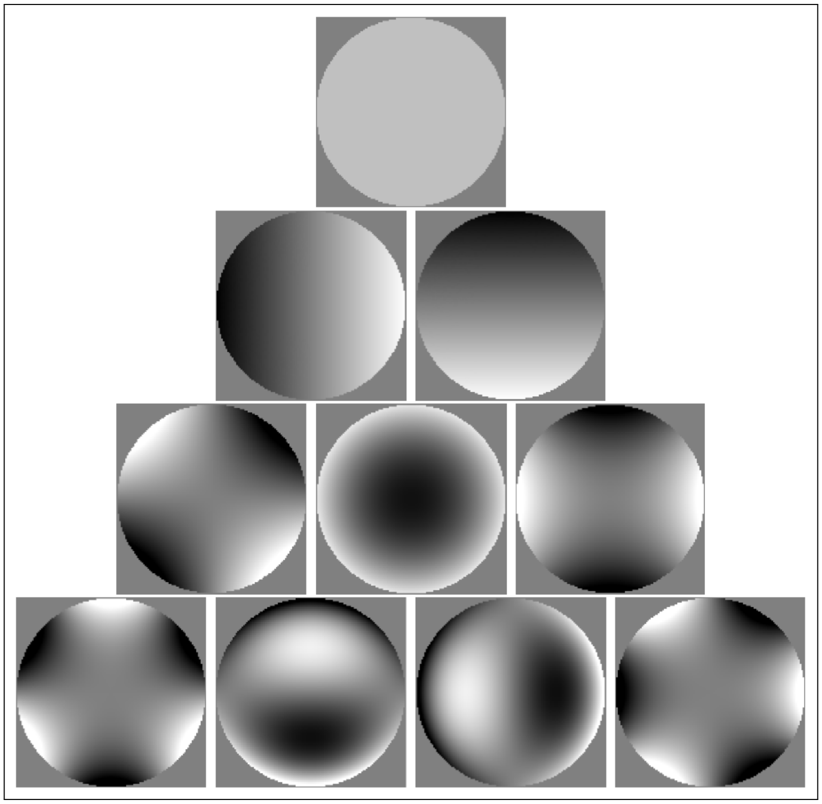

Figure 1.18: First ten Zernike polynomials arranged vertically by radial order and horizontally by azimuthal order

Zernike polynomials are sometimes not the best basis to be used due to the following inconveniences:

- Orthogonality is lost with central obstructions or *spiders* used to hold the secondary mirror.
- As the order increases, the energy of each mode tends to concentrate only in the edges.
- The order of the basis is arbitrary and does not correlate perfectly with an increase in spatial frequency.
- The covariance matrix of the Zernike polynomials is not diagonal, which means that the modes are not statistically independent (Dai, 1995). Statistical independence is a requirement due to the random nature of atmospheric distortions.

1.3.2 Karhunen-Loeve (KL) basis

Any orthogonal basis in which the modes are statistically independent is called a KL basis (Dai, 1995).

This basis is constructed using the spatial covariance matrix of the phase in the pupil. Let **r** and **r'** be points in the aperture, and ϕ the phase in the pupil which follow Kolmogorov statistics. The covariance matrix is obtained as

$$Cov_{\phi}(\mathbf{r},\mathbf{r'}) = \langle \mathbb{I}_p(\mathbf{r})\phi(\mathbf{r})\mathbb{I}_p(\mathbf{r'})\phi(\mathbf{r'})\rangle \tag{1.21}$$

where $\mathbb{I}_p$ is an aperture function and $\langle x\rangle$ the expected value of a random variable x. The KL modes are obtained by first computing a Zernike covariance matrix over the atmospheric turbulence (refer to equations 3.13 and 3.14 in Roddier (1999)). Then this matrix can be diagonalized, and its eigen-vectors are the KL modes (Roddier, 1999).

Using this, it is possible to mitigate most of the inconveniences of the Zernike basis. Due to it's construction, it takes into account the shape of the entrance pupil, therefore it is possible to work with obstructions. As the number of the mode increases, the spatial frequencies also increases. For all the modes, energy is roughly spread through out the whole area of the pupil. Figure 1.19 shows examples for some of the KL modes for a circular pupil.

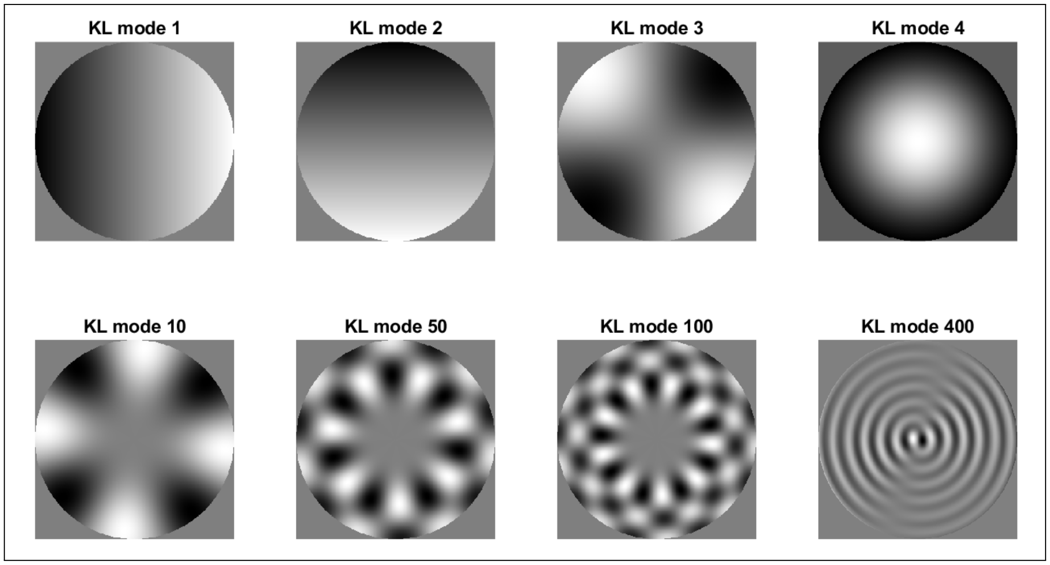

Figure 1.19: Examples of KL modes for a circular pupil

As it can be seen in figure 1.19, the first modes for the KL basis are similar to those of the Zernike basis (figure 1.18), but as the order increases they differ in energy distribution, making it better distributed through the pupil area. This effect, together with statistical independence, allows for better levels of approximation (and AO correction) than the Zernike basis for the same number of modes used.

1.4 Wavefront Reconstruction and Interaction Matrix

When you have the wavefront sensor measurements, it is necessary to process the information to be able to recreate the wavefront, and in this way to be able to send the relevant commands to the deformable mirror. Two ways used for this reconstruction are model based or by means of an interaction matrix.

The model is a theoretical approach to wavefront reconstruction. In this method some analytical expression relates the wavefront measurements to the original phase. The problem with this method is that it does not take into account aspects such as misalignments or other effects that can interfere with the signal.

1.4.1 Interaction Matrix

The interaction matrix (IMat) corresponds to an experimental method to calibrate the wavefront reconstruction. The method consists of "showing" certain known aberrations to the wavefront sensor using the DM and recording their measurements in the columns of a matrix called the **interaction matrix**. In the case of this work, the *push-pull* technique is used, which consists of showing the sensor each KL mode twice, the first with a positive amplitude and the second with a negative amplitude (hence the name). The vector obtained by subtracting the signal from both cases is recorded in each column of the interaction matrix. The amplitude of the input mode should be as small as possible, to ensure that the system is working in the linear regime. Figure 1.20 shows a diagram of the push pull method for a single mode.

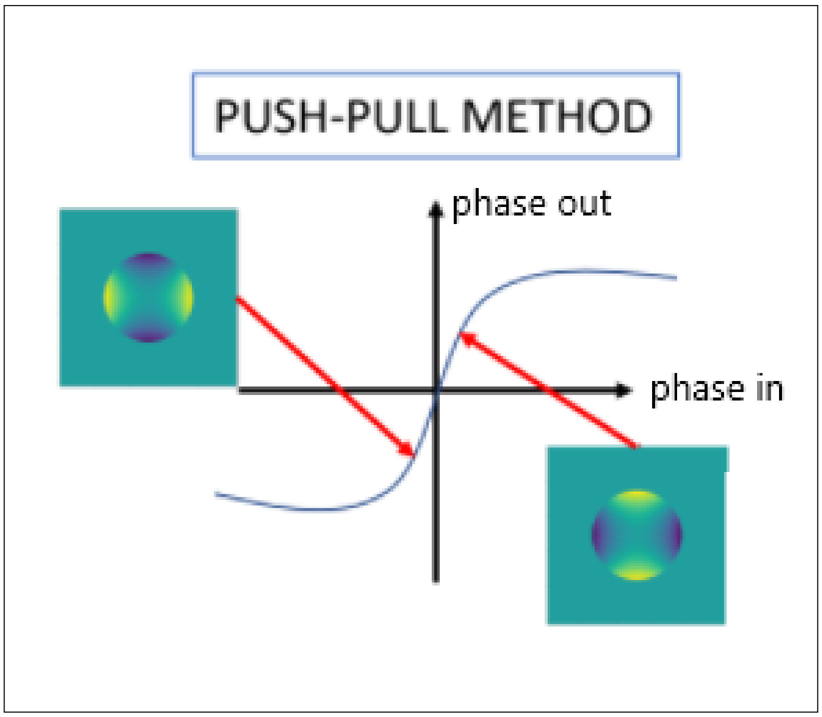

Figure 1.20: Graphical representation of the push pull method. The light blue curve corresponds to the response of the wavefront sensor (*phase out*) given an input aberration (*phase in*)

Mathematically, the push-pull method for each column of the interaction matrix is obtained as

$$\delta I(\phi_i) = \frac{I(\epsilon\phi_i) - I(-\epsilon\phi_i)}{2\epsilon N_{ph}} \tag{1.22}$$

with N_{ph} the number of photons arriving to the detector and $\epsilon \ll 1$.

The advantage of this method is that it takes into account most of the non-idealities of the system, which would be complex to include in a model based reconstruction. One downside is that it takes time to calibrate, which otherwise could be used for science observations, and can also introduce noise to the reconstruction.

1.4.2 Wavefront reconstruction

Let ϕ_c be the vector that represents the reconstructed wavefront, **IMat** the interaction matrix, V the vector that contains all the signal delivered by the sensor and A_c the vector of amplitudes of the KL modes of the reconstructed wavefront. Considering the inverse process of the interaction matrix, it is possible to obtain the vector of amplitudes of the modal decomposition of the reconstructed wavefront as

$$A_c = \mathbf{IMat}^{\dagger}\, V \tag{1.23}$$

Since the interaction matrix is not necessarily a square matrix, a pseudo inverse based on singular value decomposition is used, denoted with the superscript †. A_c corresponds to the vector of commands sent to DM. Mathematically, to reconstruct the wavefront, equation 1.17 must be used

$$\phi_c = \Phi\, A_c \tag{1.24}$$

Since we are using the KL basis, Φ's columns are it's modes. Combining equations 1.23 and 1.24 we get

$$\phi_c = \Phi\, \mathbf{IMat}^{\dagger}\, V \tag{1.25}$$

The two matrices of the equation 1.25 can be processed before the closed-loop operation, which returns the reconstruction matrix $\mathcal{R}$

$$\mathcal{R} = \Phi\, \mathbf{IMat}^{\dagger} \tag{1.26}$$

So the reconstructed wavefront can be obtained by transforming the sensor signal using the reconstruction matrix

$$\phi_c = \mathcal{R}\, V \tag{1.27}$$

equation 1.27 means that the reconstruction of the wavefront can be carried out by doing a single matrix multiplication.

The residual phase ϕ_{res} is obtained subtracting the reconstructed to the turbulent input

$$\phi_{res} = \phi - \phi_c \tag{1.28}$$

1.5 Closed loop operation

The adaptive optics system is a MIMO control loop, that is, it has multiple inputs (the measurement of each subaperture of the wavefront sensor) and multiple outputs (the position of each actuator on the deformable mirror). If the wavefront sensor is located before the deformable mirror, then it is an open control loop, since there is no record of the corrections made. If the wavefront sensor goes after the deformable mirror, then we have a closed loop (figure 1.1).

Using a modal approach, it is possible to decouple each mode and control them independently. This has the benefit of instead of having a MIMO system, having m parallel single input single output (SISO) subsystems, with m the number of orthogonal modes of the system to correct.

The simplest way of controlling an AO system is with an integrator. As the control is done by a computer and the wavefront sensor has to take an image of a certain exposure time, a discrete approach has to be made to understand the dynamics of the system. Let $a(nT)$ be the modal command sent to the DM, with n the discrete time variable and T the period, and $d(nT)$ the vector of modal measurements given by the WFS (residuals). For each mode, the command sent to the DM can be a function of the commands sent in a previous cycle and the measurements done so far

$$a(nT) = \sum_{j=0}^{p} \beta_j d((n-j)T) + \sum_{i=1}^{l} \alpha_i a((n-i)T) \tag{1.29}$$

Using the z-transform, it is possible to get the discrete transfer function

$$\mathcal{C}(z) = \frac{\sum_{j=0}^{p} \beta_j \, z^{-1}}{1 - \sum_{i=1}^{l} \alpha_i \, z^{-1}} \tag{1.30}$$

Taking into account the dynamics of the DM and WFS, we have that the DM holds its shape for the duration of the integration time T, therefore, its zero order hold transfer function is (Roddier, 1999)

$$M(s) = \frac{1 - e^{-sT}}{sT} \tag{1.31}$$

The WFS integrates a continuous signal during the exposure time of the detector, and the readout and computation times generate a delay of $\tau \rightarrow e^{-s\tau}$. Therefore, the WFS transfer function is (Roddier, 1999)

$$S(s) = \frac{1 - e^{-sT}}{sT} e^{-s\tau} \tag{1.32}$$

The closed loop transfer function assuming that the frequency is smaller than $1/4$ of the sampling rate, is

$$G(s) = \left(\frac{1 - e^{-sT}}{sT} \right)^2 e^{-s\tau} \mathcal{C}(z = e^{sT}) \approx e^{-s(T+\tau)} \frac{\sum_{j=0}^{p} \beta_j \, e^{-jsT}}{1 - \sum_{i=1}^{l} \alpha_i \, e^{-isT}} \tag{1.33}$$

In a simple case, where we only take into account the previous command to the DM and the new measurement, the transfer function is

$$G(s) = e^{-s(T+\tau)} \frac{\beta_0}{1 - \alpha_1 e^{-sT}} \tag{1.34}$$

if $\tau \approx T$, meaning that the processing time takes approximately one frame to compute, and $sT \ll 1$, the transfer function can be approximated as

$$G(s) \approx e^{-sT} \frac{\beta_0}{(1 - \alpha_1) + s} \tag{1.35}$$

This expression corresponds to a one cycle delayed leaky integrator. A leaky integrator is useful because it behaves similar to an integrator, but leaks over time, preventing wind ups. The closed loop operation box diagram can be seen in figure 1.21, where g corresponds to a gain and $e(s)$ to any source of error in the measurement.

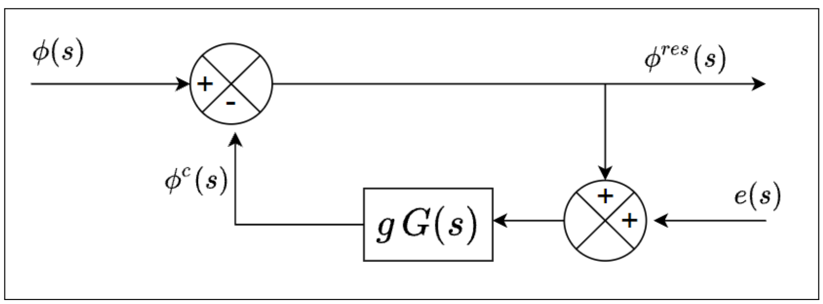

Figure 1.21: Closed loop operation diagram

Using the box diagram in figure 1.21 it is possible to obtain an expression for the residual phase

$$\phi^{res}(s) = \frac{1}{1 + g\,G(S)}\phi(s) - \frac{g\,G(s)}{1 + g\,G(S)}e(s) \tag{1.36}$$

This expression will allow us to optimize the parameters of the controller, in order to minimize the residual phase in closed loop operation.

1.6 Error budget and Strehl ratio

The Strehl ratio (SR) is defined as the ratio between the maximum amplitude of the observed star over the maximum amplitude of a diffraction limited star (Strehl, 1895). It gives a measure of the quality of the correction. It goes from zero to one, being one a practically perfect correction. Figure 1.22 shows a diagram of a cross-section of a PSF with and without atmospheric distortions.

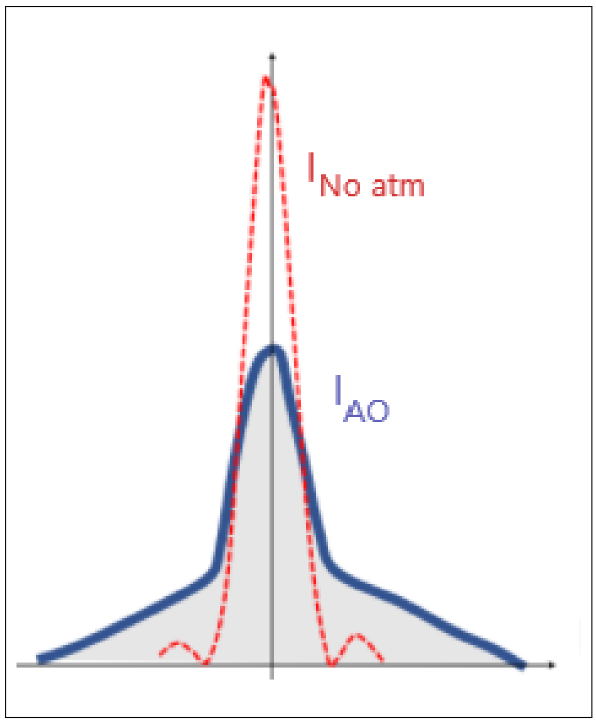

Figure 1.22: Cross sections of the PSF for a diffraction limited telescope ($I_{No\ atm}$) and the PSF when using AO to correct for the atmosphere (I_{AO}).

Mathematically, the SR is computed as

$$SR = \frac{I_{AO}(0)}{I_{No\ atm}(0)} \tag{1.37}$$

Due to the difficulty of knowing the intensity with no atmosphere, an approximation is used (Mahajan, 1983).

$$SR \approx e^{-\sigma_\phi^2} \tag{1.38}$$

with σ_ϕ^2 the variance of the residual phase. The approximation improves as σ_ϕ goes to zero and underestimates the ratio for higher values of the residual.

When the AO system is in action, the variance of the residual phase can be estimated as a sum of different sources of error (Veran et al., 1997).

$$\sigma_\phi^2 = \sigma_{fitting}^2 + \sigma_\tau^2 + \sigma_{nl}^2 + \sigma_\theta^2 + \sigma_{noise}^2 \tag{1.39}$$

1.6.1 Fitting error

Fitting error comes because of the limited number of actuators used to correct the wavefront, therefore the DM acts as a high pass filter.

$$\sigma_{fitting}^2 = \alpha_F \left(\frac{D}{r_0}\right)^{5/3} n_{act}^{-5/6} \tag{1.40}$$

with $\alpha_F \sim 0.3$ a DM technology dependant coefficient and n_{act} the number of actuators in the DM (Hardy, 1998).

1.6.2 Temporal error

Phase variance can be introduced by the delay of the corrections of the system. A coherence timescale, which encodes the time for when the turbulence changes by 1 rad, can be computed as (Hardy, 1998)

$$\tau_0 = 0.314 \cos\gamma \frac{r_0}{V} \tag{1.41}$$

with γ the zenith angle and V the weighted wind speed over the present layers in the atmosphere. If the system has a delay of $\tau_{delay} = T + \tau$, due to exposure time T and computing time τ, a temporal error can be obtained with expression 1.42 (Hardy, 1998).

$$\sigma_\tau^2 = 28.4 \left(\frac{\tau_{delay}}{\tau_0}\right)^{5/3} \tag{1.42}$$

For an effective AO system, τ_{delay} should be at least 5 times smaller than τ_0.

1.6.3 Non linearities

Non linearities can come from different sources, like the DM or the WFS. For example, the membrane of a continuous type DM may not act in a linear manner when two actuators are activated. WFS can introduce measurement errors that can also contribute to the non linearities.

1.6.4 Anisoplanatism error

Anisoplanatism error comes from the fact that the column of air that is between the telescope and the guide star is not the same as the column between the telescope and the science object. An isoplanatism angle can be defined as the angle distance where there is a 1 rad difference in the phase, and can be computed as (Hardy, 1998)

$$\theta_0 = 0.314 \cos\gamma \frac{r_0}{\overline{h}} \tag{1.43}$$

with $\overline{h}$ the height of the turbulent layer. If the guide star is at an angle θ_{obs} of the science target, then the anisoplanatism error introduced is given by expression 1.44 (Fried, 1982; Hardy, 1998)

$$\sigma_\theta^2 = \left(\frac{\theta_{obs}}{\theta_0}\right)^{5/3} \tag{1.44}$$

1.6.5 Noise

When using a detector there are two main sources of noise: photon noise and read out noise (RON).

Photon noise comes from the discrete nature of photons, making them arrive at the detector following a Poisson distribution, where noise is equal to the square root of the mean flux.

RON is noise that comes from the electronics of the detector. In general, it is not dependant on the flux, but increases with temperature, therefore it is necessary to cool down the detector.

These sources of noise can introduce random variations in the measurement of the wavefront sensor, therefore they have an impact on the residual phase. The formula for the noise, given an input modal phase is (Correia et al., 2020)

$$\sigma^2_{\phi_i} = \frac{4\sigma^2_{RON}}{s^2(\phi_i)\, N^2_{ph}} + \frac{1}{s^2_{\gamma}(\phi_i)\, N_{ph}} \tag{1.45}$$

with σ_{RON} the the average read-out-noise in photo-electrons per pixel, N_{ph} the amount of photons, $s(\phi_i)$ the modal phase sensitivity to RON, and $s_{\gamma}(\phi_i)$ the modal sensitivity to photon noise (Correia et al., 2020). Sensitivities will be defined in section 1.8. If N modes are corrected with the DM, the total error introduced by noise can be obtained as the sum of the variances.

$$\sigma^2_{noise} = \sum_{N} \sigma^2_{\phi_i} \tag{1.46}$$

1.7 Laser guide star (LGS)

The use of laser guide stars makes it possible to increase the coverage of AO systems, due to the lack of natural guide stars (NGS) bright enough to be able to correct atmospheric aberrations (Tyson, 2000). These laser stars are generated by exciting sodium atoms present in a layer of the atmosphere located approximately 90 km above sea level. Due to the width of the laser beam, the spot has a radial extension. Typical LGS' have a diameter from 30 to 50 cm. Also, the sodium layer has a thickness of between 10 to 20 km (see figure 1.23), which makes the artificial star a 3D extended object (Olivier and Max, 1994) (See figure 1.24). Figure 1.25 shows two examples of LGS. In the left image it is seen how the lasers are fired from the telescope and the right shows the generation of the artificial star.

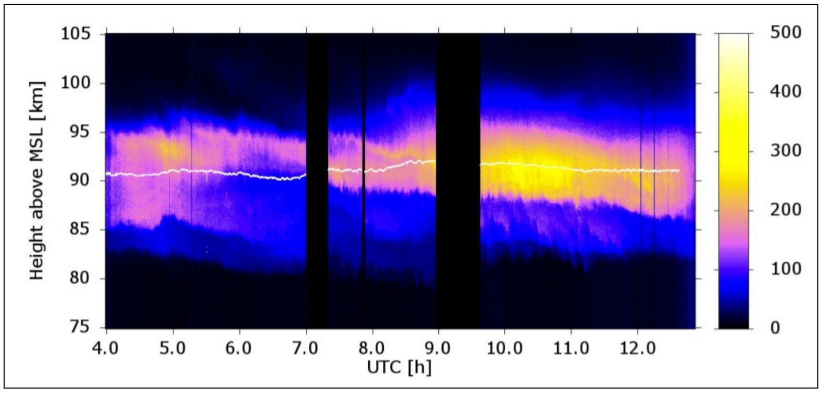

Figure 1.23: Measured sodium density for an arbitrary night. The color bar indicates the relative photon emissions received and the while line the mean altitude (Credits Pfrommer and Hickson (2014)).

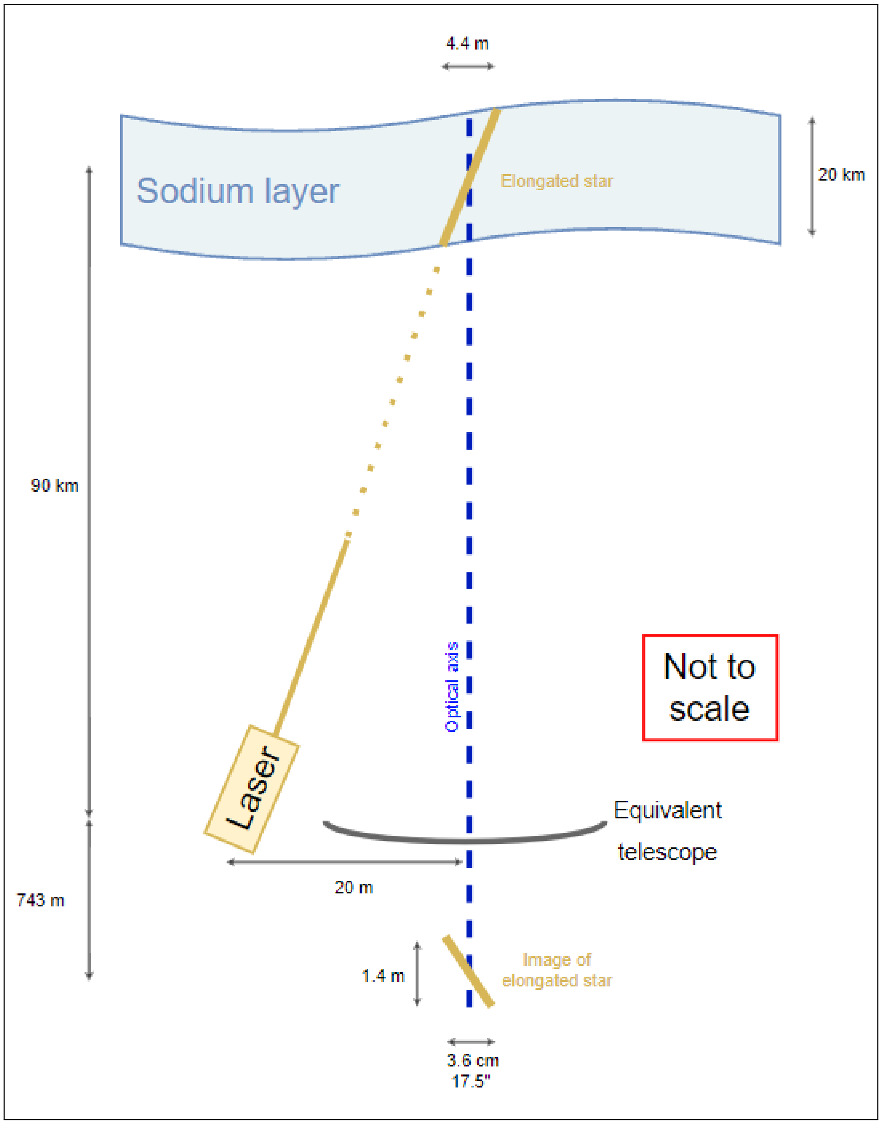

Figure 1.24: Diagram to illustrate the source of the 3D spot elongation of the LGS in the image plane of the telescope.

Figure 1.25: LGS in action. Left panle: image of multiple lasers being fired from one of the VLTs to produce LGSs (Credits ESO (2017)); Right panel: image showing part of the laser path and the artificial guide star (Credits NOIRLab (2017))

The distribution of sodium atoms can affect the shape and size of the LGS. As seen in figure 1.23, it can vary substantially in a single night, therefore it is necessary to test the system for different sodium profiles.

Taking cross sections of the sodium profile, it is possible to observe some of the distribution of sodium atoms at different observation times, as seen in figure 1.26

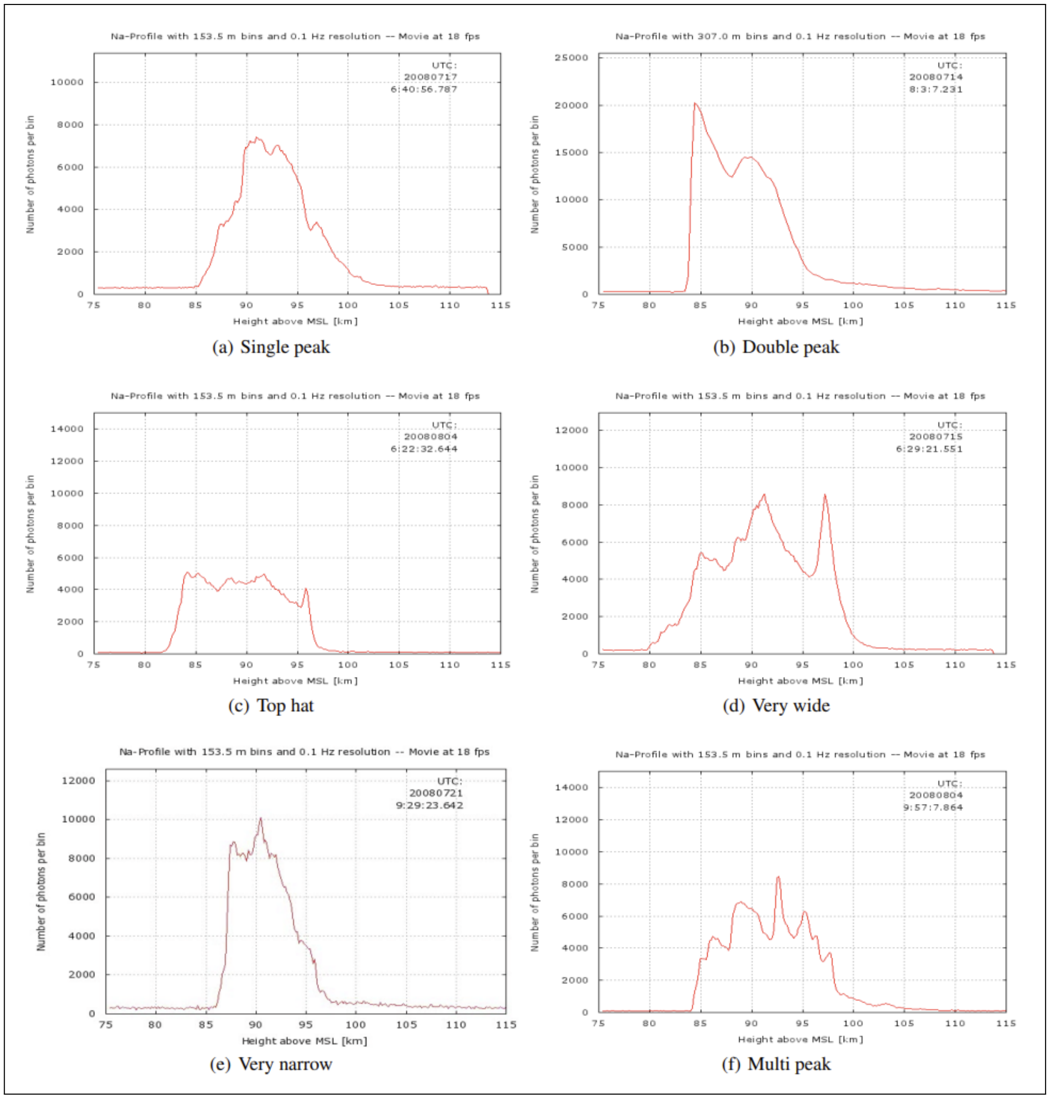

(a) Single peak (b) Double peak (c) Top hat (d) Very wide (e) Very narrow (f) Multi peak

Figure 1.26: Multiple sodium profiles with classification (Credits Pfrommer and Hickson (2014)).

An average shape of the sodium density profile can be approximated as a Gaussian with FWHM = 7 km centered at 90 km (Esposito et al., 2016) (similar to plots 1.26.a and 1.26.e). For this work, two sodium profiles will be used, a simple **Gaussian profile** as described before for most of the tests, and a more complicated case such as a **Double peak profile** similar to 1.26.b for some specific examples.

On a large pupil, like the ELTs, the sub-apertures of a Shack-Hartmann wavefront sensor see the LGS as an elongated object depending on their position with respect to the laser launch telescope. As a result, a detector with a large number of pixels per sub-aperture is required to fully sample the elongated spots and minimize centroiding errors. At the scale of the ELTs such a detector is difficult to realize(Fusco et al., 2019). Figure 1.27 shows a diagram with an example of the elongated spots obtained with the SH sensor.

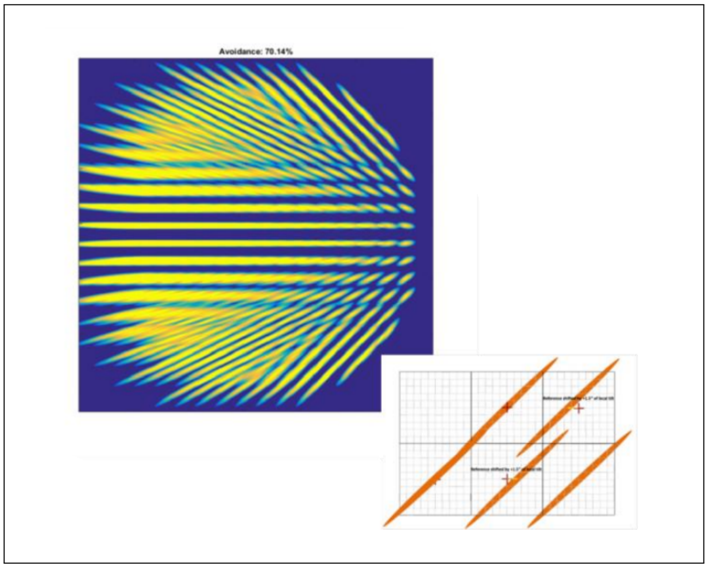

Figure 1.27: Example of spot elongations in the SH wavefront sensor (Credits Fusco et al. (2019))

1.7.1 Optical gains

The signal obtained from the NGS and the LGS may not be the same. A way to test how similar are the two signals is to compute an **optical transfer function** (OTF) matrix [1]. Mathematically, the OTF is obtained as

$$OTF = \mathbf{IMat}^{\dagger}_{NGS}\,\mathbf{IMat}_{LGS} \tag{1.47}$$

Where $\mathbf{IMat}_{NGS}$ is the interaction matrix using a point source as calibration and $\mathbf{IMat}_{LGS}$ using an elongated source as calibration (i.e. the signal obtained for every mode when using a LGS). Every column of the OTF matrix corresponds to the modal reconstruction of the signal obtained from the LGS using the NGS interaction matrix.

[1]This optical transfer function does not refer to the same optical transfer function obtained as the auto-correlation of the entrance pupil, but encodes the same purpose: to specify the frequency (or modal) response of the system. In this case, how the sensitivity to a KL modes changes when going from a diffraction limited source to a LGS

The diagonal terms of the OTF corresponds to the **optical gains** (or signal strength), which gives information about the relative amplitude of the signal produced by the LGS as seen by a NGS reconstructor. As an example, if the term $OTF_{11} = 0.5$, it means that for the same input aberration, the LGS produces half of the signal as the NGS for the first mode. The non-diagonal terms corresponds to the coupling between the modes when changing the source.

1.8 New wavefront sensor proposal

Considering that ELTs are being designed to use SH sensors (Uhlendorf et al., 2013), it seems appropriate to study the possibility of using other wavefront sensors. Various authors have proposed the use of a pyramid wavefront sensor as a replacement for the SH for ELTs, due to advantages such as adjustable sensitivity and dynamic range during operation (Esposito et al., 2016) and the lower number of pixels required for the detector (Esposito et al., 2016; Fusco et al., 2019). It has also been shown that, for an NGS, the PWFS has a similar or even better behavior than the SH in aspects such as limiting magnitude (Esposito and Riccardi, 2001), noise propagation (Fauvarque et al., 2017), sensitivity in diffraction limited and partial correction operation (Ragazzoni and Farinato, 1999), and closed loop operation (Vérinaud, 2004).

In this work, the performance of a wavefront sensor will be measured in terms of sensitivity, linearity, dynamic range and closed loop operation. The criteria for each quantity are:

- Linearity: The sensor is able to determine the amplitude of the aberration, without introducing measurement errors. The two main sources of non-linearity are: 1) the saturation zone, where the sensor is not able to determine the amplitude of the aberration and 2) when a single KL mode is introduced, the sensor outputs non-zero values for other modes. The sensor will be considered to be operating in a linear region when the RMS value of the measurement errors does not the fitting error.
- Sensitivity: Rate of change of the sensor signal as a function of the input aberration.

For a given modal aberration, the sensitivity to RON can be obtained as

$$s(\phi_i) = \frac{\sigma(\delta I(\phi_i))}{\sigma(\phi_i)} \tag{1.48}$$

and the sensitivity to photon noise can be obtained as

$$s_\gamma(\phi_i) = \frac{\sigma(\delta I(\phi_i)./\sqrt{I_0})}{\sigma(\phi_i)} \tag{1.49}$$

with I_0 the reference intensity and $./$ the element-wise division.

- Dynamic range: As RON or photon noise will not be included in the simulation, the ratio between maximum and minimum measurement would not give useful information, therefore the dynamic range will be defined as the range of amplitudes where the sensor's output is within 70% of the real value (3 dB drop).

- Closed loop operation and residual phase: When the adaptive optics system is running, not all of the atmosphere distortions are corrected. Therefore, the Strehl ratio and the RMS of the residual phase will be used as metrics for comparison between the NGS and LGS AO systems.

1.9 Objectives of the thesis

General objective:
To study the performance of a pyramid wavefront sensor with LGS compared to its behavior using an NGS.

Specific objectives:

1. To determine the linearity, sensitivity, dynamic range and closed loop operation of a pyramid wavefront sensor using: NGS and LGS.

2. To gain knowledge about the KL mode sensitivity losses when using an extended object.

2. LITERATURE REVIEW

Efforts to understand the behaviour of the PWFS when using LGS have been done before. In this chapter I will present some of the most resent publications on the subject. Each section will refer to one specific publication mentioned in its title.

2.1 "The Pyramid Wavefront Sensor with Extended Reference Source" (Pinna1a et al., 2011)

This work's purpose was to investigate the effects of 2D spot elongations of the reference object for a PWFS.

Using a laboratory optical setup, they were able to create a complete AO system. To generate the extended objects, they used optical fiber cores with different diameters as their sources, which resulted in objects who's on sky angular diameter ranged from a diffraction limited (DL) one up to 1.6" (> 40 times the diameter of the DL spot).

Using an Adaptive Secondary Mirror, they were able to generate atmospheric disturbances, with a 15 m/s wind and a 0.8" seeing. As they generated their own disturbances, they could measure them within a few nm of error and then use the KL modal residual of the AO corrections as metric for the performance for each spot size.

In their tests they found that the PWFS losses sensitivity as the size of the object increases. This result was in concordance with the literature, because the extension of the object acts as a spatial modulation, which is known to decrease the sensitivity (Vérinaud, 2004). Also, they found that when using a 1.6 " object, the sensitivity drop is similar to the effect that a loss in flux of up to one magnitude has for a diffraction limited object.

2.2 "Pyramid wavefront sensor performance with laser guide stars" (Quiros-Pacheco et al., 2013)

This work's aim was to characterizing the sensitivity for point sources, 2D and 3D objects.

2.2.1 2D elongation

For 2D objects, they found that the elongations acts in a similar way to the modulation of the spot on top of the pyramid. They found that with a modulation radius for a point object of $R_{TT} = \frac{R_{EO}}{2}$, with R_{EO} the angular size of the elongated object, the pyramid has the same sensitivity for both cases (point source with modulation and elongated object without modulation), but the elongated object had twice the dynamic range.

Then, they tested the noise propagation coefficients (NPC), which represents the sensitivity of the PWFS to phase noise. They built interaction matrices using 500 KL modes and 30×30 subapertures for the pyramid for three types of extended objects and three modulations amplitudes. NPC were calculated as

$$p_i^2 = (\mathbf{IMat}^t\mathbf{IMat})_{ii}^{-1} \tag{2.1}$$

The results they found confirmed that the sensitivity for the extended sources and their equivalent modulations had the same sensitivity. Also, they found that the sensitivity to noise increases with the size of the elongated object, which means that to obtain the same signal to noise ratio (SNR), a higher intensity source has to be used.

2.2.2 3D elongation

For the 3D object, they computed the radial sensitivity loss and noise propagation coefficients.

Their sensitivity computation consisted in introducing tilt to the system and then check the signal profile of the measurements. They found that as they got further away from the center of the pupils, the sensitivity decreases down to less than 50% at the edges.

Finally, they found that the NPC were tree to four times bigger in the case of the 3D elongated object when compared to the 2D objects, and up to 15 times bigger than the DL case.

2.3 “Use of Laser Guide Star with Pyramid Wavefront Sensor” (Blain et al., 2015)

This work’s main objective was to evaluate the performance in terms of sensitivity of the PWFS with LGS and compare it to the SH wavefront sensor.

They computed sensitivities for different KL modes and found that modulation decreases the overall sensitivity of the pyramid, which is in concordance with previous works.

For closed loop operations with 2D objects, they showed that both PWFS and SH wavefront sensors have similar performances, in term of residual phase, but the PWFS showed a slightly lower residual phase, in particular at low order modes.

2.4 “Pyramid wavefront sensing using Laser Guide Star for 8m and ELT class telescopes” (Esposito et al., 2016)

This work was designed to study of 3D elongated guide stars for 8 m and 40 m class telescopes.

Using incoherent summation, they modeled the LGS as a series of samples with different tilt and defocus coefficients.

2.4.1 8 m class telescope

For a 8 m class telescope, like the ones in the VLT, they generated interaction matrices for both PWFS and SH wavefront sensors, and found that NPC where similar in both cases, with the pyramid having slightly lower values. When running *end to end* simulations of closed loop operation, they found that the pyramid had a similar, if not slightly better performance than the SH sensor in terms of the Strehl ratio.

2.4.2 40 m class telescope

For the 40 m class telescope, they computed interaction matrices for both WFSs and found that the NPC for the pyramid were up to tree times as large as for the SH WFS. They ran end to end simulation for both sensors and found a similar performance in terms of Strehl ratio, but the key difference is that for the PWFS they used a 176×176 pixel detector (currently available) and for the SH WFS the used a 1600×1600, necessary for the sampling of elongated spots. Such a detector is not available with current technology. With this, they conclude that the PWFS could be an alternative to used in the new ELTs.

3. METHODS AND SIMULATIONS

3.1 Optical simulation description

To develop out this thesis, it was necessary to create a code that would allow the simulation of different processes and optical elements. All these aspects were done in Matlab using the OOMAO toolbox (Conan and Correia, 2014). The basis of this work consisted in the propagation of wave fronts. These wave fronts are of the form

$$\psi(x,y) = \sqrt{n}\,\mathbb{I}_p(x,y)\,e^{i\phi(x,y)} \tag{3.1}$$

with n the average flux in photons, $\mathbb{I}$ an indicative function of the entrance pupil and $\phi(x,y)$ a phase. Wavefront propagation will be explained later.

3.1.1 Optical elements and angular spectral propagation

Phase masks were mainly used to simulate optical elements. These masks can simulate lenses, mirrors or other elements by incorporating the effect on the phase that these components would have on the wavefront. Following Fauvarque et al. (2017), let x and y be the coordinates of the plane perpendicular to the optical axis, ψ the electromagnetic field (EM field) in its phasorial form just before passing through the phase mask, ϕ_{mask} the phase incorporated by the mask and $\mathbb{I}_{mask}$ the function indicative of the aperture of the mask. The field resulting from applying a phase mask is

$$\psi_{new}(x,y) = \psi(x,y)\,\mathbb{I}_{mask}(x,y)\,e^{i\phi_{mask}(x,y)} \tag{3.2}$$

For spectral propagation, an algorithm based on Fast Fourier Transform (FFT) is used for Fresnel diffraction presented in Mas et al. (1999). If the Fresnel equation is considered with the paraxial approximation, the electro-magnetic field propagated a distance Δz can be obtained as

$$\psi'(x_2,y_2) = \frac{e^{ik\Delta z}}{i\lambda\Delta z}\iint_{\mathbb{R}^2}\psi(x_1,y_1)e^{i\frac{k}{2\Delta z}\left[(x_1-x_2)^2+(y_1-y_2)^2\right]}dx_1dy_1 \tag{3.3}$$

with k the wave number, (x_1, y_1) the source plane coordinates, (x_2, y_2) the coordinates of the propagated plane and the $'$ symbol representing that the wavefront was propagated (if the wavefront was propagated twice, the symbol would be $''$). Using properties of convolution (denoted by $*$), the equation can be expressed as

$$\psi'(x_2, y_2) = \psi(x_1, y_1) * \left[\frac{e^{ik\Delta z}}{i\lambda\Delta z} e^{i\frac{k}{2\Delta z}x_1^2 + y_1^2}\right] \tag{3.4}$$

Using properties of the Fourier transform it is possible to reduce the computation time substantially. The expression of the propagated field is

$$\psi'(x_2, y_2) = \mathcal{F}^{-1}[(f_{x1}, f_{y1}), (x_1, y_1)]\{H(f_{x1}, f_{y1})\mathcal{F}[(f_{x1}, f_{y1}), (x_1, y_1)]\{\psi(x_1, y_1)\}\} \tag{3.5}$$

with $\mathcal{F}[(f_{x1}, f_{y1}), (x_1, y_1)]\{\}$ the Fourier transform from source space to space frequency space $(f_{x1}, f_{y1}) = \left(\frac{x_1}{\Delta z\lambda}, \frac{y_1}{\Delta z\lambda}\right)$ and

$$H(f_{x1}, f_{y1}) = e^{ik\Delta z} e^{-i\pi\lambda\Delta z(f_{x1}^2 + f_{y1}^2)}$$

3.1.1.1 Implementation in matlab

The OOMAO toolbox allows the creation of several objects, such as a star, an atmosphere, telescopes, DMs, WFS' and others. The toolbox is made in such a way that the propagation is done with the $*$ symbol. As an example, if we have a star, a telescope and a detector objects, we can simulate the propagation as

$$star * telescope * detector \tag{3.6}$$

Then, we can retrieve the image from the detector using the detector.frame command (see figure 3.1).

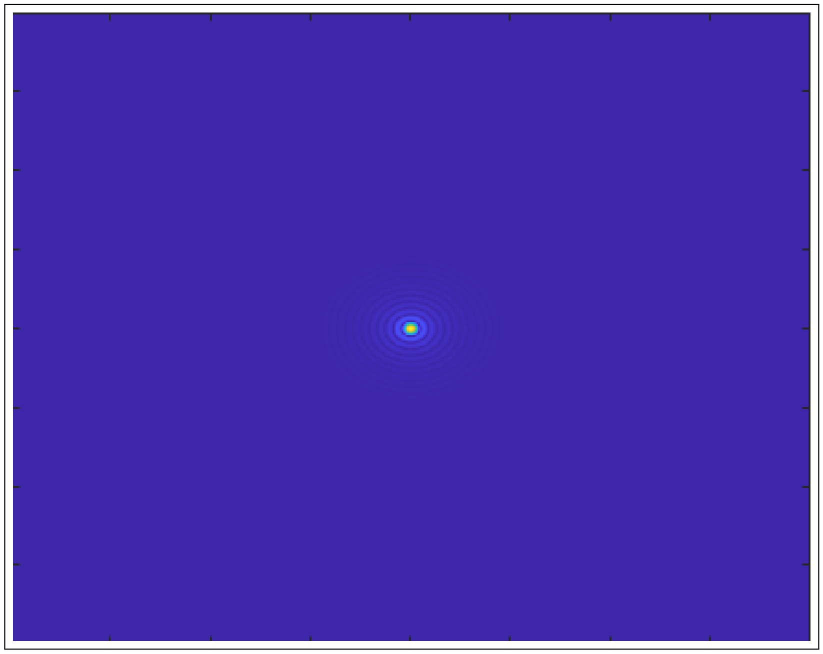

Figure 3.1: Diffraction limited image of a star using the OOMAO toolbox

For buildup, the star object receives as parameter the observing wavelength

Observing wavelength : 589 nm

The detector object receives as parameter the field of view in λ/D's

Field stop size : 40

The telescope object will be explained in section 3.1.3.1.

3.1.2 Phase distortions

The phase aberrations used in this work are generated using the Von Karman model.

Let FC be a $N \times N$ matrix of complex random coefficients with distribution $\mathcal{N}(0,1)$. The simulated atmospheric phase aberration can be obtained as

$$\phi = \Re e \left(\mathcal{F}^{-1}[(f_{x1}, f_{y1}), (x_1, y_1)]\{FC \cdot \sqrt{C_\phi(f_{x1}, f_{y1})}\} \right) \tag{3.7}$$

Figure 3.2 shows the process to generate atmospheric disturbances following the Von Karman model

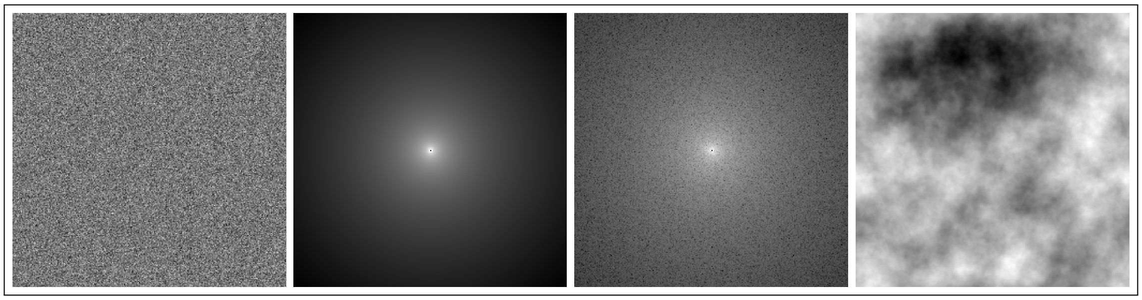

Figure 3.2: Simulation of atmospheric aberration using the Von Karman model with the following parameters: $r_0 = 20\,cm$, $N = 256$, $L_0 = 10\,m$ and $l_0 = 1\,cm$. From left to right, the first image corresponds to the random coefficients with distribution $\mathcal{N}(0, 1)$. The second image corresponds to the logarithm of the square root of the power spectrum corresponding to equation 1.11. The third image corresponds to the logarithm of the element-by-element multiplication of the two previous images. The fourth image is the simulated atmospheric phase aberration, corresponding to equation 3.7

3.1.2.1 Implementation in matlab

Using the OOMAO toolbox, it was possible to define an atmosphere. It receives as input the r_0, L_0, and the altitude, relative turbulence intensity, wind speed and direction for each turbulent layer as a list denoted with square brackets.

For the no wind scenario, the parameters introduced to the atmosphere object were

r_0	:	0.15 m
L_0	:	20 m
layer heights	:	[1000 5000] m
fractional r_0	:	[0.8 0.2]
layer wind speeds	:	[0 0] m/s
layer wind direction	:	[$3\pi/4$ $\pi/4$]

For the low wind scenario, the parameters introduced to the atmosphere object were

r_0	:	0.15 m
L_0	:	20 m
layer heights	:	[1000 5000] m
fractional r_0	:	[0.8 0.2]
layer wind speeds	:	[5 5] m/s
layer wind direction	:	[$3\pi/4$ $\pi/4$]

For the high wind scenario, the parameters introduced to the atmosphere object were

r_0	:	0.2 m
L_0	:	20 m
layer heights	:	[1000 5000] m
fractional r_0	:	[0.8 0.2]
layer wind speeds	:	[10 10] m/s
layer wind direction	:	[$3\pi/4$ $\pi/4$]

Then using the $+$ symbol, it was possible to couple the atmosphere to the telescope, so when propagating the star to the telescope, it takes into account the distortions produced by the atmosphere. As an example, if we had a star, an atmosphere, a telescope and a detector, first we couple the atmosphere to the telescope as

$$telescope = telescope + atmosphere \tag{3.8}$$

and then we propagate the star to the telescope (through the atmosphere) and to the detector

$$star * telescope * detector \tag{3.9}$$

As before, we can retrive the image of the distorted star using the detector.frame command (see figure 3.3).

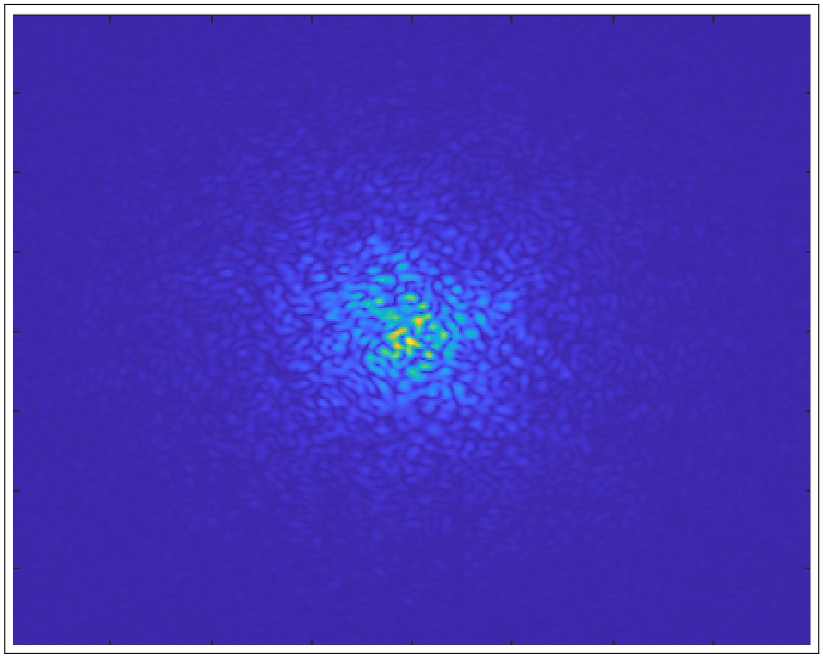

Figure 3.3: Image of a distorted star using the OOMAO toolbox

Then, using a OOMAO specific syntax operation, it is possible to update the atmosphere such that is evolves according to the wind speed and direction. To do this, the command $+telescope$ is used. Summing up several images, it is possible to simulate a long exposure.

3.1.3 Telescope, DM and pyramid

The telescope was simulated using a circular aperture with no central obstruction. Considering equation 3.1, the phase, aperture function and average flux for the EM field at the entrance pupil are

$$\begin{aligned} \phi_{tel} &= -k\frac{x_p^2+y_p^2}{2f_{efl}} \\ \mathbb{I}_{tel} &= \begin{cases} 1 & \text{for } x_p^2+y_p^2 \leq D^2/4 \\ 0 & \text{for } x_p^2+y_p^2 > D^2/4 \end{cases} \end{aligned} \tag{3.10}$$

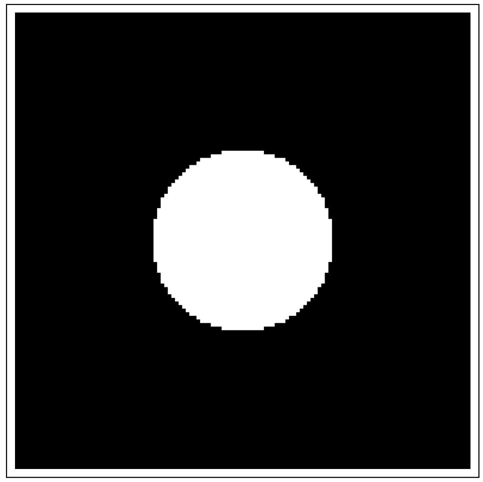

Figure 3.4: Image of telescope aperture

with x_p and y_p the coordinates in the entrance pupil's plane and f_{efl} the effective focal length of the telescope. The magnitude of the source is later added after a normalization of the image. This produces the electromagnetic field at the entrance pupil

$$\psi_{tel} = \mathbb{I}_{tel}\, e^{i\phi_{tel}} \tag{3.11}$$

To add a phase aberration, ϕ_{abr} must be added to the phase of the telescope ϕ_{tel}. A phase mask is assembled and added to the entrance EM field, using expression 3.2.

Light gets propagated a distance equal to the focal length using equation 3.5 and the field obtained in the image plane (or Fourier plane) is $\psi'(x_i, y_i)$ with x_i and y_i the coordinates in the image plane.

Once the light reaches the image plane, the phase of the pyramid must be incorporated into the EM field. The phase incorporated by the pyramid has the following form

$$\phi_{pyr} = k\,(|x_i| + |y_i|)\frac{D}{4f_{efl}} \tag{3.12}$$

Finally, the phase mask of the pyramid is added using expression 3.2 and propagates a distance equal to the focal length using equation 3.5, where $\psi''(x_d, y_d)$ is obtained. (x_d, y_d) are the coordinates of the detector plane. The intensity registered by the detector is obtained as

$$I_d = |\psi''(x_d, y_d)|^2 \tag{3.13}$$

This image is then normalized such that all the sum of the values in all the pixels add up to one, and then multiplied by the number of photons that should arrive at the detector given the magnitude of the source and the efective area of the telescope.

3.1.3.1 Implementation in matlab

Using the OOMAO toolbox, it was possible to define a telescope, DM and pyramid WFS. As input for the telescope object, it receives the diameter, field of view, resolution (pixels in the diameter) and sampling time. The DM object receives the KL modal base (obtained using an OOMAO function), the resolution of the wavefront and the useful actuators. For the pyramid wavefront sensor, the OOMAO class receives as input the number of pixels per pupil, the resolution of the wavefront and the modulation amplitude in multiples of λ/D.

As before, for the propagation every object has to be included.

$$star * telescope * dm * pyramid \tag{3.14}$$

The pyramid object comes with its own detector, so in order to obtain the signal, the command pyramid.camera.frame is used (see figure 3.5).

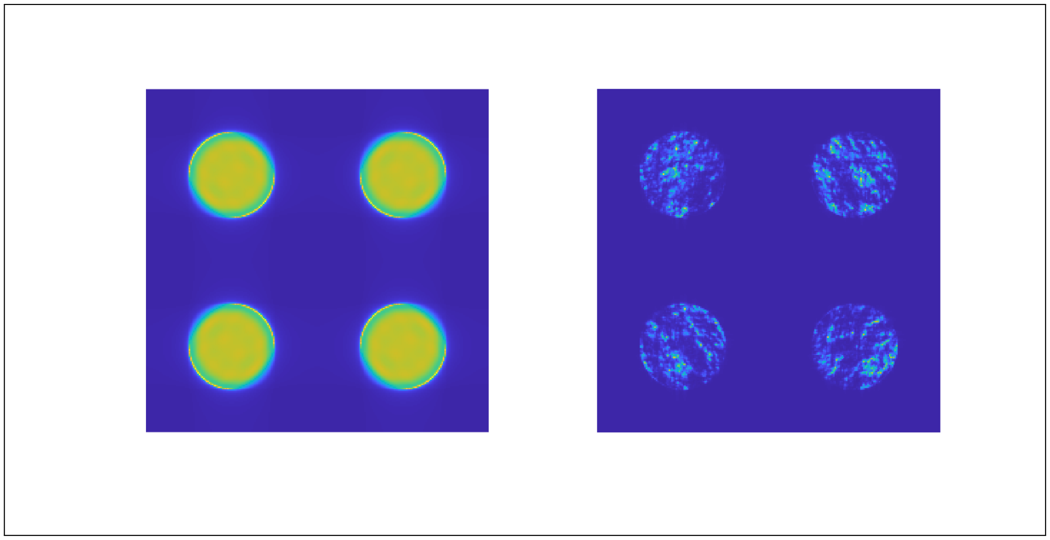

Figure 3.5: Left panel: image of the four pupils for a propagation without atmosphere (i.e. the reference intensity); right panel: image for a propagation through atmosphere.

3.1.4 LGS

Following what was done by Esposito et al. (2016), in order to simulate a LGS it was necessary to discretize the sodium layer into samples and make an incoherent sum of the contribution of each one to the measurement.

In Esposito's work the LGS was uniformly sampled. For this, the sodium layer was separated into slices, each one separated vertically by a distance of 1 km, covering from 85 to 95 km. Each slice had radially distributed samples $5\lambda/D$ apart from each other, therefore sampling the 3D structure of the laser beacon. Then, using a sodium density profile (see figure 3.6) each sample's intensity was scaled to take into account relative distribution of sodium atoms in the atmosphere.

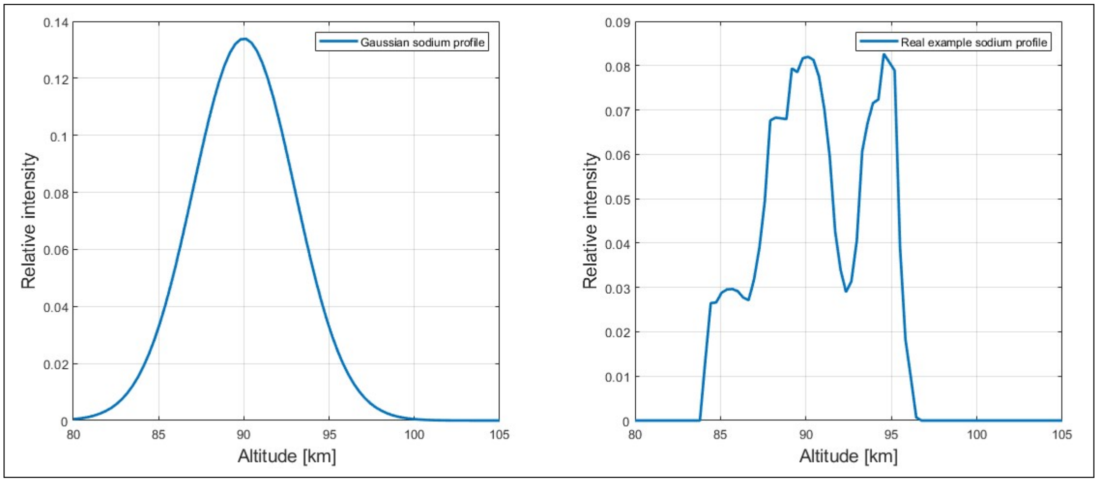

Figure 3.6: Left panel: a simple Gaussian sodium profile with 7 km FWHM; right panel: double peak sodium profile (real example of a profile from Pfrommer and Hickson (2014)).

There are several problems with the uniform sampling technique.

- There are many points that have little contribution to the system due to their low intensity, but are equally expensive computationally.
- Large portions of the LGS are not sampled, therefore it is difficult to test real like sodium profiles.
- The periodicity of the samples can introduce unwanted structures given by the symmetry of the grid used for the sampling.

Therefore, in this work a Monte Carlo approach was used to sample the LGS. We can use the relative distribution of the sodium atoms as a probability density function, and generate a random set of samples that follows that distribution. The amount of samples will be explained in section 3.1.6

To generate the 3D structure, X and Y coordinates are randomly generated using a Gaussian distribution. The X coordinate is centered at $\overline{x} = 0\,m$ and with a standard deviation of $\sigma_x = \frac{90000\,m}{206265\sqrt{8\ln 2}}$ (FWHM = 1" @90 km). The Y coordinate is centered at $\overline{y} = D/2\,m$ (laser launch telescope located at the side of a telescope with diameter D pointing straight up) and with the same standard deviation as the X coordinate $\sigma_y = \sigma_x$. For the Z coordinate, it is randomly generated using the desired probability density function that mimics the sodium profile. Figures 3.7 and 3.8 shows the 3D sampling of the LGS with each coordinate's generated probability density function.

This approach assumes the telescope is pointing at zenith (orthogonal to the sodium profile). This assumption will be used throughout the simulations. In order to simulate the pointing of the telescope the focus and z distribution of the samples may be adjusted by the elevation angle γ (measured from the zenith). Using the parallel-plane atmosphere approximation, the focus of the telescope should be adjusted multiplying its values by the secant of the elevation angle, as shown in equations 3.15 and 3.16

$$focus_{new} = focus\, sec(\gamma) \tag{3.15}$$

$$Z\_coordinate_{new} = Z\_coordinate\, sec(\gamma) \tag{3.16}$$

This approach assumes that the distribution of sodium atoms does not change significantly with respect to the location where the laser enters the layer and where it exits it. To include the possibility of changing the aim of the laser launch telescope, the X and Y coordinates should also include a correction factor as follows

$$X\_coordinate_{new} = X\_coordinate + Z\_coordinate\, tan\theta_0\, cos\phi_0 \tag{3.17}$$

$$Y\_coordinate_{new} = Y\_coordinate + Z\_coordinate\, tan\theta_0\, sin\phi_0 \tag{3.18}$$

with θ_0 and ϕ_0 the angles in spherical coordinates of the laser launch telescope with respect to the pointing of the telescope.

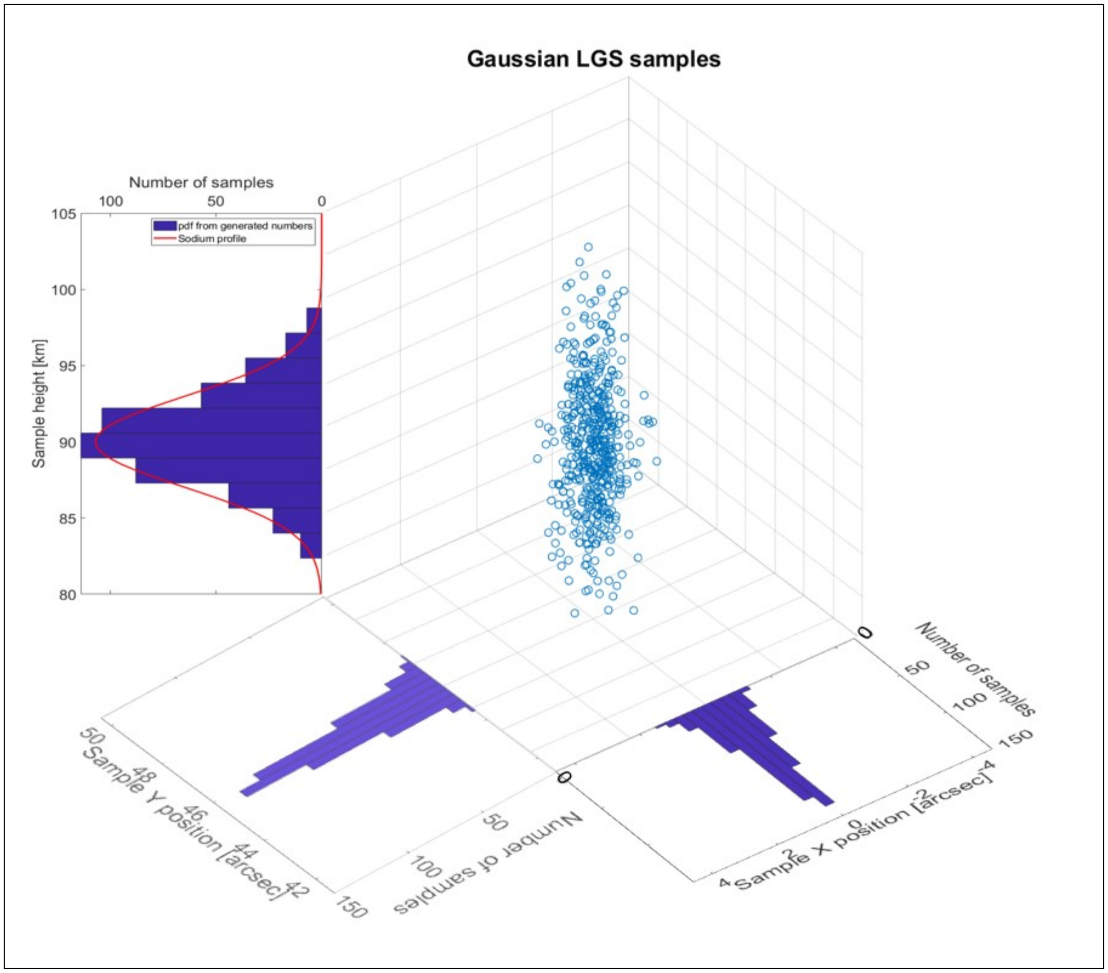

Figure 3.7: Gaussian sampling of the LGS following the sodium distribution from the left image in figure 3.6. Note that the **y** axis is not centered at zero because of the laser being shot straight up from the side of the telescope

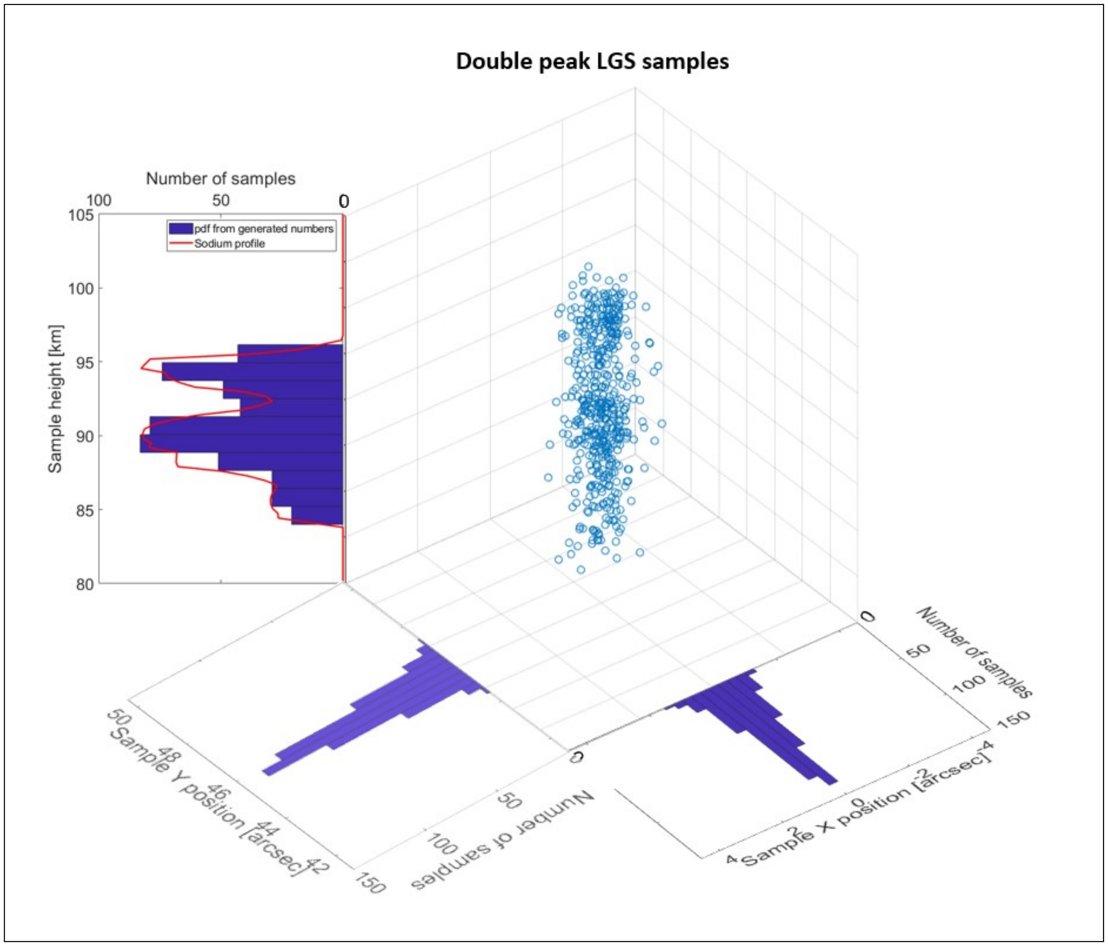

Figure 3.8: Real-like sampling of the LGS following the sodium distribution from the right image in figure 3.6.

Using the center of the telescope as the origin, each sample of the LGS had a (x_m, y_m, z_m) coordinate. As each point radiates light spherically, the phase of the wavefront can be obtained as the sum of a focus coefficient given by the distance from the sample to the telescope, and a tip/tilt given by the x_m and y_m coordinates.

$$\begin{aligned}\phi_{tilt,\,m} &= k\,atan\left(\frac{x_m}{z_m}\right)x_p\\ \phi_{tip,\,m} &= k\,atan\left(\frac{y_m}{z_m}\right)y_p\\ \phi_{focus,\,m} &= k\,\frac{(x_p^2+y_p^2)}{2r_m}\end{aligned}\tag{3.19}$$

with $r_m = \sqrt{x_m^2 + y_m^2 + z_m^2}$. The phase expressions in 3.19 must be incorporated to the phase in 3.10

$$\begin{aligned}\phi_{LGS_m} &= \phi_{tilt,\,m} + \phi_{tip,\,m} + \phi_{focus,\,m}\\ \mathbb{I}_{LGS_m} &= \begin{cases}1 & \text{for } x_p^2 + y_p^2 \leq D^2/4\\ 0 & \text{for } x_p^2 + y_p^2 > D^2/4\end{cases}\end{aligned}\tag{3.20}$$

With this, a phase mask is assembled and added to the EM field of the entrance of the telescope in equation 3.11, obtaining

$$\psi_{tel\_LGS_m} = \mathbb{I}_{LGS_m}\, e^{i\phi_{tel\_LGS_m}}\tag{3.21}$$

with $\phi_{tel\_LGS_m} = \phi_{tel} + \phi_{LGS,\,m}$. Two methods were explored for the propagation.

3.1.4.1 Method 1: Complete propagation

For each of the sample points for the LGS, a complete propagation was carried out through the telescope and the pyramid sensor. The telescope's diameter and focal length matched the VLT parameters (due to computational issues, the ELT could not be simulated as it required operating on matrices of up to 100 GBytes)

For the telescope, the parameters for the object were

Telescope diameter	:	8.2 m
Field of view	:	2.5 arcmin
Resolution	:	2600 pix
Sampling time	:	2 ms

For the DM, the parameters for the object were

Modes	:	400 KL modes
Resolution	:	2600 pix

For the pyramid using the NGS, the parameters for the object were

Pupil resolution	:	60 pix
Resolution	:	2600 pix
Modulation	:	4 λ/D

For the pyramid using the LGS, the parameters for the object were

Pupil resolution	:	60 pix
Resolution	:	2600 pix
Modulation	:	0 λ/D

The image of the LGS can be obtained by adding all the intensities obtained in the image plane

$$LGS_{image} = \sum_m |\psi'_{VLT\_LGS_m}(x_i, y_i)|^2 \tag{3.22}$$

In a similar way, the intensity that is recorded in the detector is

$$I_{d,LGS} = \sum_m |\psi''_{VLT\_LGS_m}(x_d, y_d)|^2 \tag{3.23}$$

Figure 3.9 shows the images of the LGS as seen through the telescope for both sodium profiles, and figure 3.10 shows the reference intensity for both cases.

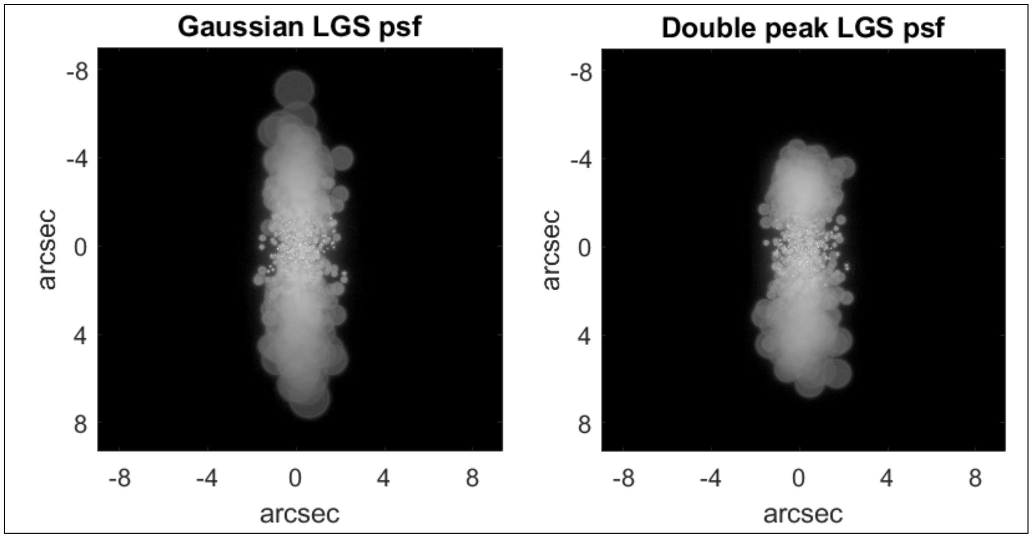

Figure 3.9: Log scale images of the simulated LGS as seen through the telescope. Left panel: Gaussian sodium profile; right panel: Double peak sodium profiles.

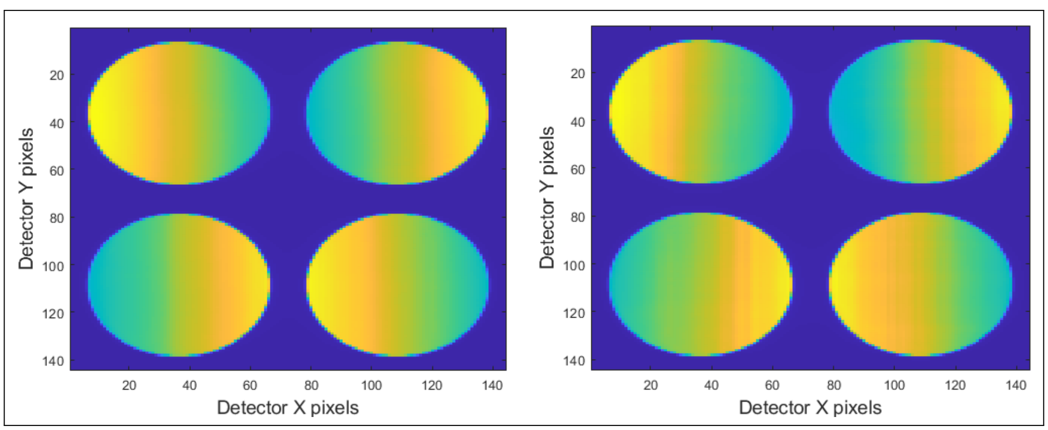

Figure 3.10: Simulated reference intensities. Left panel: Gaussian sodium profile; right panel: Double peak

The problem with this method is that for every sample, the whole pyramid is being simulated, even though only a small portion of it interacts with the light. Figure 3.11 represents the path the light takes from the LGS to the detector and figure 3.12 represents the path the light takes from a single sample to the detector

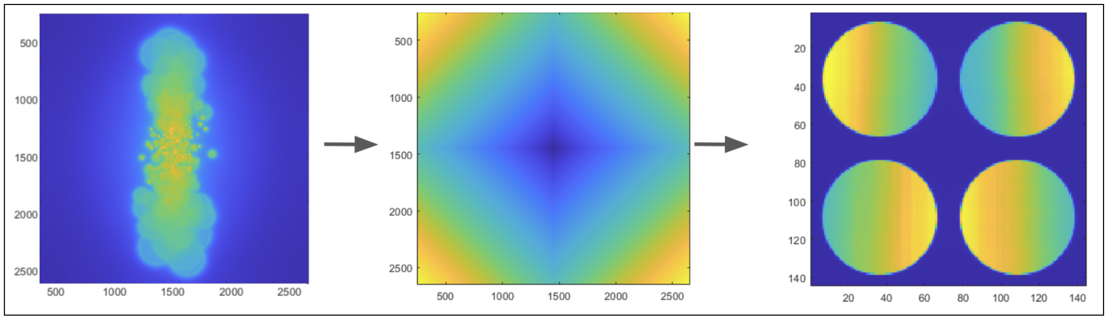

Figure 3.11: Representation of light path from LGS to detector (all units in pixels). Left image: LGS psf; center image: pyramid; right image: pupils in the detector

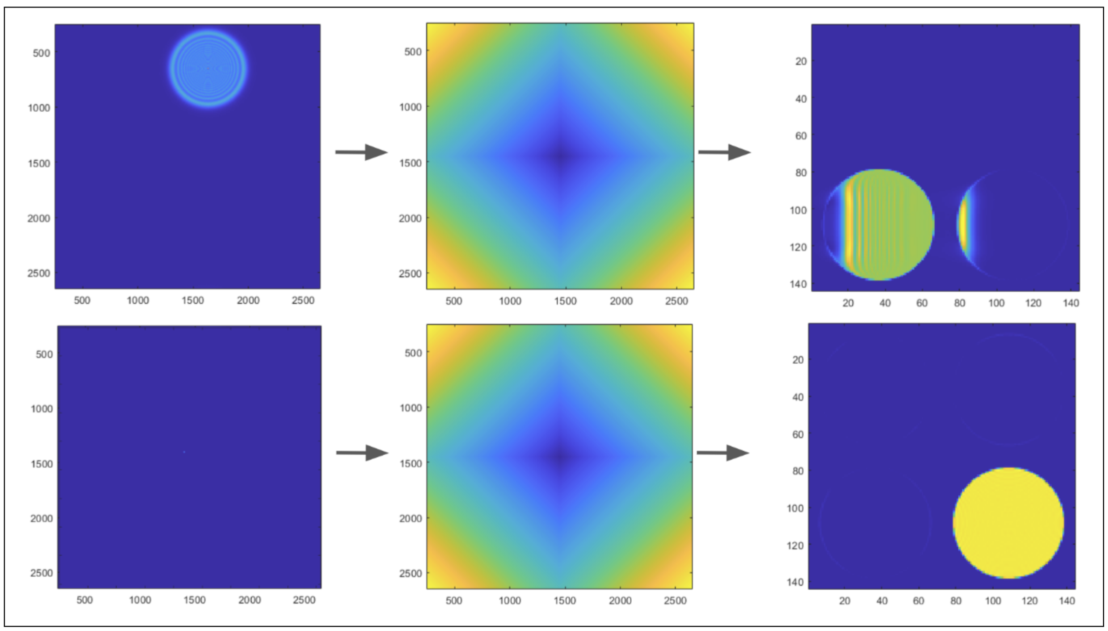

Figure 3.12: Representation of light path from a single sample to detector (all units in pixels). **Top row: Lower edge sample.** Left image: sample psf; center image: pyramid; right image: pupils in the detector. **Bottom row: Near center sample.** Left image: sample psf (as sample is near perfect focus, it looks only as a dot at the center of the image); center image: pyramid; right image: pupils in the detector.

As it's possible to observe in figure 3.12, each sample only interacts with a small portion of the pyramid. This effect is even more important for samples near the center that are in focus (bottom row figure 3.12), as they use a smaller number of pixels. As each propagation for every sample has to simulate the complete pyramid, much of the memory and computation times are wasted.

Different telescope diameters were simulated and the computation time recorded to observe a general trend and to see what to expect when simulating a 40 m telescope. Figure 3.13 shows an approximation for the computation times for different telescope diameters

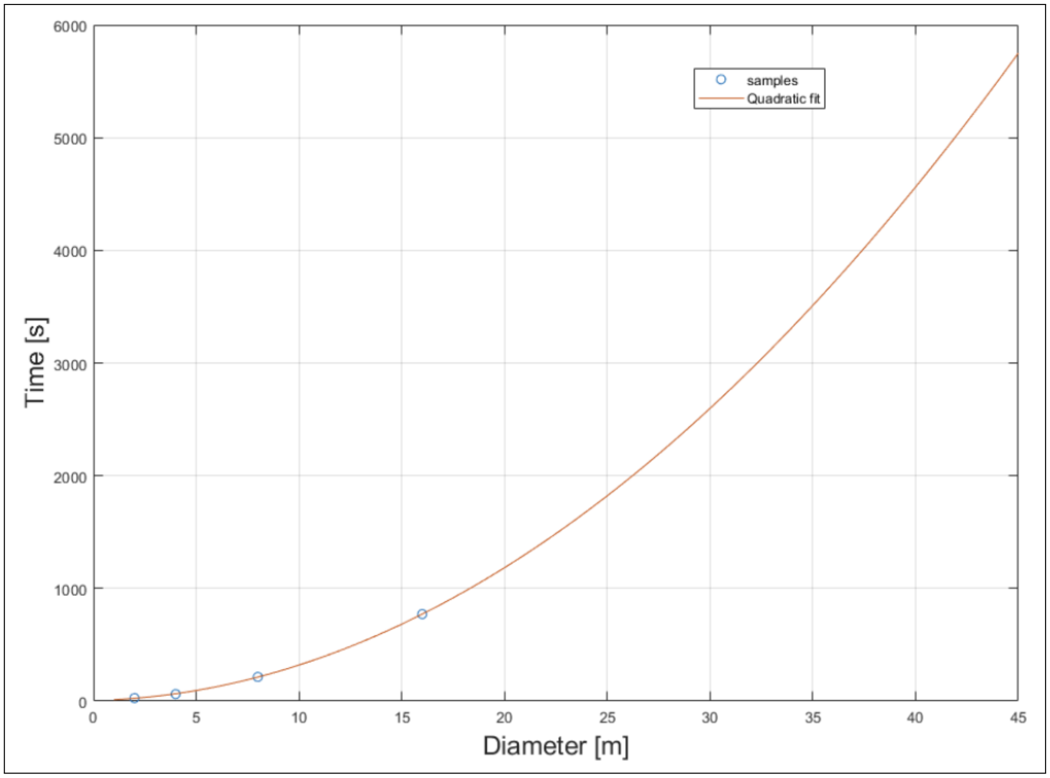

Figure 3.13: Computation time for the propagation of different telescope diameters

The graph on figure 3.13 shows that each frame of simulation for a 40 m telescope would take more than an hour. As an example, to build the interaction matrix for 400 modes, 800 frames are needed, meaning over a month of simulation time.

As for the memory issues, in order to have enough pixels to have the whole LGS in every frame for a 40 m telescope, more than 100 GBytes of RAM are needed.

3.1.4.2 Method 2: Portion propagation

The idea is to use only the portion of the pyramid each samples interacts with. Due to the height of each sample, the defocus coefficient will expand the image of the star. For this, the simulation was divided into three regimes:

- Inner regime: samples between 88 and 92 km
- Middle regime: samples between 85 and 95 km (and outside the inner regime)
- External regime: samples lower than 85 km or higher than 95 km

For each regime a suitable sized telescopes, pyramids and DMs were created, smaller for the inner regime and bigger for the external (in the resolution parameter for the objects, the list [240 480 960] is used as an abbreviation of the three separate objects used with different sizes).

For the telescope, the parameters for the object were

Telescope diameter	:	8-40 m
Field of view	:	2.5 arcmin
Resolution	:	[240 480 960] pix
Sampling time	:	2 ms

For the DM, the parameters for the object were

Modes	:	400 KL modes
Resolution	:	[240 480 960] pix

For the pyramid using the NGS, the parameters for the object were

Pupil resolution	:	60 pix
Resolution	:	240 pix
Modulation	:	4 λ/D

For the pyramid using the LGS, the parameters for the object were

Pupil resolution	:	60 pix
Resolution	:	[240 480 960] pix
Modulation	:	0 λ/D

Then, with the on-sky X and Y coordinates of each sample (figures 3.7 and 3.8), the corresponding x and y positions in the detector for each sample were computed and instead of adding a tip/tilt to each sample, the pyramid itself was translated the computed amount. With this, each sample has to be propagated in a straight line, therefore needing a small field of view (small number of pixels) and the pyramid translation is in charge of compensating for the physical position of the sample. Figure 3.14 shows examples for the propagation in the three regimes and figure

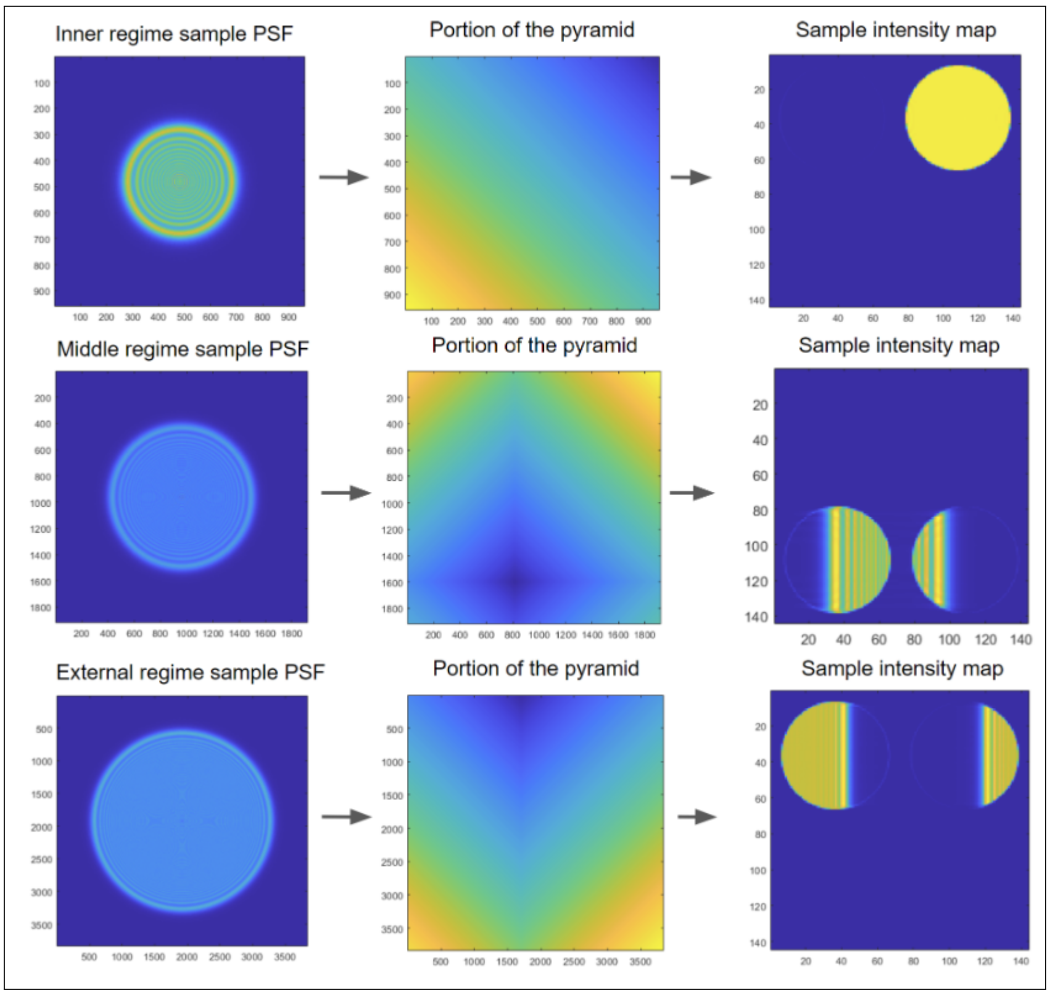

Figure 3.14: Light path from samples from the three regimes. All labels are in pixels. Top row: example from inner regime; middle row: example from middle regime; bottom row: example from external regime

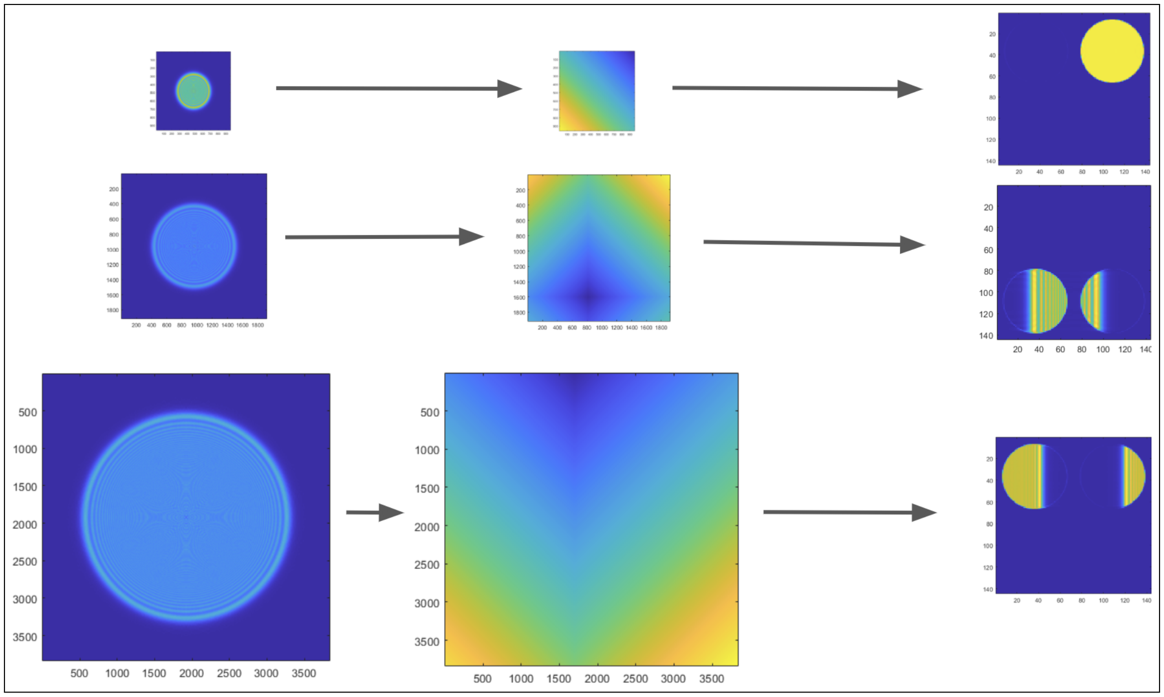

Figure 3.15: Same figure as 3.14, but scaled with the size of the matrices.

As most of the samples are in the inner or middle regime (refer to figure 3.7 to see height distribution), computation times are shorten by a factor of over 60 when simulating 20 m telescopes, going from 1200 to 17 seconds per iteration.

To test the validity of the method, complete propagation of the LGS (method 1) was performed for several test cases, and the average difference in the measurements between the two methods was lower than 0.001%, meaning that the second method outputs the same information as the first, but in a fraction of the time. For this work, the method of **Portion propagation** was used with telescopes with diameter 8, 16, 32 and 40 m. Using several diameters will allow to observe a trend that will provide information on what to expect when using the extremely large telescopes.

3.1.5 Interaction matrix

Interaction matrices were computed for a point source, like an NGS, and for two sodium profiles for the LGS, showed in figure 3.6. To do this, phase masks were used to introduce a positive and negative phase for the push-pull method. In this case the phase corresponded to each KL mode as

$$\phi_{\pm KL,j} = \pm\epsilon\, KL_j(r/R,\theta) \tag{3.24}$$

This phase was introduced to the entrance electromagnetic flied and propagated twice, once with the positive amplitude and the other with the negative amplitude. For the LGS, this process had to be repeated for every sample. Then, using equation 1.22 it was possible to obtain each column of the IMat.

3.1.6 Number of samples in LGS

As the LGS is being discretely sampled, it is important to have enough points such that the results are not affected by under-sampling. In a real-life situation there are more than tens of trillion atoms that act as point sources when the laser excites them, but in a simulation perspective that amount of samples is unreachable. Therefore, a simulation experiment was conducted where several interaction matrices with different number of samples were computed for some KL modes, to observe the evolution of the sensitivity with respect to the number of samples. Then, the number of samples for the LGS can be found as the quantity of point sources from which the sensitivity does not evolve when increasing its number. Figure 3.16 shows the sensitivity evolution with respect to the number of samples.

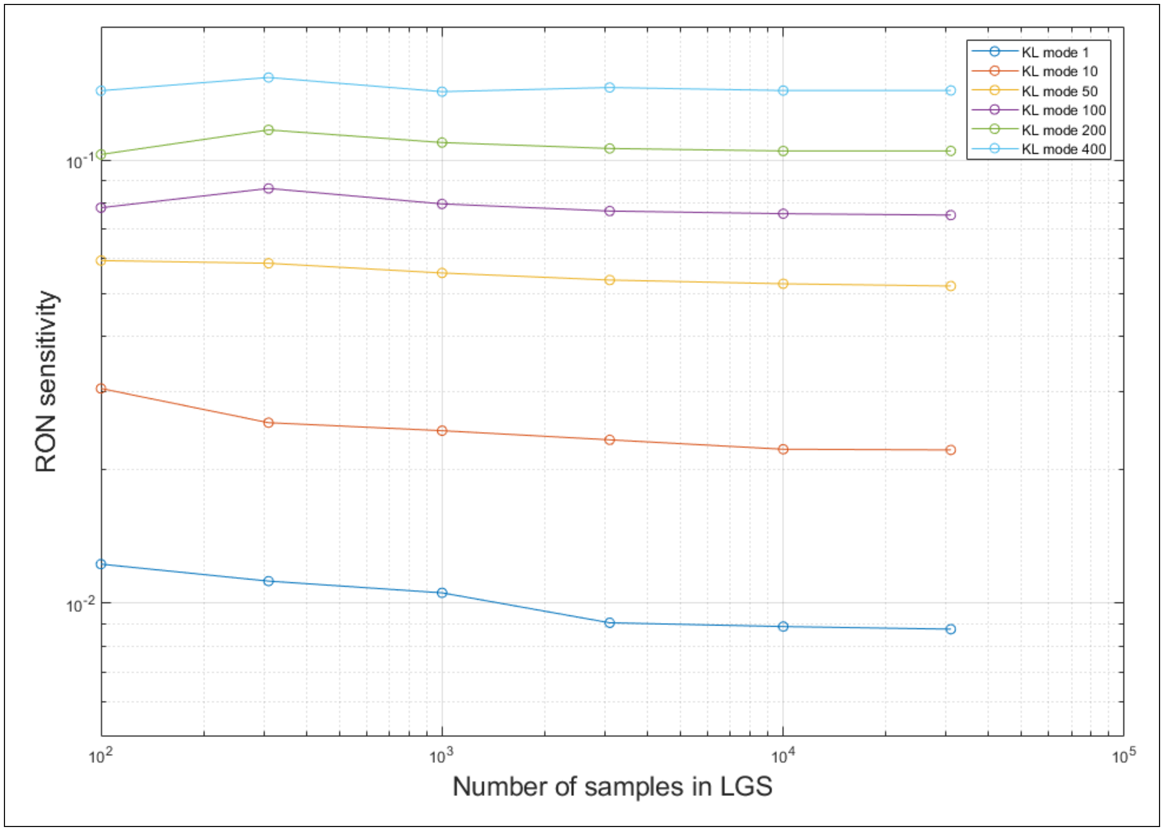

Figure 3.16: Read out noise sensitivity evolution with respect to the number of samples for different KL modes.

From 3.000 samples onward all the modes are within 10 % of the steady state value, and at 10.000 samples they are at less than 2 %. Using this information, it was decided that all the simulations should be done with 10.000 samples.

3.2 Noise

The two main sources of noise when dealing with a detector are read out noise and photon noise. As the laser stars are usually bright, read out noise can be neglected, therefore, the main component of noise in the system is given by the discrete nature of photons. As each arrival of a photon is a discrete event, it is possible to deduce that they will follow a Poisson distribution. With this, photon noise can be introduced to the simulation by having each pixel in the pupils image follow a Poisson distribution with mean the pixel's value and deviation equal to it's square root.

A typical LGS has a magnitude of around 7-9 (Chin et al., 2016), therefore it is possible to calculate the amount of photons that should arrive at the detector in each frame. Also, the magnitude of the LGS (or NGS) can be artificially increased or decreased, in order to estimate the limiting magnitude of the system.

3.3 Description of the simulations

3.3.1 Linearity and dynamic range

In order to study linearity and dynamic range, an simulation was designed that consisted of "showing" the wavefront sensor each KL mode individually, varying the input amplitude Γ, to then obtain the modal decomposition of the reconstructed wavefront by the sensor. In this reconstructed wavefront, the amplitude of the introduced mode (diagonal term) was recorded as the measurement and the RMS value of all the modes other than the one introduced (non-diagonal terms) was calculated and recorded as an error.

To "show" the pyramidal sensor each KL mode, phase masks were used again. In this case the phase corresponded to each KL mode as

$$\phi_{KL,j} = \Gamma KL_j(r/R, \theta) \tag{3.25}$$

with Γ a constant to control the amplitude of the aberration. This phase mask was added to the entrance's EM field using the expression 3.2. With this, the wavefront that was propagated for the natural guide star was

$$\psi(x_p, y_p) = \mathbb{I}_{tel}\, e^{i(\phi_{tel}+\phi_{KL,j})} \tag{3.26}$$

For the artificial guide star, the propagated fields were of the form

$$\psi_m(x_p, y_p) = \mathbb{I}_{LGS_m}\, e^{i(\phi_{tel\_LGS_m}+\phi_{KL,j})} \tag{3.27}$$

The dynamic range of each mode was obtained as the range of amplitudes were the measurement was within 70% of the input amplitude.

Linearity, or linear range, was obtained as the range of amplitudes in which the error was less than the fitting error, given a telescope with $D = 20\,m$, 400 actuators and $r_0 = 0.2\,m$.

3.3.2 Sensitivity losses and optical gains

To compute the sensitivity losses, expression 1.48 was used in every column of the interaction matrices to obtain the sensitivity to RON, and expression 1.49 to obtain the sensitivity to photon noise. The same procedure was also repeated for pure sine and cosine modes, with vertical and horizontal directions because it is possible to assume that, because of the shape of the LGS, different directions of spatial frequencies will be measured differently. Due to the elongation (and modulation effects), vertical frequencies should have less sensitivity than horizontal ones (figure 3.17 shows examples of both frequencies).

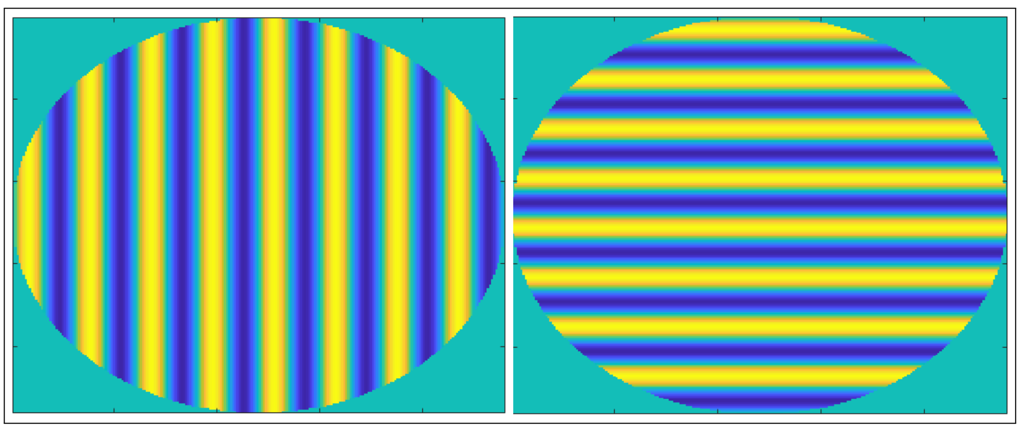

Figure 3.17: Pure sinusoidal modes. Left panel: horizontal frequency; right panel: vertical.

In the case of the pure sinusoidal modes, the global sensitivity was computed as

$$s = \sqrt{s_{sine}^2 + s_{cosine}^2} \tag{3.28}$$

For the optical gains, expression 1.47 was used for the two LGS examples.

3.3.3 Closed loop operation

To simulate a closed loop operation, the following block diagram was used

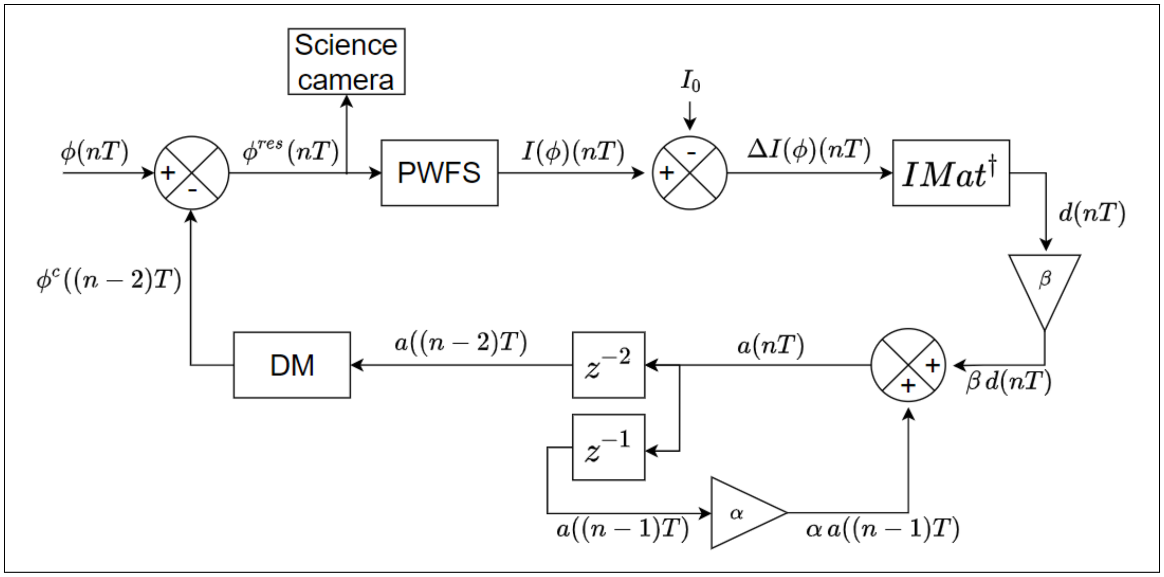

Figure 3.18: Closed loop implementation diagram.

The notation for the diagram is

n	:	number of iteration
T	:	sampling time
$\phi(nT)$	:	Input phase
$\phi^{res}(nT)$	:	Residual phase
$\phi^c(nT)$	:	Reconstructed phase
$I(\phi)(nT)$	:	Intensity map given by the PWFS
I_0	:	Reference intensity
$\Delta I(\phi)(nT)$	:	vectorized meta intensity
$d(nT)$	:	modal reconstruction of the phase / measurement
β	:	loop gain
$a(nT)$	:	command to the DM
α	:	leak factor
z^{-x}	:	x cycles delay

This closed loop was implemented for five cases:

- Natural guide star with point source calibration
- Both laser guide star profiles with point source calibration
- Both laser guide star profiles with elongated source calibration

3.3.4 Wind simulation

Different wind scenarios were tested: no wind, low wind $5\,m/s$ and high wind $10\,m/s$.

For each iteration of the control loop, a “science” star gets propagated through the atmosphere and corrected by the DM, then using a perfect star as reference, the Strehl ratio and residual phase RMS were recorded during the simulation, to be used as metric for the performance in closed loop operation.

4. SIMULATION RESULTS AND DISCUSSION

4.1 Optical gains

4.1.1 LGS optical gain maps

As the propagation has to be incoherent for every sample of the LGS, it was possible to observe the optical gains for each sample independently. For this, a toy model of the LGS was build, with uniform sampling, to see how the optical gains evolves with it's structure. To do this, the interaction matrix for the NGS was used to reconstruct the signal obtained for every sample. Figure 4.1 shows tree examples for different KL modes.

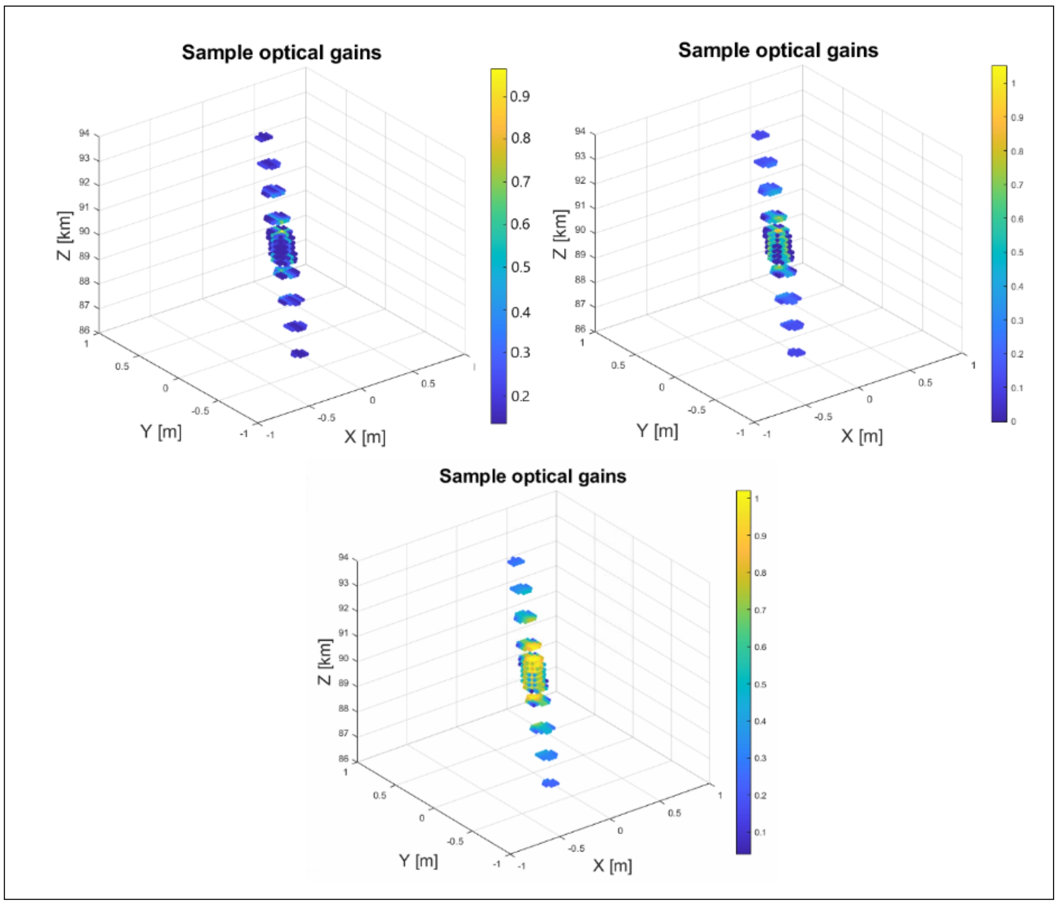

Figure 4.1: Normalized sample optical gains for KL modes 5 (top left), 50 (top right) and 250 (bottom)

From figure 4.1 it is possible to observe that for low KL modes (i.e. low spatial frequencies) the signal is coming mainly from the central point of the LGS, were the pyramid and telescope are focused. As the overall optical gain is obtained as the arithmetic mean of all the sample optical gains, it means that its value will tend to increase with the KL mode (due to modulation effects for the NGS, the optical gain will be decrease at the beginning). As we move radially out from the center, the drop in optical gain (or signal strength) can be explained as when the sample reaches the pyramid, due to its tip and tilt, instead of seeing a four sided pyramid, it will see a glass plane, which does not act as a knife edge, therefore producing less or even no signal.

As the KL mode increases, it is possible to observe that the samples that are not in the center of the LGS start to have more influence in the signal. This can be understood as the KL mode increases the spot size is bigger for every sample, which means that the light will fall in more than one face, increasing the signal strength.

4.1.2 Optical transfer function

After obtaining the calibration matrix for the NGS and both calibration matrices for the LGS' for the first 400 KL modes (all matrices were full rank, meaning they could be left invertible), it was possible to obtain the matrix corresponding to the modal optical transfer function using equation 1.47. Figure 4.2 shows an image corresponding to the matrix representation of the optical transfer function (OTF) for the Gaussian profile LGS. Diagonal terms corresponds to the optical gains and non-diagonals to the coupling between the modes

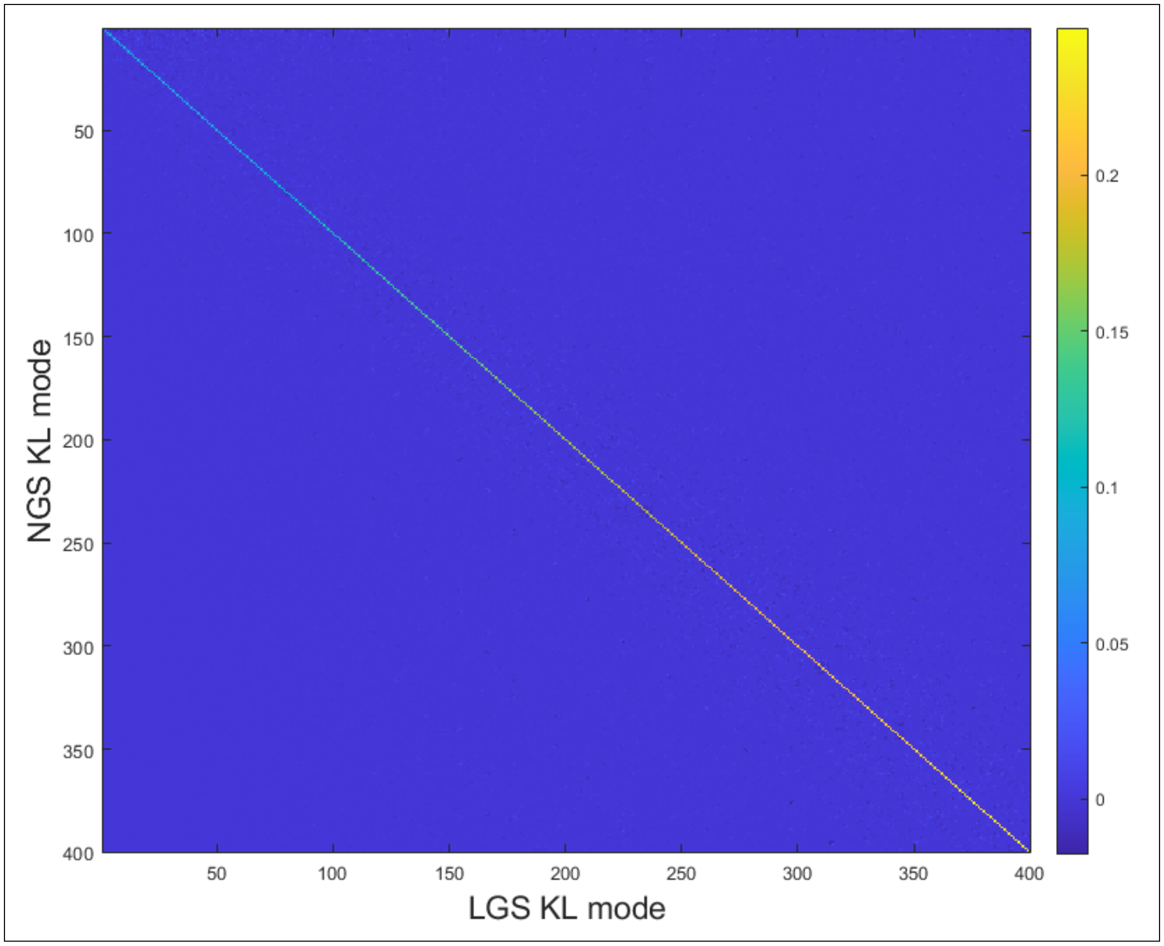

Figure 4.2: Image representation of the matrix corresponding to the optical transfer function.

As it can be seen in figure 4.2, the matrix is mainly diagonal. This can be understood as that the signal obtained using a LGS is similar to that obtained with a NGS, meaning that it would be possible to use the interaction matrix calibrated with a point source to reconstruct a wavefront obtained using a LGS.

To quantify how diagonal the matrix is, an error bar plot was used. The diagonal terms were used as the measurements, meanwhile for each column of the OTF, the RMS value of all the non-diagonal terms was calculated and stored as the error bar.

For a given mode, a high value of the error-bar would mean that the signal coming from the PWFS using a LGS is different from the one using a NGS, therefore the reconstruction can introduce errors. If the error-bar value is low, it means that the reconstruction can be accomplished without introducing errors to the measurement. Figure 4.3 shows the error bar plot corresponding to this description for the Gaussian and the double peak example profile LGS'.

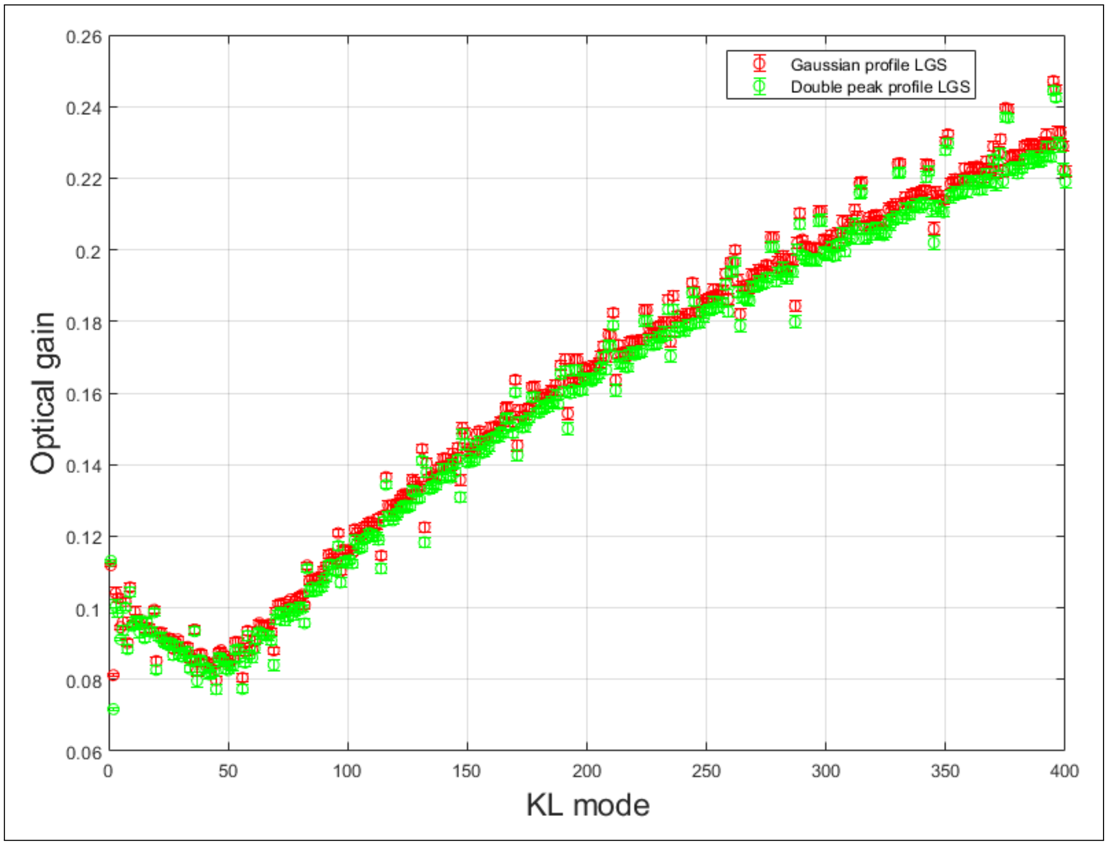

Figure 4.3: Optical gains and coupling between the modes for the Gaussian and double peak profile LGS.

As information about this test could not be found in literature, a factor of 5% coupling (error bar divided by measurement) is considered as a badly reconstructed mode. Figure 4.4 shows the measured coupling between the modes

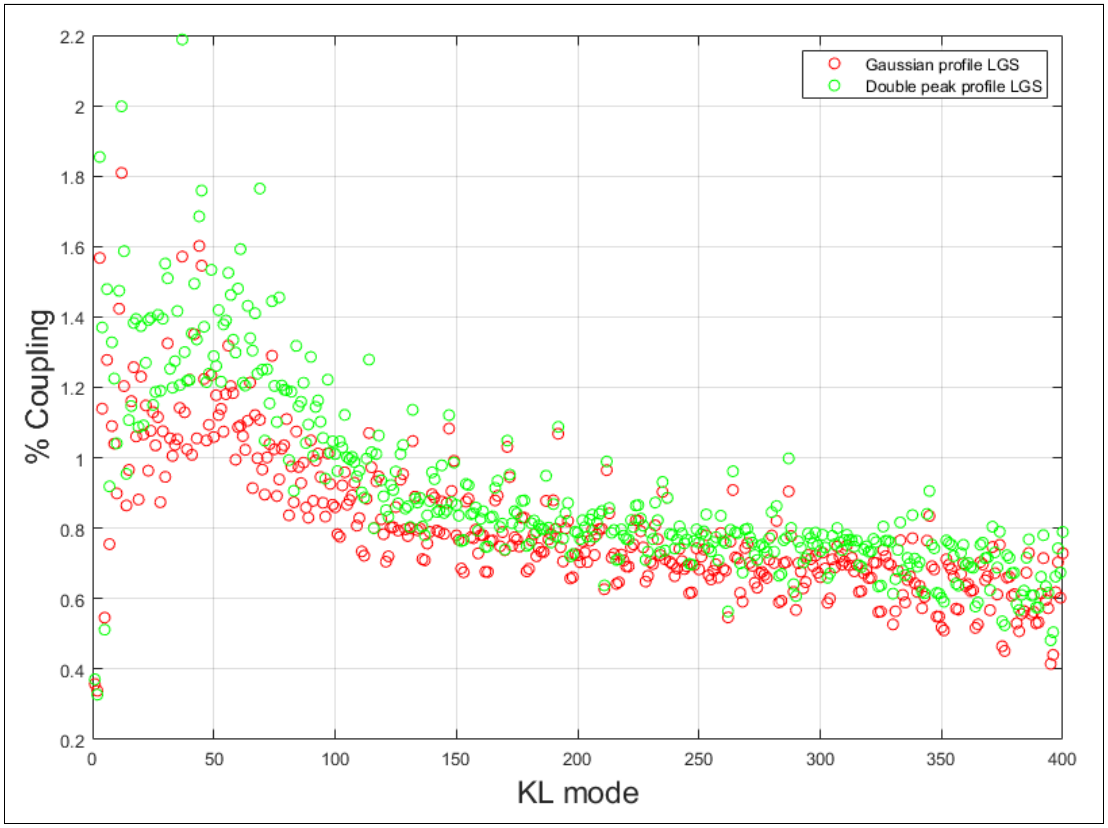

Figure 4.4: Coupling between the modes for the Gaussian and double peak example profile LGS.

As it is possible to observe in figure 4.4, the coupling between the modes does not go above 5% for either profile, therefore it can be concluded that the modes are correctly reconstructed. From the image it is also possible to observe that the coupling between the modes increases if a double peak profile is used. This could be explained as the structure of the LGS can interfere in the reconstruction, adding extra information that has to do more with the shape of the source than with the phase. For example, with the double peak LGS, the centroid of light is not in the focus of the telescope, meaning that the overall measurement will have more focus coefficient than with the Gaussian centered at 90 km.

Another interesting result is to observe what happens when the interaction matrix is calibrated for a Gaussian profile, but the LGS has a different structure, for example a double peak. This can be seen using the same technique as before, i.e.

$$OTF_{gauss \rightarrow double\ peak} = \mathbf{IMat}^{\dagger}_{LGS_{gauss}} \cdot \mathbf{IMat}_{LGS_{double\ peak}} \tag{4.1}$$

The resulting optical transfer function can be seen in figure 4.5

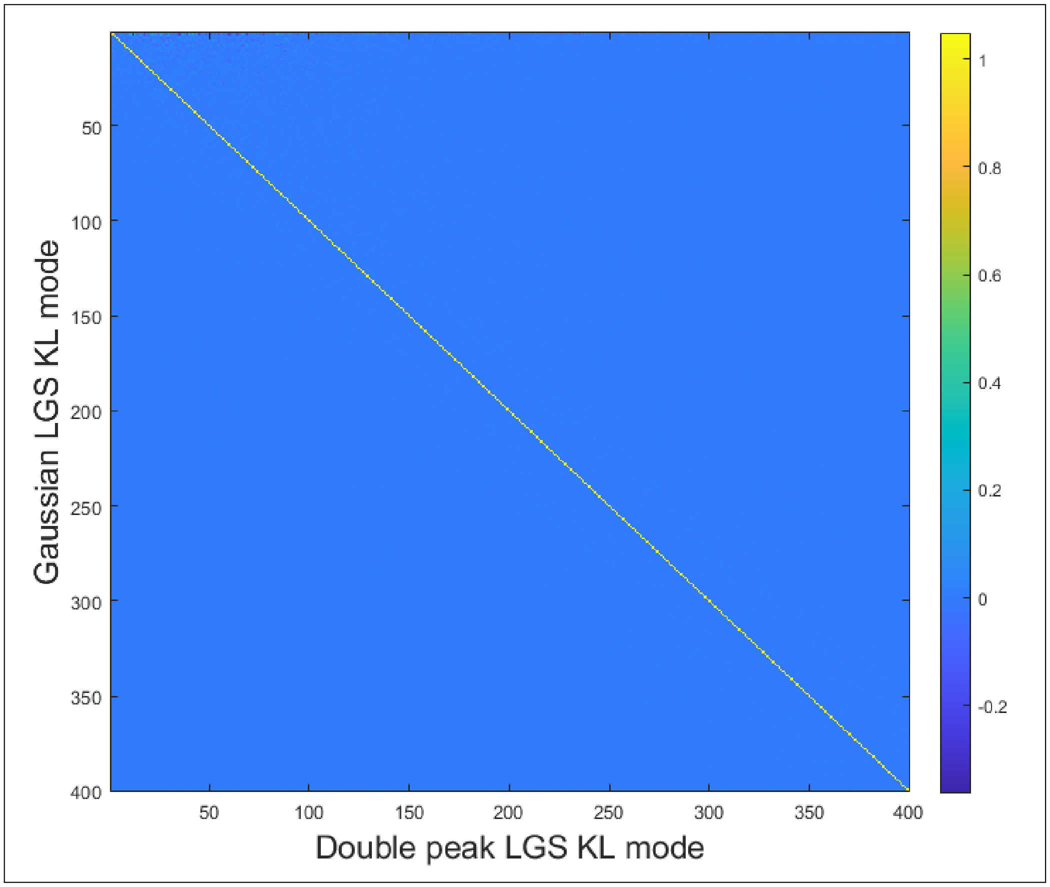

Figure 4.5: Optical transfer function going from a Gaussian sodium profile to a double peak

The OTF is nearly identical to the identity, which means that the signal coming from the two profiles is similar. Figure 4.6 shows the optical gains corresponding to the diagonal of the OTF and figure 4.7 shows the coupling between the modes.

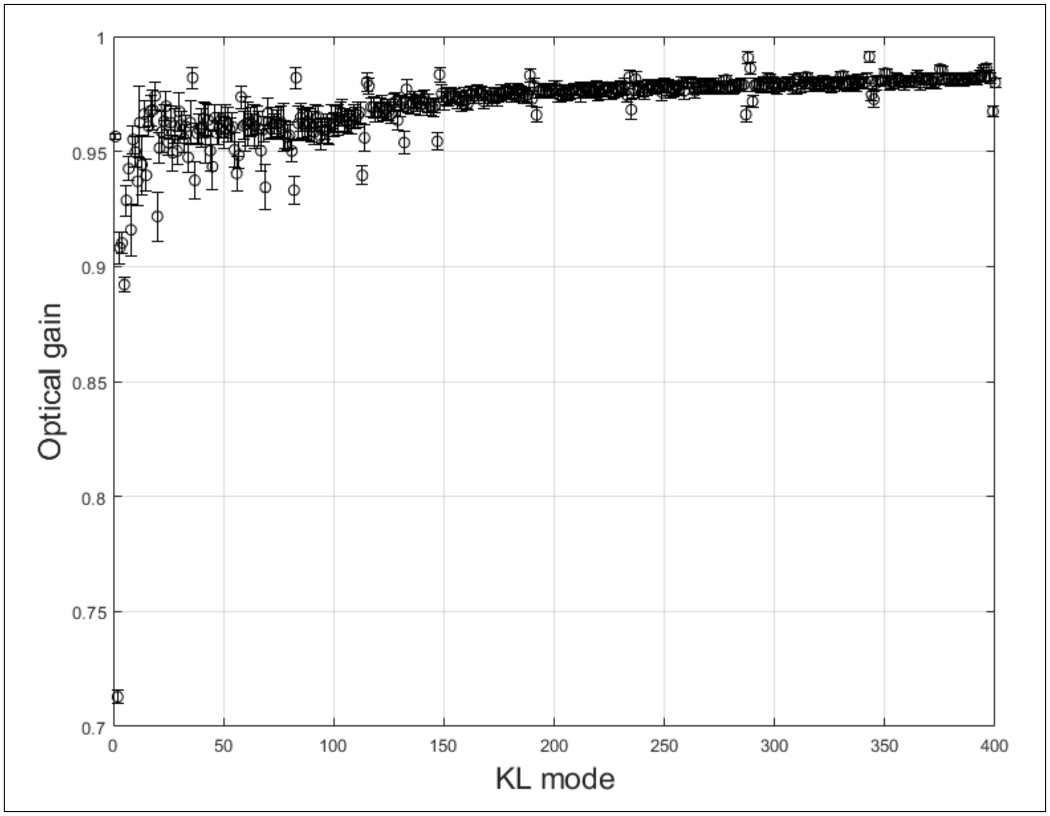

Figure 4.6: Optical gains going from a Gaussian sodium profile to a double peak

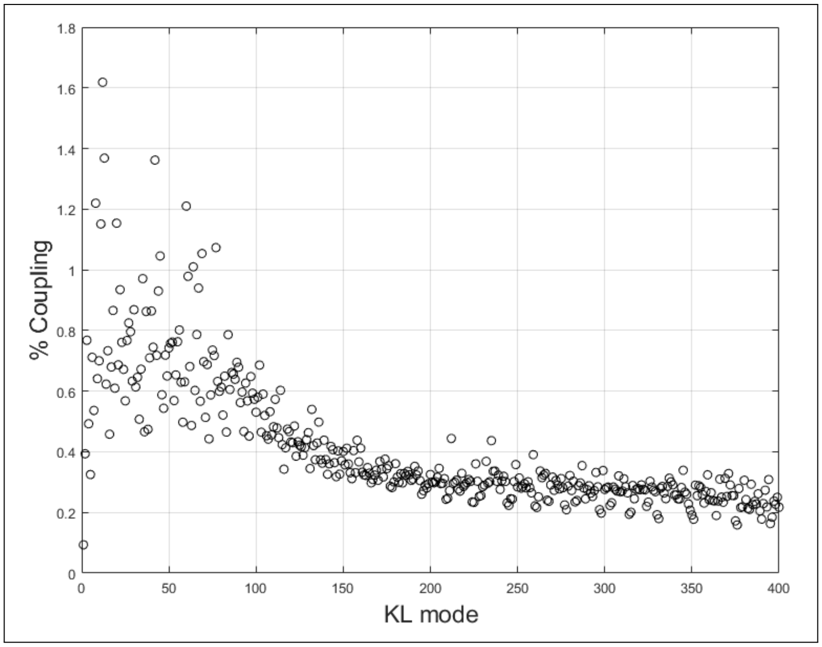

Figure 4.7: Coupling of the optical gains going from a Gaussian sodium profile to a double peak

Considering what was mentioned above, it seems possible to build the interaction matrix using a telescope simulator and a point source like a fiber optics core or a pinhole, and not having to build an elongated object simulator. Then, using theoretical or experimental optical gains, the interaction matrix can be scaled to have the best performance when using a LGS. Also, it seems possible to update the optical gains in real time to optimize the reconstructor for the changing distribution of sodium atoms in the atmosphere.

To test the possibility to reconstruct the LGS wavefront measurement using a point source calibration, new interaction matrices for the LGS were be computed. These IMat's were obtained by updating the optical gains of the point source IMat. To update the optical gain, each column of the $\mathbf{IMat}_{NGS}$ has to be divided by the respective optical gain

$$OG = diag(\mathbf{IMat}^{\dagger}_{LGS}\mathbf{IMat}_{NGS}) \tag{4.2}$$

$$\mathbf{IMat}_{LGS_{new}} = \mathbf{IMat}_{NGS}./OG \tag{4.3}$$

with the diag($\mathbf{A}$) the diagonal of the matrix $\mathbf{A}$ and the $./$ symbol the column-term division.

With this, new interaction matrices were build for the two LGS profiles and tested for linearity, dynamic range and closed loop operation. For nomenclature purposes, **PSC** refers to *point source calibration with updated optical gains* and **ESC** refers to *elongated source calibration*.

4.2 Linearity and dynamic range for point and elongated sources

When a single KL mode is introduced as the wavefront distortion, the sensor outputs an amplitude value for every corrected mode. If it was perfectly linear, then only the mode corresponding to the input would give a measurement and all of the rest would measure zero. In reality, the sensor gives non-zero values for the other modes, corresponding to non-linearities. Figure 4.8 shows the modal decomposition of the signal from the pyramid using NGS for three amplitudes of a single KL mode as input

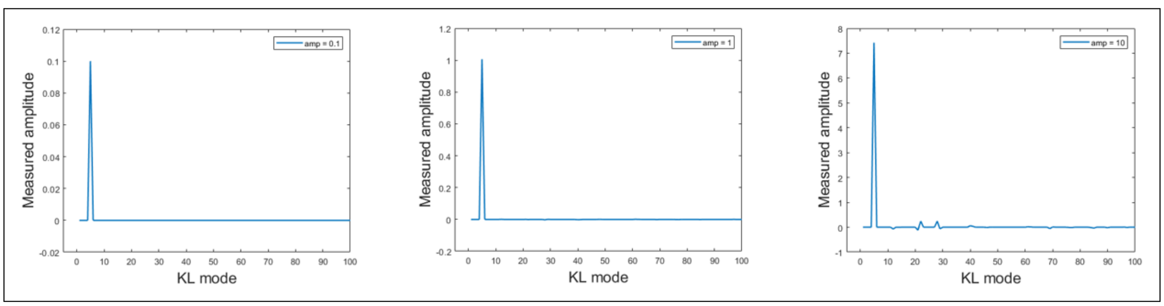

Figure 4.8: Evolution of the measurements for PWFS with NGS as the relative amplitude of the input mode increases from 0.1 on the left up to 10 on the right.

It is possible to observe in figure 4.8 that as the amplitude of the distortion gets larger, the response of the pyramid for that mode decreases and also other modes start to increase the measured amplitude. The difference between the input amplitude and the measured amplitude will be called **residual in the measurement** and the RMS of the non-diagonal modes the **Error introduced in the measurement**

To test linearity, the fitting error was computed. Using an 8.2 meter telescope, 400 KL modes corrected and $r_0 = 0.25\,m$, the fitting error can be estimated using expression 1.40, resulting in

$$\sigma_{fitting} = 63\,nm$$

With this, it is possible to determine that the sensor will be operating in the linear region when the measurement errors do not exceed 63 nm rms (or equivalently 0.67 rad rms).

As the computing time for each linear range estimation is too high, it will be tested for only some of the KL modes. Results can be observed in figures 4.9 to 4.15.

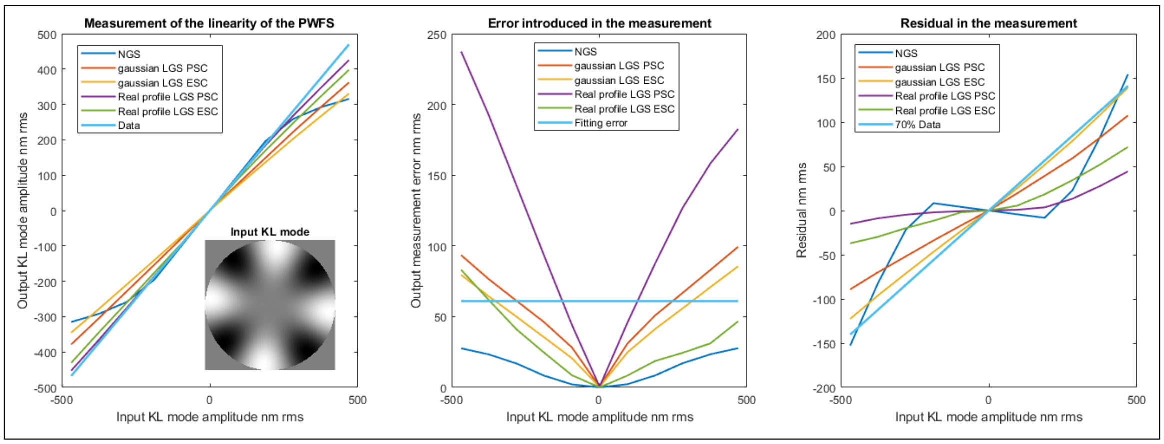

Figure 4.9: Linearity and dynamic range test for KL mode 10. Real profile refers to the double peak example.

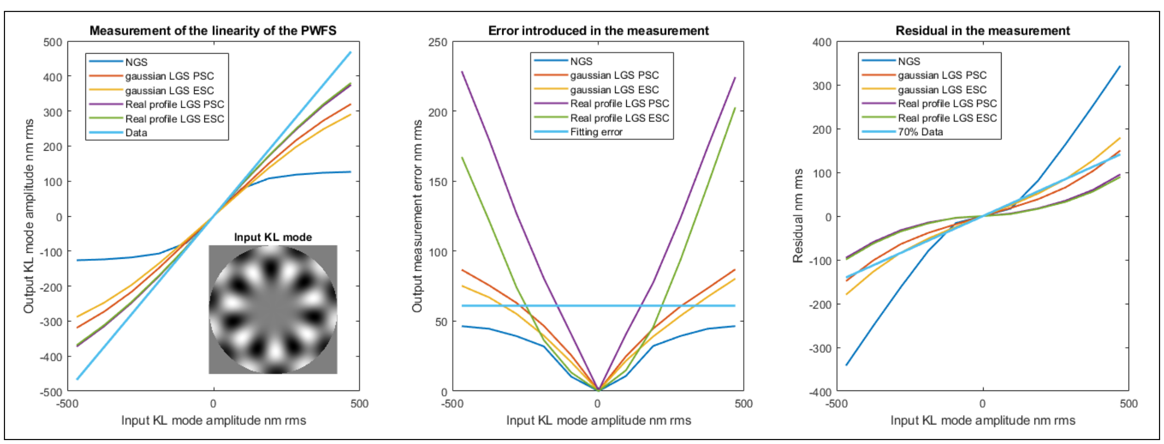

Figure 4.10: Linearity and dynamic range test for KL mode 50.

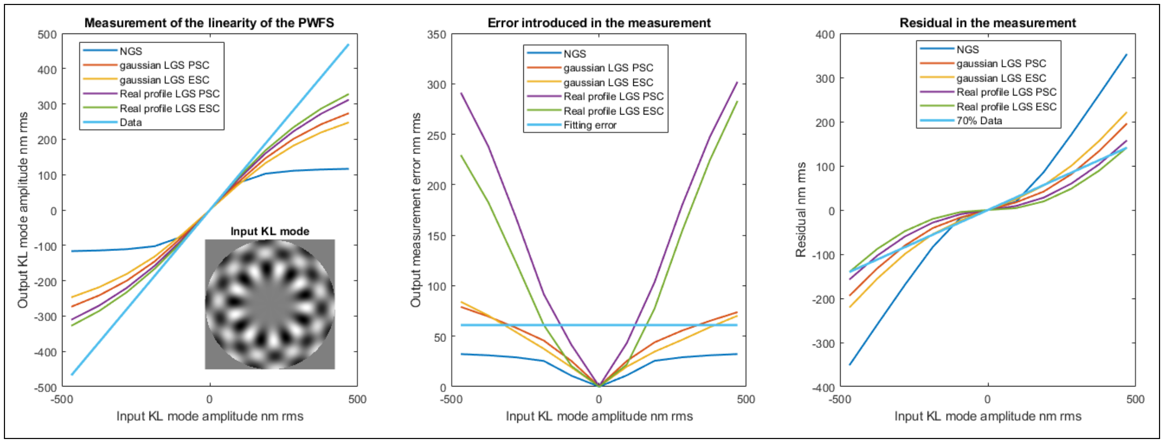

Figure 4.11: Linearity and dynamic range test for KL mode 100.

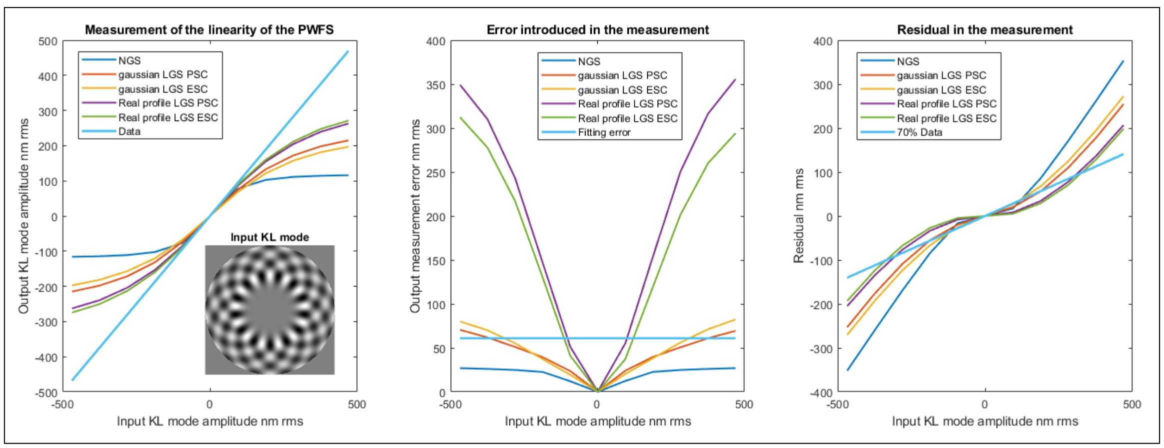

Figure 4.12: Linearity and dynamic range test for KL mode 200.

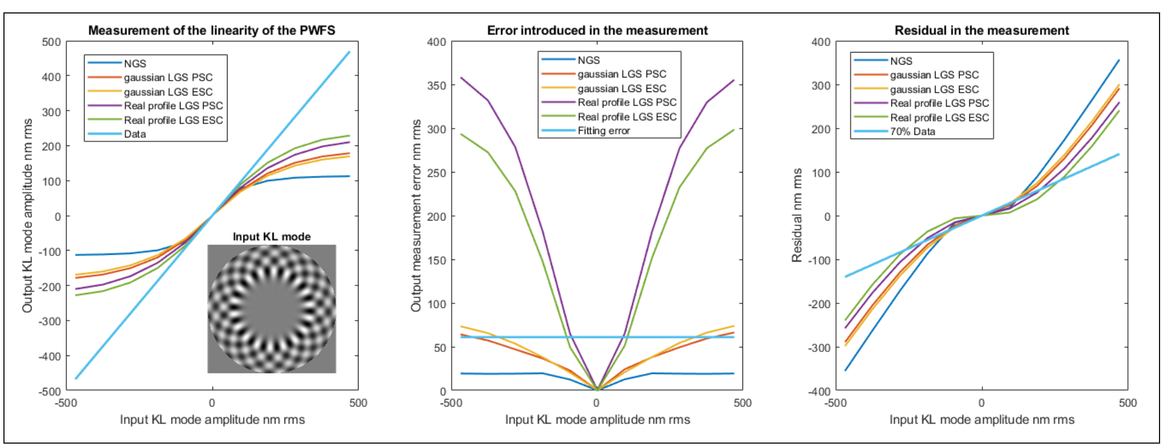

Figure 4.13: Linearity and dynamic range test for KL mode 300.

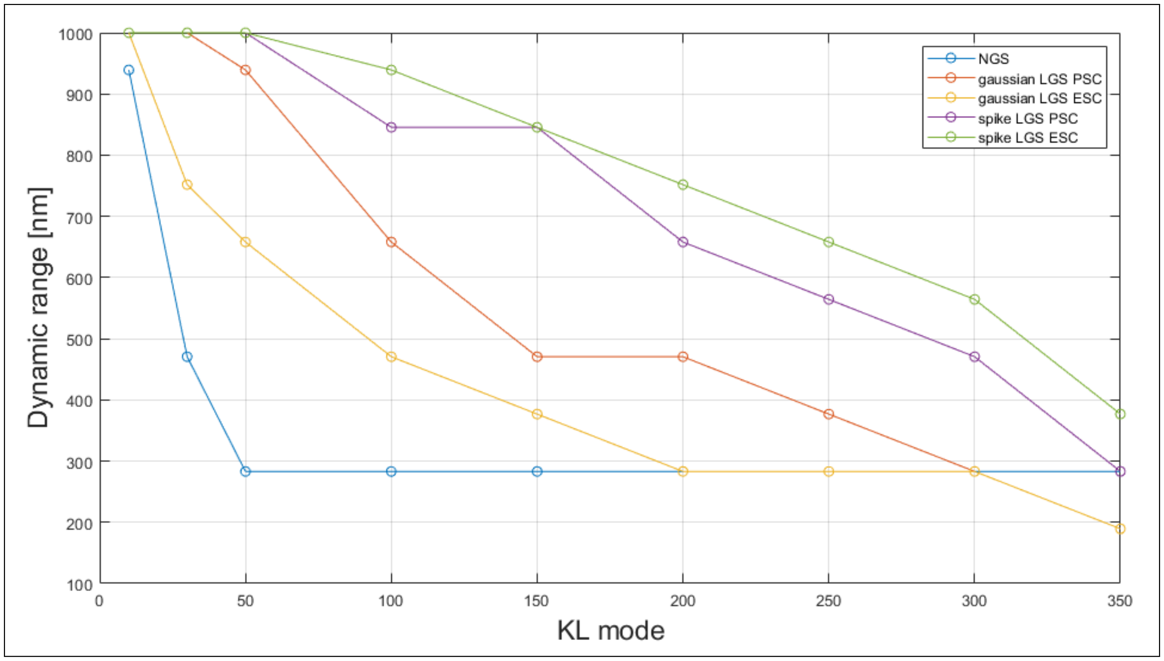

Figure 4.14: Dynamic range measurements for the NGS and the two reconstructors for both LGS'. Measurements are limited to 1000 nm due to simulation constraints. Spike refers to the double peak profile example

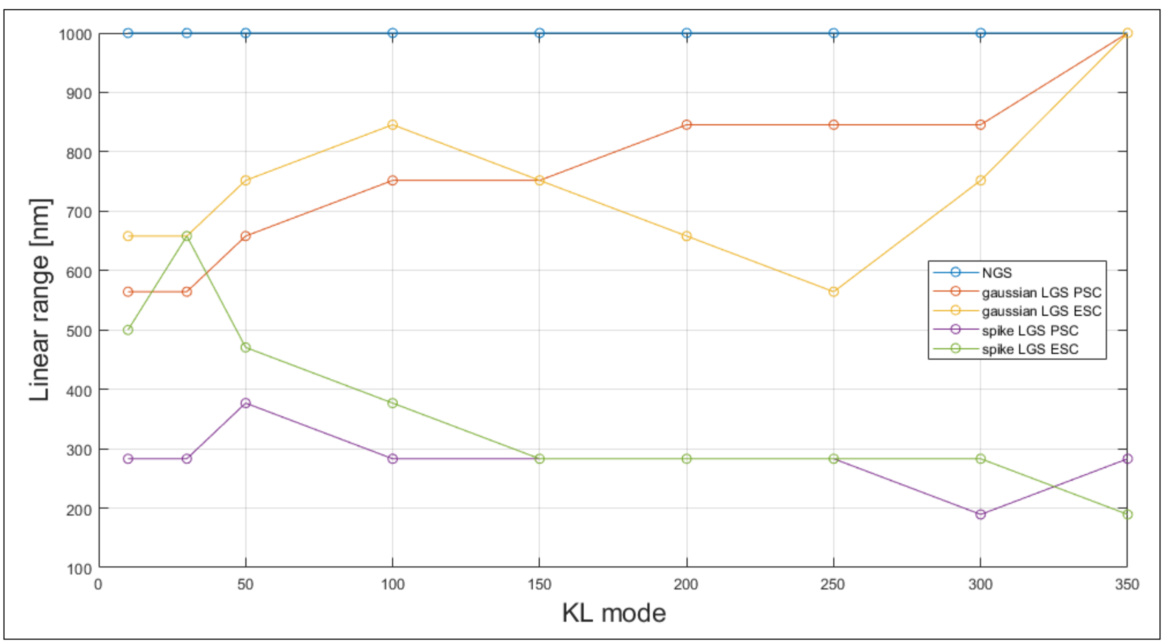

Figure 4.15: Linear range measurements for the NGS and the two reconstructors for both LGS'. Measurements are limited to 1000 nm due to simulation constraints.

From figure 4.14 it is possible to observe the dynamic range of the pyramid tends to decrease for the LGS and remain constant for the NGS (after KL mode 50) as the KL mode increases for all of the simulated cases. This behaviour is expected due to the trade-off between sensitivity and dynamic range and will be explained in section 4.3.2. The size of the LGS acts as a kind of spatial modulation, which increases the dynamic range of the sensor. This effect is visible in the simulation, as the NGS saturates before and to a lower value than the LGS (left graph in figures 4.9 to 4.13).

As the order of the KL mode increases, the dynamic range for the LGS starts getting closer the NGS, because the equivalent modulation amplitude (normalized by the wavelength) becomes similar to the spatial frequencies introduced by the mode (recall figure 1.15).

For all the tested KL modes, the real example profile LGS had the biggest dynamic range. This can be explained as because it had more samples that were not in focus, the spot size of the whole LGS was bigger, therefore it had a bigger equivalent modulation amplitude, increasing the dynamic range.

For the linearity, the NGS does not introduce measurement errors grater than the fitting error, meaning that it always operates in the linear regime. For the LGS, the two profiles have different behaviours, with the Gaussian LGS having in average a linear region two to three times bigger than for the real example profile. This can be explained as the sensor might have been saturated due to the high focus coefficient of the real example profile LGS, therefore interfering with its measurements.

As the structure of the sodium layer is dynamic, it means that the conditions of operation for the LGS are constantly changing. For this reason, a static approach to the control operation is not recommended. Instead, the loop gain, leak factor and if possible the optical gains should be updated in real time to optimize the operation.

4.3 Sensitivity losses

4.3.1 LGS sensitivity maps

As the propagation has to be incoherent for every sample of the LGS, it was possible to observe the sensitivity for each sample independently. For this, the same toy model of the LGS was used, to see how the sensitivity evolves with it's structure. Figure 4.16 shows tree examples for different KL modes.

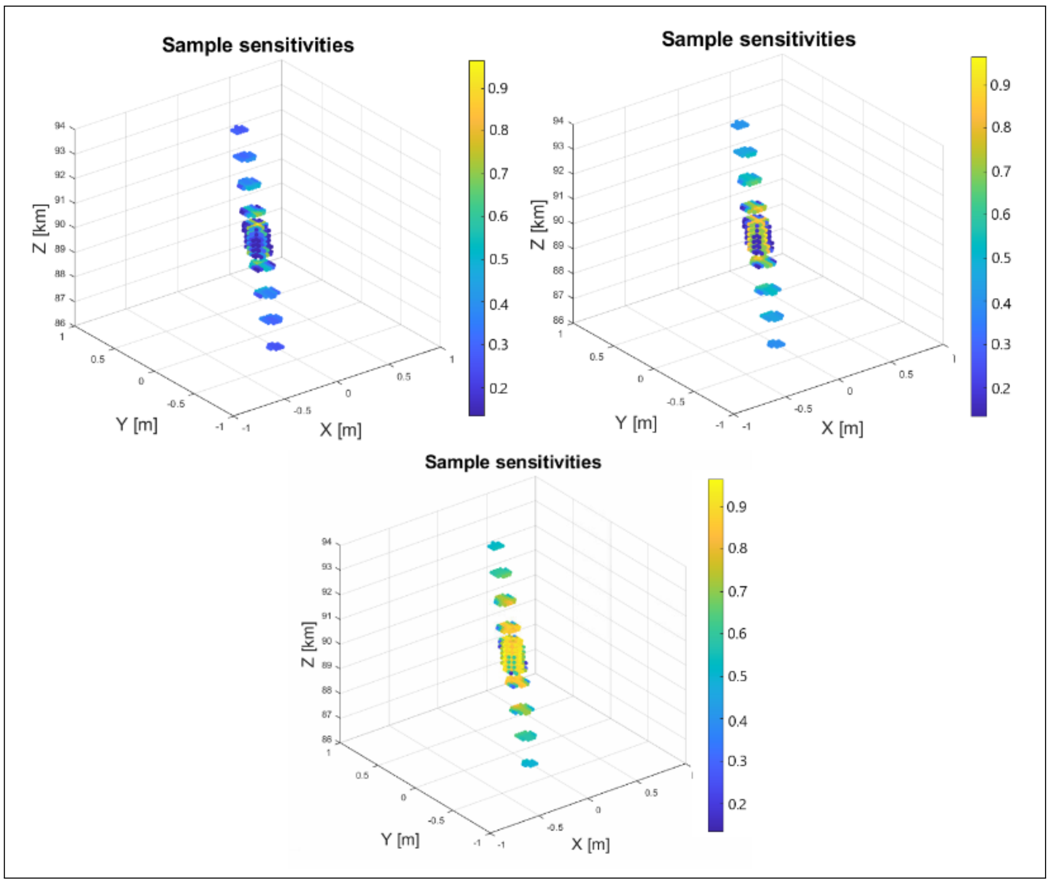

Figure 4.16: Normalized sample sensitivity for KL modes 5 (top left), 50 (top right) and 250 (bottom). The normalization is such that the central point has sensitivity equals to one, with the purpose of compearing the drop in sensitivity for the samples of the LGS compared to a NGS

From figure 4.16 it's possible to observe that for low order KL modes (i.e. low spatial frequency), the pyramid is only sensitive for the samples that are in the center of the LGS, and it quickly drops in sensitivity for the points that are away from it. Then, for higher modes, the pyramid starts to increase it's sensitive area.

From the top right graph in figure 4.16 it's clearly visible that the pyramid is more sensitive in the edges (yellow cross shape in the LGS), which is in concordance with literature. Also, it is possible to see that for the points near the central layer (at 90 km), the sensitivity drops quickly as we go further away radially, but for the points in the outer slices (e.g. 88 or 92 km), because of the defocus coefficient, the image of the sample on the pyramid falls in more than one face, increasing the dynamic range for points that would be otherwise saturated, therefore increasing the sensitivity.

As the order of the KL mode increases (bottom graph in figure 4.16), more of the LGS starts being sensitive, which in term increases the overall sensitivity. This is because the size of spot of the samples acts as a modulation, increasing the dynamic range, therefore allowing more samples of the LGS to provide useful information.

4.3.2 Read out noise (RON) sensitivity

Using expression 1.48, it was possible to obtain the RON sensitivity for the NGS and the different telescope diameters for the LGS. Results are in figures 4.17-4.20.

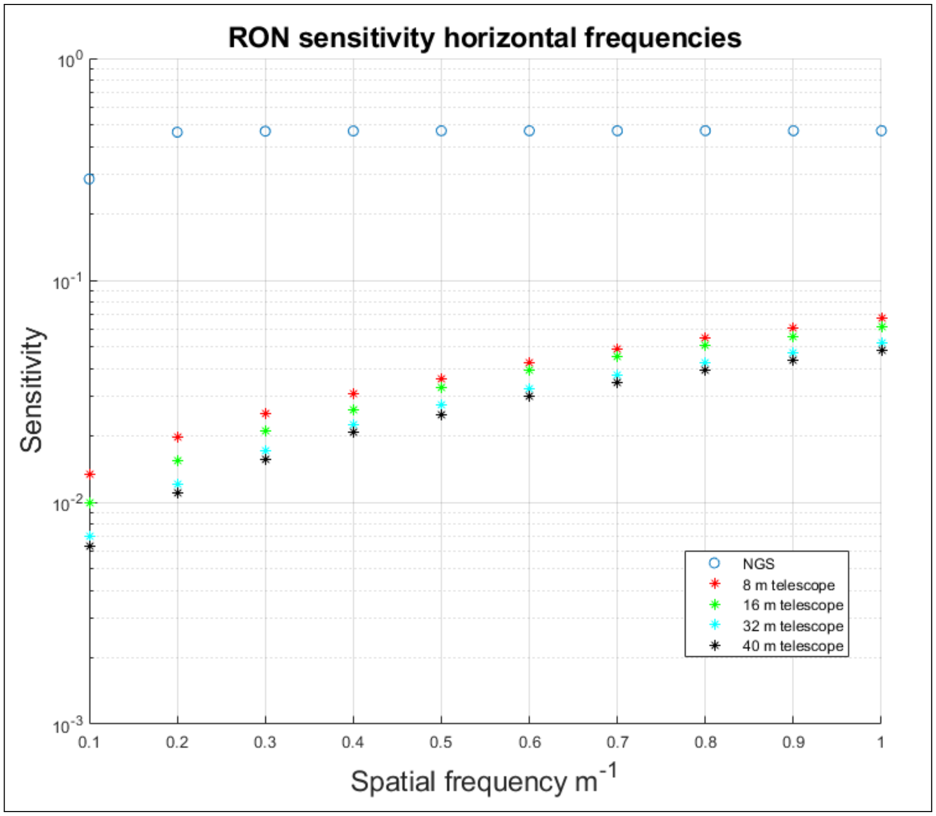

Figure 4.17: Horizontal frequencies RON sensitivity for the NGS and the different telescope diameters for the LGS.

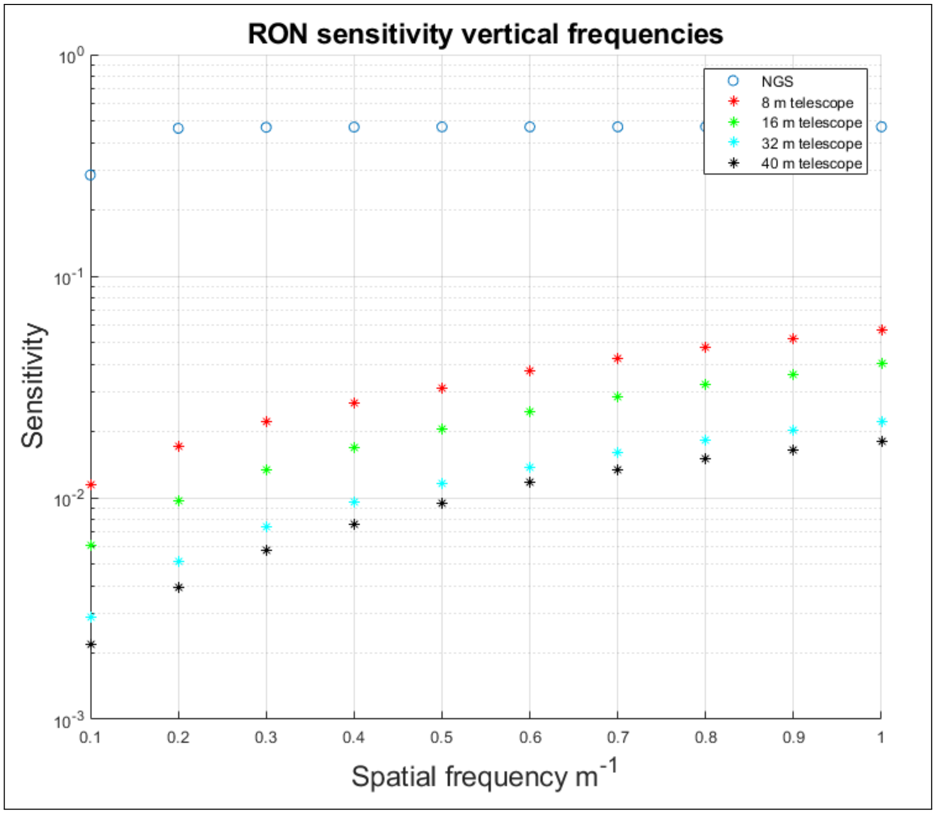

Figure 4.18: Vertical frequencies RON sensitivity for the NGS and the different telescope diameters for the LGS.

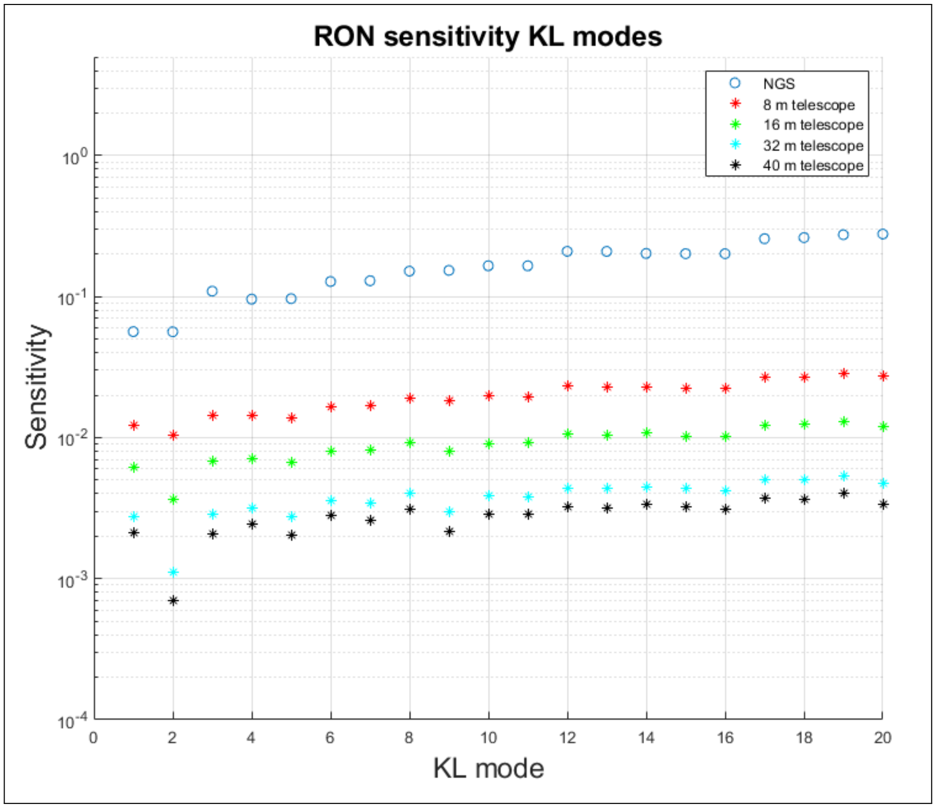

Figure 4.19: first 20 KL modes RON sensitivity for the NGS and the different telescope diameters for the LGS.

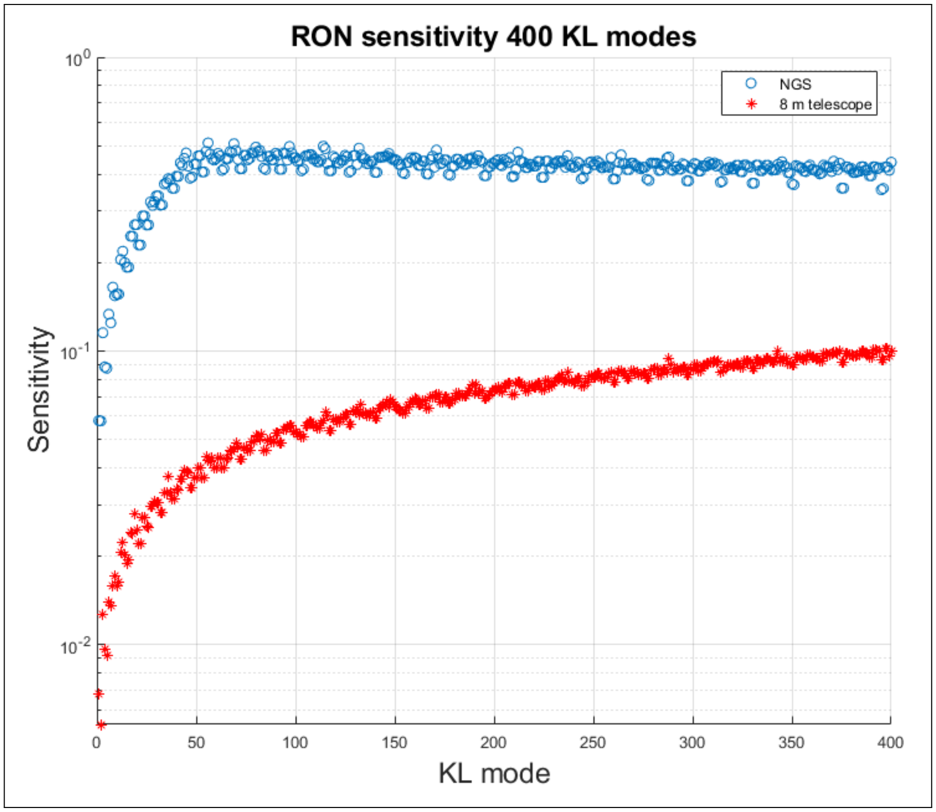

Figure 4.20: first 400 KL modes RON sensitivity for the NGS and 8 m telescope for the LGS.

In figure 4.17 (horizontal frequencies) it is possible to observe that there is a considerable drop in sensitivity going from an NGS to an LGS. This drop is around 95 % for the lower spatial frequencies and 90 % for higher ones. There exists a drop in sensitivity as the telescope diameter increases but is not as large as for the vertical frequencies. This drop in sensitivity for horizontal frequencies may have to do with the reduced depth of field for the bigger telescopes. This increases the horizontal width of the LGS, lowering the sensitivity.

Figure 4.18 shows the impact of the elongation of the LGS on the sensitivity, as the 40 m telescope is five to ten times less sensitive than the 8 m one, and 25 to 200 times less sensitive than the NGS.

In the KL modes, the first two are tilt and tip. Looking at figure 4.19, it is possible to observe that, for the LGS, these have different sensitivities, and as the telescope diameter increases, this difference becomes even greater (Tip and Tilt modes are not corrected by using LGS, but it serves as a form to check if the results make sense). This has to do with the horizontal and vertical natures of these modes, making the Tip mode less and less sensitive than the Tilt mode as the telescope diameter gets larger.

From figure 4.20 it is possible to observe that the sensitivity for the NGS reaches a plateau at approximately KL mode 50 due to the presence of modulation, and that the sensitivity for the LGS seems to remain stable at 0.1, meaning that, at best, the sensitivity is five times lower than for a NGS. This difference in sensitivity can be expressed as an increase in equivalent magnitude using equation 1.45. Assuming the same detector and optical setup, the loss in sensitivity when correcting the first 400 KL modes corresponds to an increase in observing magnitude of 2.3 for an 8 m telescope (e.g. a 12.3 magnitude NGS would produce the same error due to RON as a 10 magnitude LGS).

Then, looking at figures 4.17 - 4.19, the ratio in sensitivity between the different telescope diameters remains approximately constant, therefore its assumed that the 40 m telescope will always have around 7 times less sensitivity than the 8 m telescope. Equation 1.45 has also the number of photons as a parameter. A 40 m telescope will theoretically grab 25 times more photons from the same source than an 8 m one (this will be probably lower due to the central obstruction, but the number is within the order of magnitude). Plugging this into equation 1.45 a loss in equivalent magnitude can be computed. The approximate loss in equivalent magnitude when using an LGS with a 40 m telescope is 0.9, lower than for the 8 m telescope. This result suggest that a 40 m telescope would be less affected by RON.

4.3.3 Photon noise sensitivity

Using expression 1.49, it was possible to obtain the photon noise sensitivity for the NGS and the different telescope diameters for the LGS. Results are in figures 4.21-4.24.

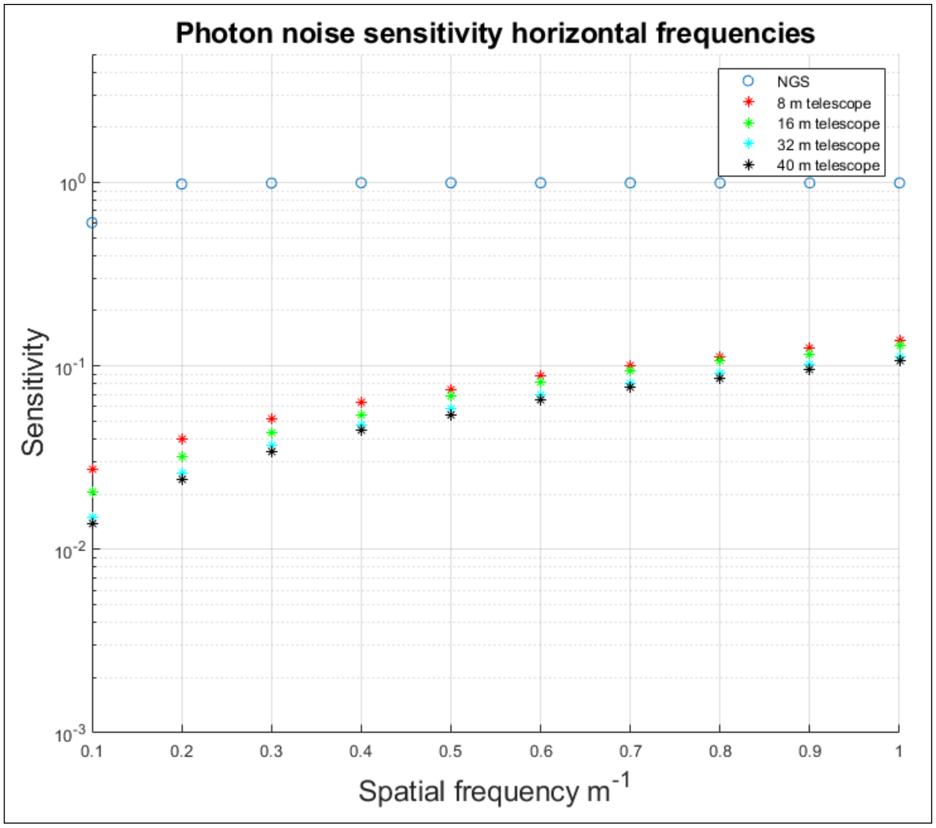

Figure 4.21: Horizontal frequencies photon noise sensitivity for the NGS and the different telescope diameters for the LGS.

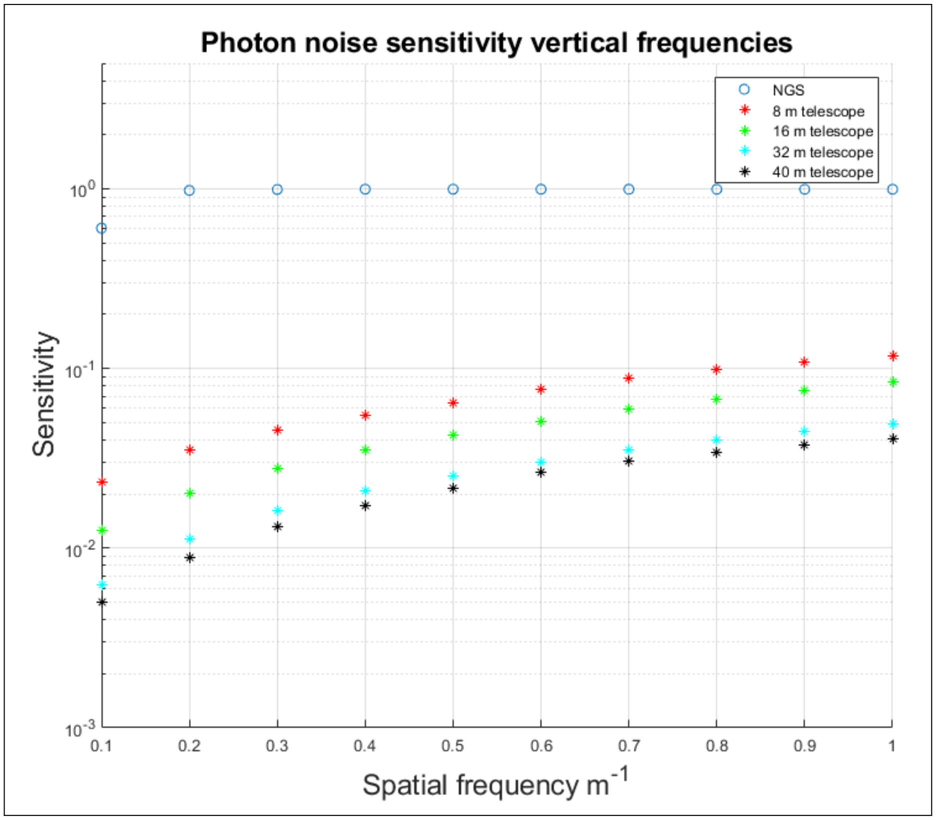

Figure 4.22: Vertical frequencies photon noise sensitivity for the NGS and the different telescope diameters for the LGS.

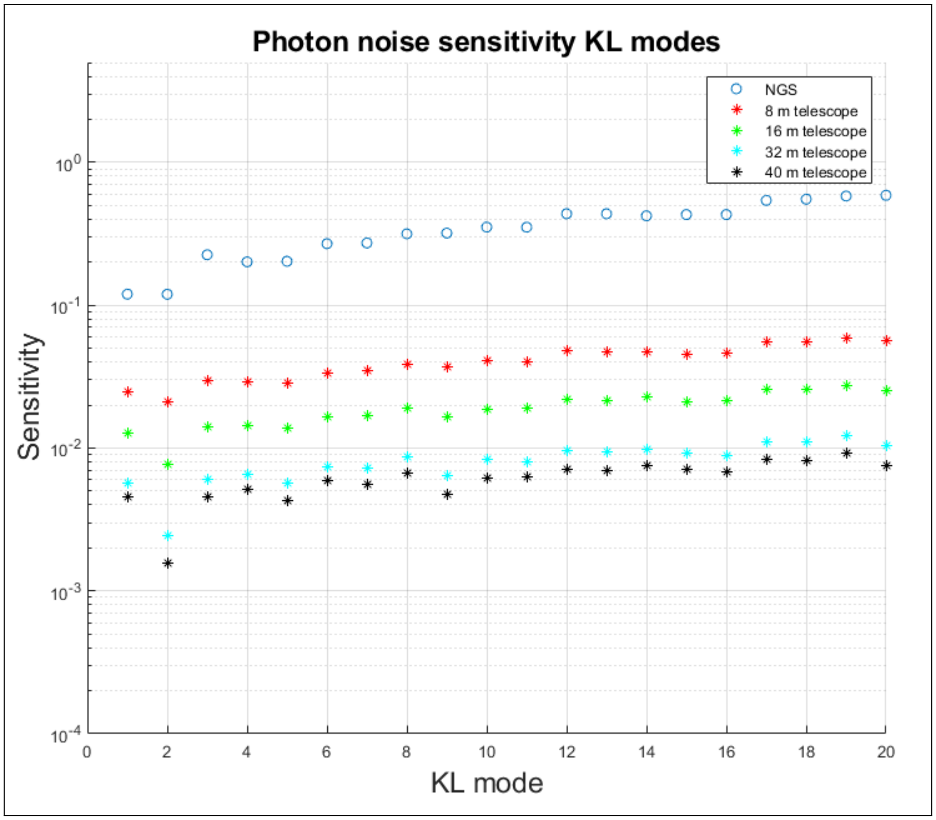

Figure 4.23: first 20 KL modes photon noise sensitivity for the NGS and the different telescope diameters for the LGS.

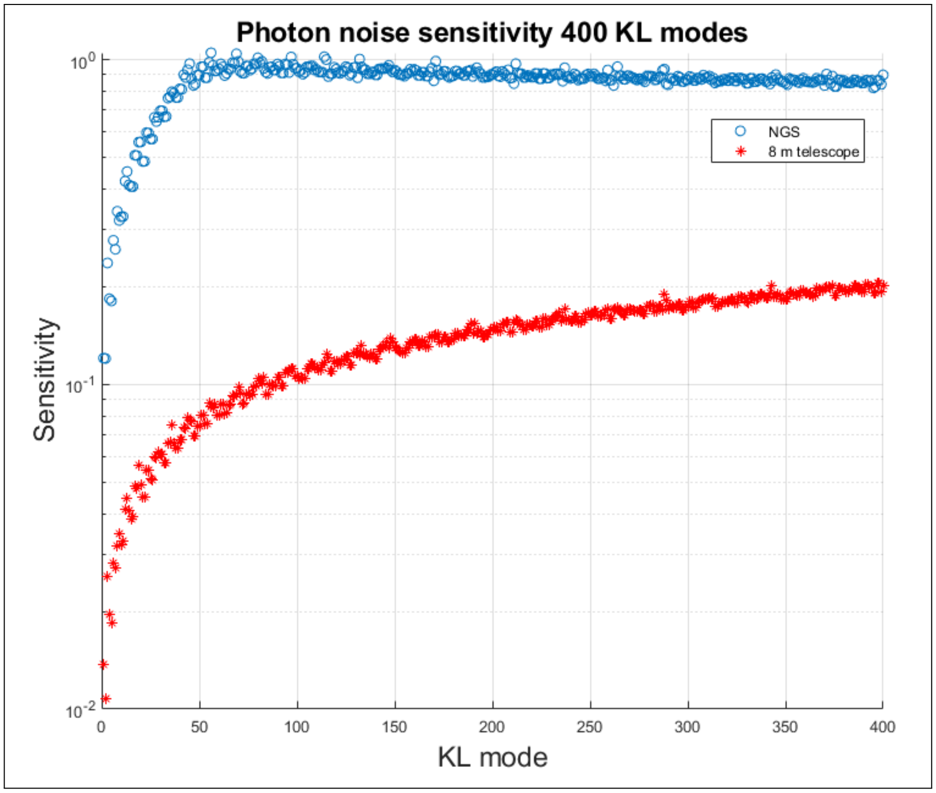

Figure 4.24: first 400 KL modes photon noise sensitivity for the NGS and 8 m telescope for the LGS.

Similar to the RON sensitivity, it is possible to observe in figures 4.21 and 4.22 that there is a 90 to 98 % drop in sensitivity when using LGS in comparison to an NGS for an 8 m telescope, and even higher for a 40 m telescope. Using the results from the 400 KL modes tested and equation 1.45, it is possible to compute that the loss in equivalent magnitude due to photon noise is 4.6 for a 8 m telescope. Using the same logic as before, assuming a constant ratio between the 8 m telescope sensitivity and the 40 m sensitivity, the loss in equivalent magnitude when using a 40 m telescope and an LGS is 5.3 (e.g. a 14.3 magnitude NGS would produce the same error due to photon noise as a 9 magnitude LGS). As photon noise usually is the limiting contribution to the error budget when using LGS, this loss in observing magnitude is a loss in limiting magnitude.

This overall drop in sensitivity has led other scientists to develop new wavefront sensors specially design to deal with the elongation of the LGS (Ragazzoni et al., 2018).

4.4 Closed loop operation

Doing several test varying the control parameters, the best results were obtained with

$$\text{loop gain} = \beta = 0.4$$

$$\text{leak factor} = \alpha = 0.95$$

Using these parameter for all of the configurations, closed loop tests were performed for low and high wind situations. The loop was closed after 20 iterations. Figure 4.25 shows an image of an uncorrected star affected by atmosphere, which was the starting point for all of the closed loop test.

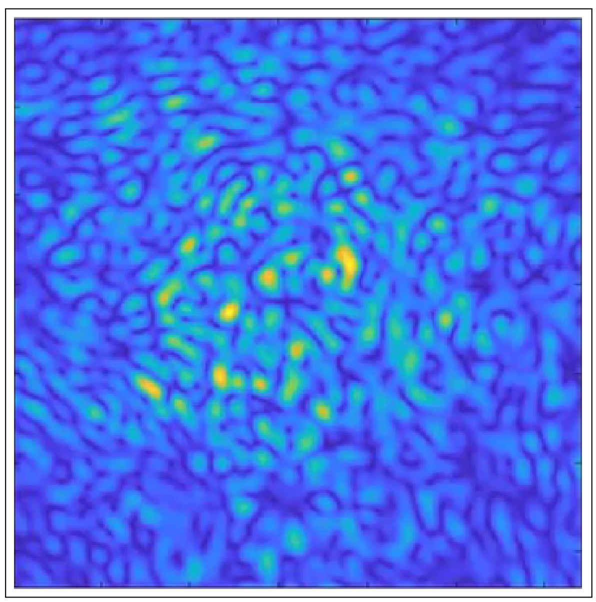

Figure 4.25: Square root scale image of an uncorrected image of a star

4.4.1 Without noise

The parameters used for the closed loop with out noise were

- Telescope diameter: 8 m

- r_0: 0.25 m
- Field of View for the guide star: 10 x 10 arcsec

4.4.1.1 Low wind

For the low wind situation, the weighted wind speed can be obtained using OOMAO. With this, the coherence time for the phase can be computed using expression 1.41.

$$\tau_0 = 10.8\, ms \tag{4.4}$$

As the system runs at 500 Hz, the delay time is 2 ms, therefore the temporal error should not affect as much the residual phase.

Figure 4.26 shows the evolution of the Strehl ratio for low wind conditions. Figures 4.27 and 4.28 show the evolution for the residual phase. Fitting error was included to observe the limiting error on the correction.

For each iteration of the control loop, a "science" star gets propagated through the atmosphere and corrected by the DM. Figure 4.29 shows images of the corrected "science" star for low wind conditions using NGS, Gaussian LGS and real example profile LGS. Point source calibration was used for the three cases and optical gains were updated for the LGS'.

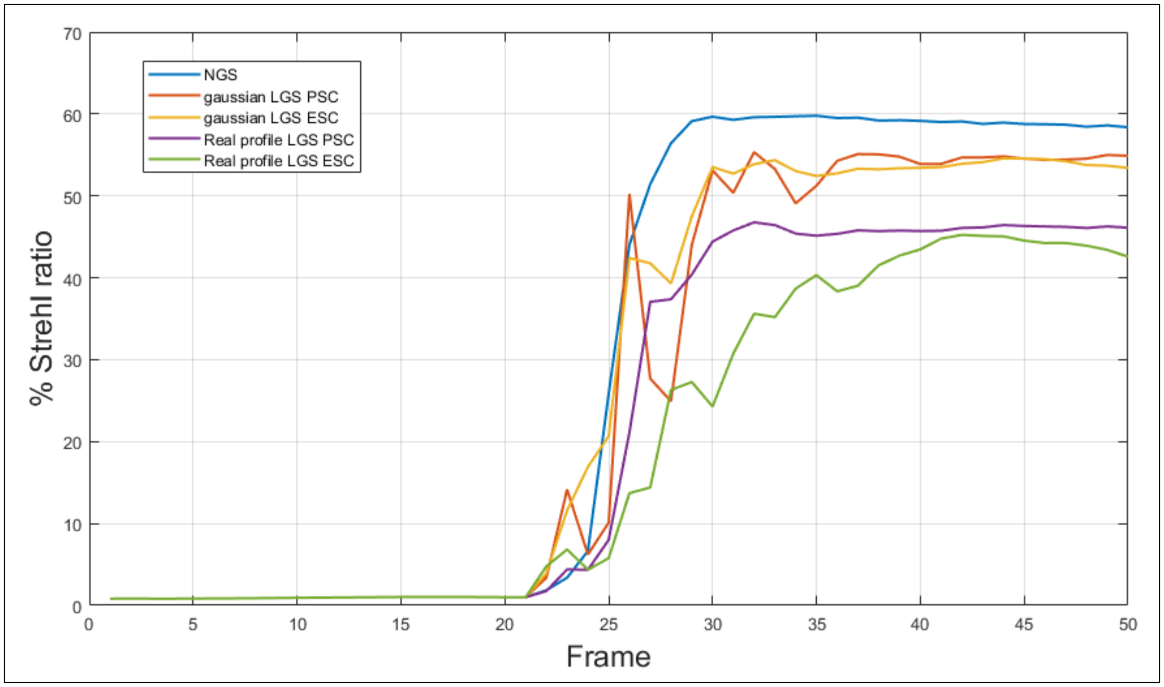

Figure 4.26: Strehl ratio evolution in closed loop for the NGS and the two cases for both LGS for low wind condition. The loop was closed in frame 20.

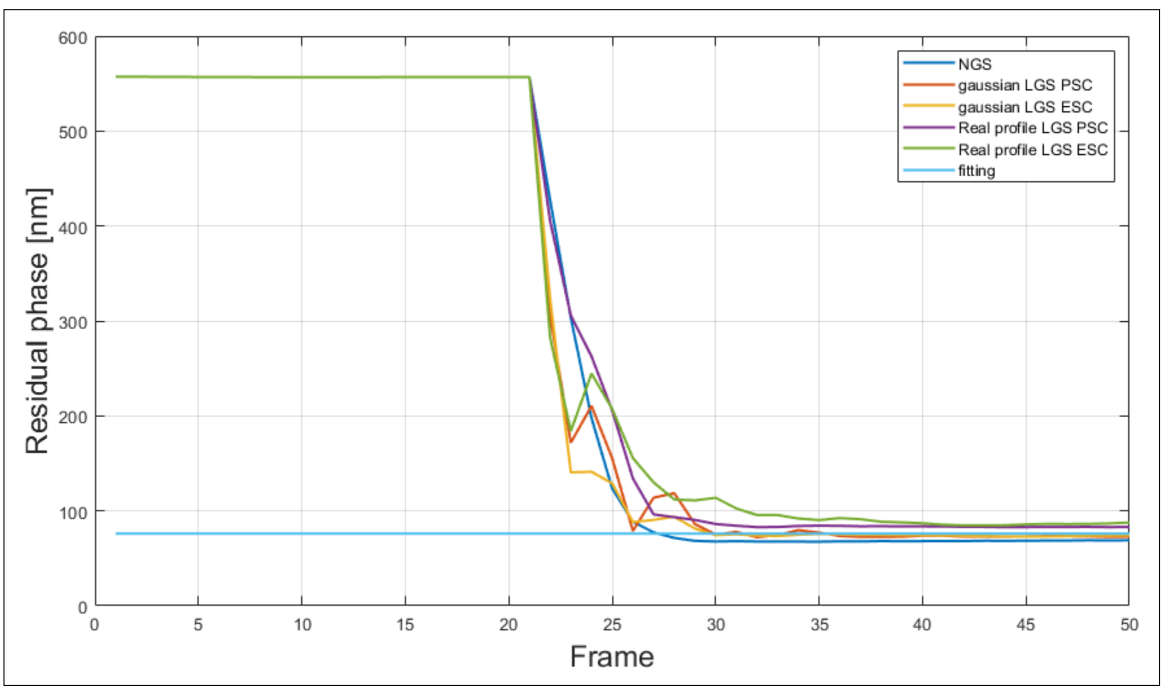

Figure 4.27: Residual phase RMS in closed loop for the NGS and the two cases for both LGS for low wind condition.

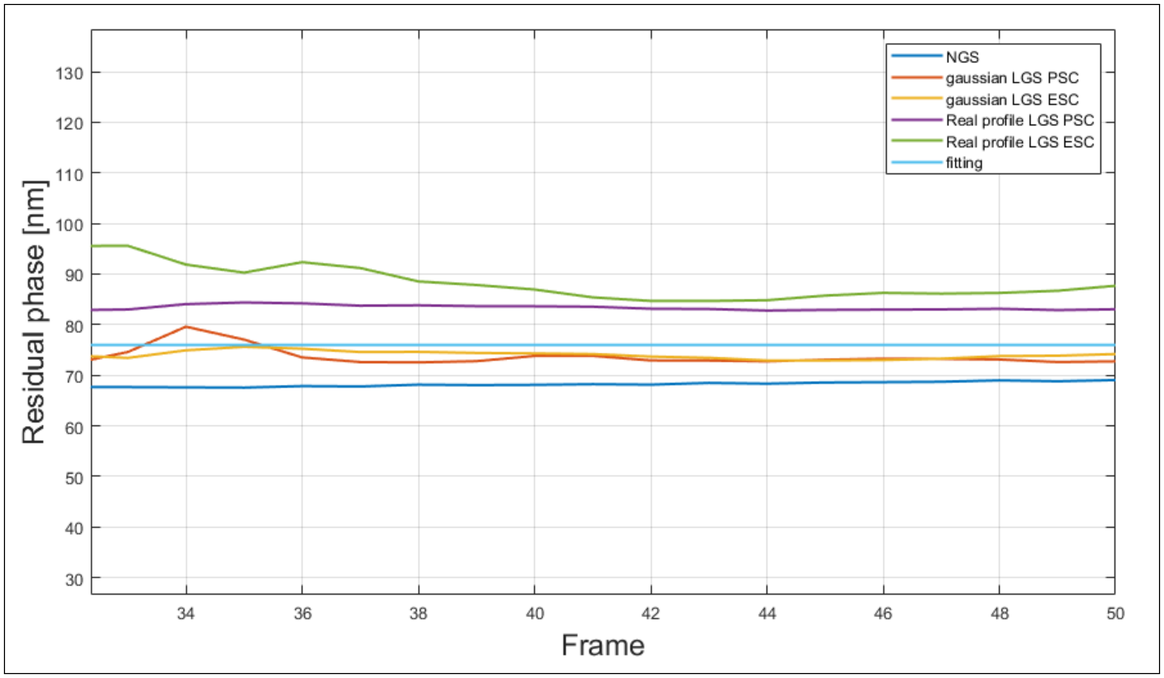

Figure 4.28: Residual phase RMS close up in closed loop for the NGS and the two cases for both LGS for low wind condition.

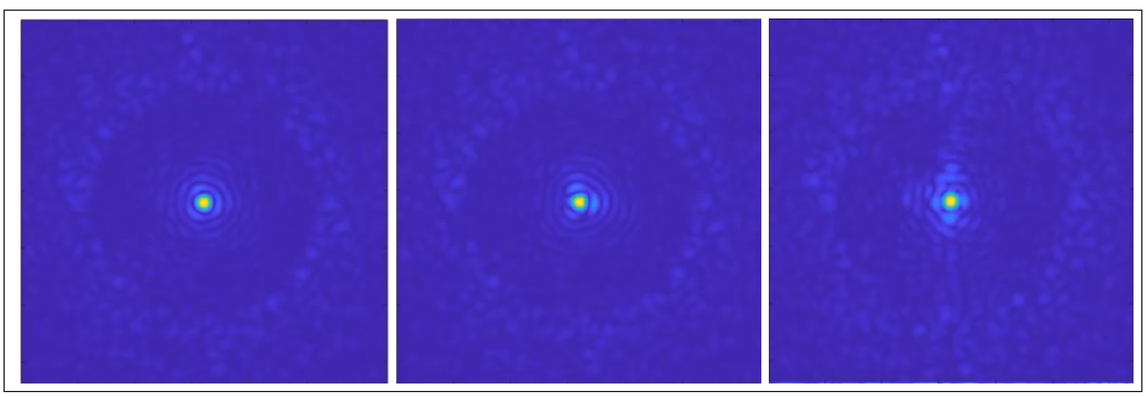

Figure 4.29: Square root scale image of corrected "science" star in low wind condition using point source calibration (and updated optical gains for the LGS'). From left to right the images are for AO systems using NGS, Gaussian LGS and real example profile LGS

From figure 4.26, it is possible to observe that the SR increased from 1% to up to 60 % when using the NGS and between 45-55% for the LGS. The NGS had a better performance than any of the LGS cases. This might be explained as the error introduced in the measurements for the NGS are lower than for the LGS, and when achieving high levels of correction, small errors in phase can have an effect on the SR.

For the LGS', the Gaussian profile LGS had a similar behavior for both calibrations and had a better performance than the real example profile one. This difference might come from the fact that the structure of the real example profile introduces more measurement errors than the Gaussian profile.

The fact that it is possible to close the loop for both LGS' using a complete point source calibration indicates the possibility of using the pyramid for laser guide star wavefront sensing. Even for the real profile the loop showed a good level of correction, meaning that it is possible to update the optical gains to optimize the reconstructor for the profile of the sodium concentration on the atmosphere.

From figures 4.27 and 4.28, it is possible to observe that fitting error is probably what is limiting the correction for the NGS and Gaussian LGS, but for the real profile LGS the non-linearities can also limit its performance.

Figure 4.29 shows the PFS' obtained for the "science" star for the three most important scenarios (Elongated source calibration would be too difficult to obtain in laboratory or telescope conditions) in low wind conditions.

For the AO using NGS (left image in fig. 4.29), Airy disks are clearly visible, meaning that diffraction limit was achieved. Also, it is possible to observe that there is a dark disk surrounding the star. This disk comes from the fact that only 400 KL modes are used for the reconstruction, and the radius of the disk is proportional to the highest spatial frequency that is being corrected.

For the AO using the Gaussian LGS, Airy disks are visible (center image in fig. 4.29), but there is a asymmetrical shape in the correction of the star. This may come from the fact that the reference intensity used came from a point source calibration (left image in figure 3.5), instead of an elongated one (left image in figure 3.10). This difference in reference intensity can introduce mainly tip, tilt and focus, but as those aberrations are large, the sensor can saturate and introduce non-linearities.

For the AO using the real example profile LGS, Airy disks are barely visible (right image in fig. 4.29). The central spot is well defined, but there are speckles in the image that may interfere with, for example, the determination of the presence of a companion. This implies that the structure of the LGS can limit the resolution and contrast of the image.

4.4.1.2 High wind

For the high wind situation, the weighted wind speed can be obtained using OOMAO. With this, the coherence time for the phase can be computed using expression 1.41.

$$\tau_0 = 6\,ms \tag{4.5}$$

The 2 ms delay now might be comparable to the coherence time, therefore the expected residual error can be obtained as the geometric sum of the fitting error and the temporal error

$$\sigma^2_{high-wind} = \sigma^2_{fitting} + \sigma^2_{\tau} \tag{4.6}$$

Using the obtained values from the simulation, the expected residual error is

$$\sigma_{high-wind} = 98\,nm \tag{4.7}$$

Figure 4.30 shows the evolution of the Strehl ratio for high wind conditions. Figures 4.31 and 4.32 show the evolution for the residual phase. Fitting and temporal error were included to observe the limiting error on the correction. Figure 4.33 shows images of the corrected "science" star for high wind conditions using NGS, Gaussian LGS and real example profile LGS. Point source calibration was used for the three cases and optical gains were updated for the LGS'.

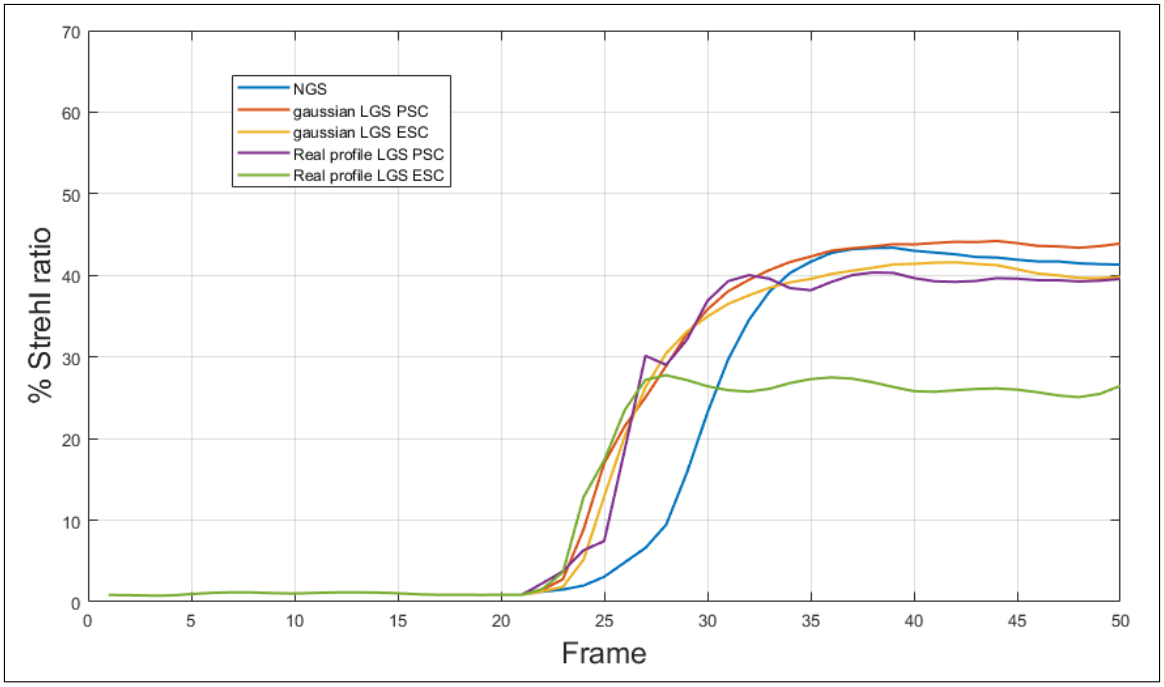

Figure 4.30: Strehl ratio evolution in closed loop for the NGS and the two cases for both LGS for high wind condition. The loop was closed in frame 20

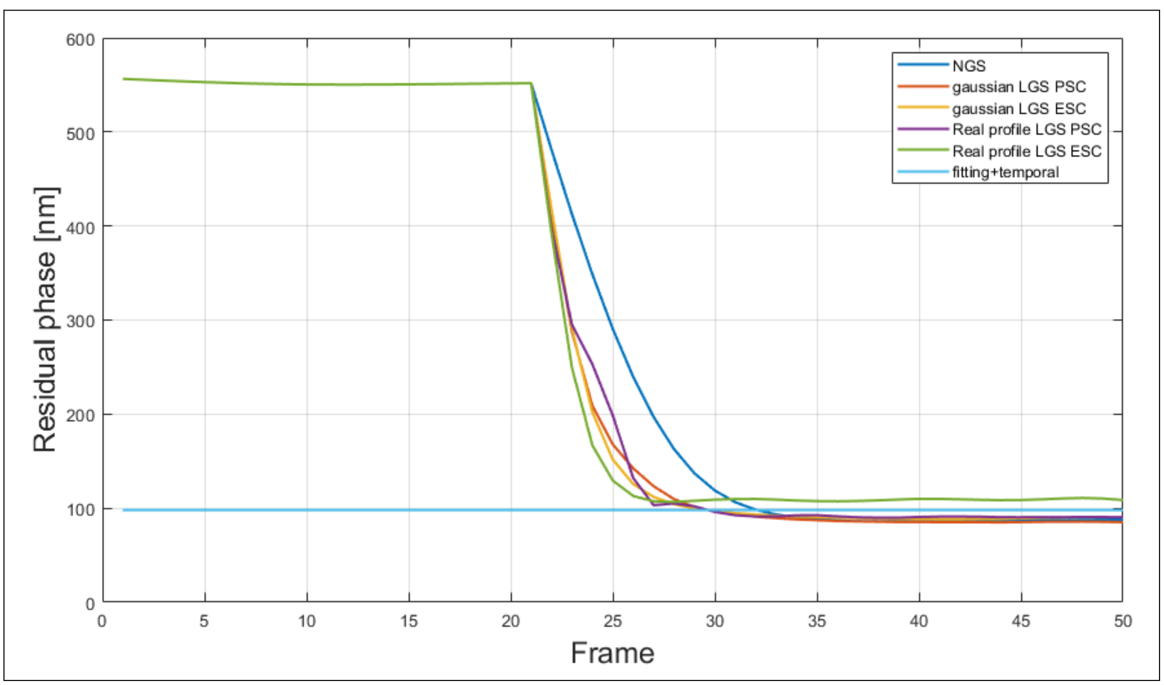

Figure 4.31: Residual phase RMS in closed loop for the NGS and the two cases for both LGS for high wind condition.

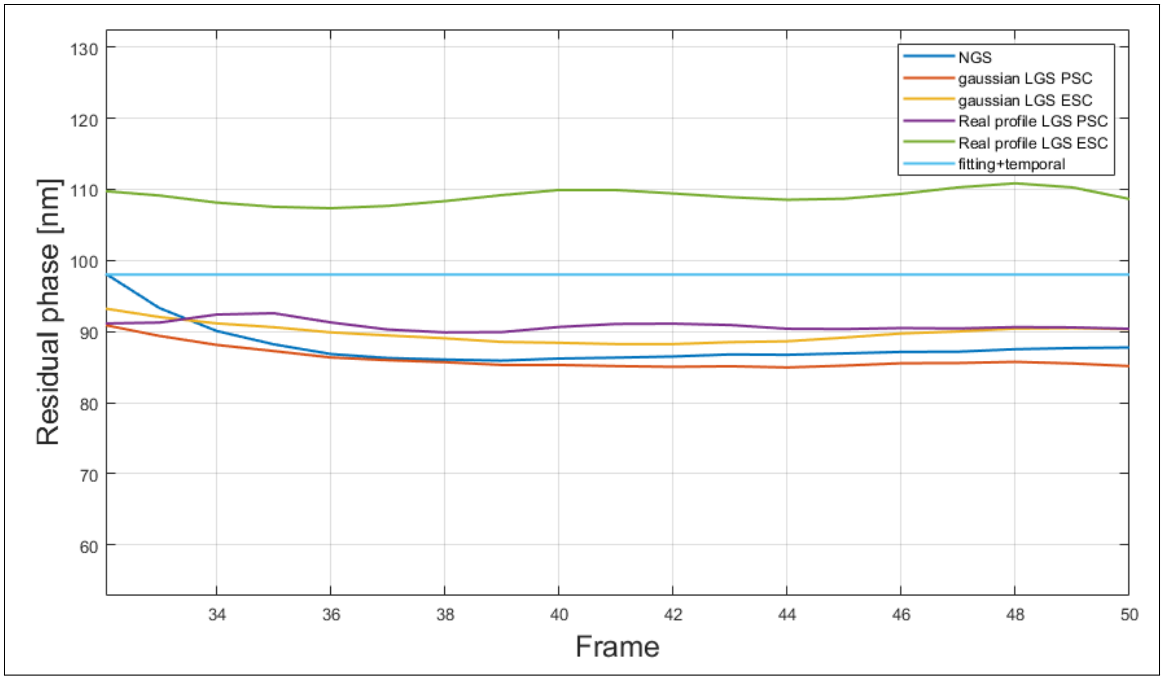

Figure 4.32: Residual phase RMS close up in closed loop for the NGS and the two cases for both LGS for high wind condition.

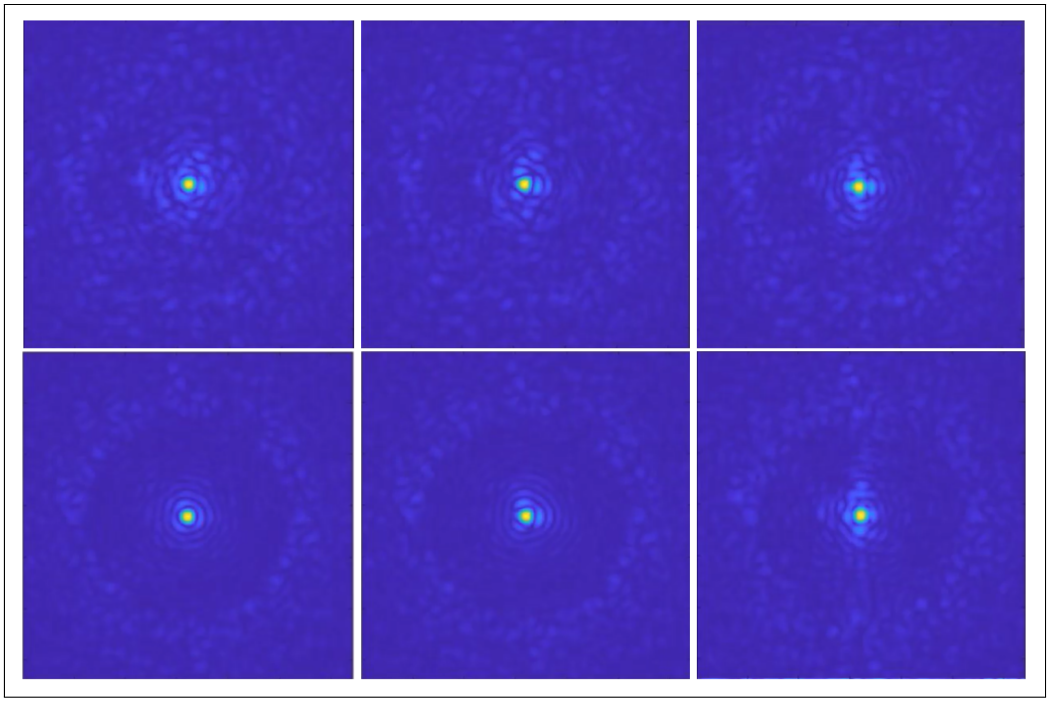

Figure 4.33: **Top row:** Square root scale image of corrected "science" star in high wind condition using point source calibration (and updated optical gains for the LGS'). From left to right the images are for AO systems using NGS, Gaussian LGS and real example profile LGS. **Bottom row:** corresponding image of science star for low wind conditions for comparison

From figure 4.30 it is possible to observe that now the NGS is not the best performing of all the cases, but its behaviour is similar than to the LGS. This can be explained as the NGS may be working in saturated conditions, meaning that its gain is lower. This lower gain in term affects the steady state correction, making it similar to the LGS cases.

The real example profile LGS with elongated source calibration had a strange behaviour, having the lowest SR from all the cases. Reasons for this could not be found, but may have to do with a specific arrange in phase that particularly affects the measurement for that profile of the LGS. Longer simulations can be used to see if this is a persistent effect, or just a coincidence.

From figures 4.31 and 4.32 it is possible to observe that the expected residual phase is similar to the simulated one, with four out of the five cases having a similar behaviour.

Figure 4.33 shows the PFS' obtained for the "science" star for the three most important scenarios in high wind condition and low wind for comparison.

For the AO using NGS (left image in fig. 4.33), Airy disks barely visible, meaning that diffraction might not being achieved. The central spot is well defined, but again speckles might cover the presence of a companion.

For the AO using the Gaussian LGS, Airy disks also barely are visible (center image in fig. 4.33). Whats interesting is that the level of correction is similar to that of the NGS and also the real profile LGS, meaning that here the extra dynamic range of the LGS is compensating for the errors introduced in the measurement, meanwhile for the NGS the saturation acts as a gain less than one, deteriorating the correction for the rapidly changing phase due to the high wind.

Again we see that the loop was successfully closed using the point source calibration for the LGS, reassuring the possibility of updating the optical gains to optimize the reconstructor and allowing the use of PWFS to be used with LGS.

4.4.2 With noise

Similar tests as before where conducted, but this time photon noise was introduced to the system. To do this, different magnitude stars where used as the guide star and the cumulative SR from the run was recorded.

The parameters used for the closed loop with noise were

- Telescope diameter: 8 m
- r_0: 0.15 m
- Field of View for the guide star: 10 x 10 arcsec
- Guide star magnitude range: [5, 17]

With an $r_0 = 0.15\,m$, the fitting error allows for a correction of SR of around 40 %. The results of the closed loop with noise can be observed in figure 4.34

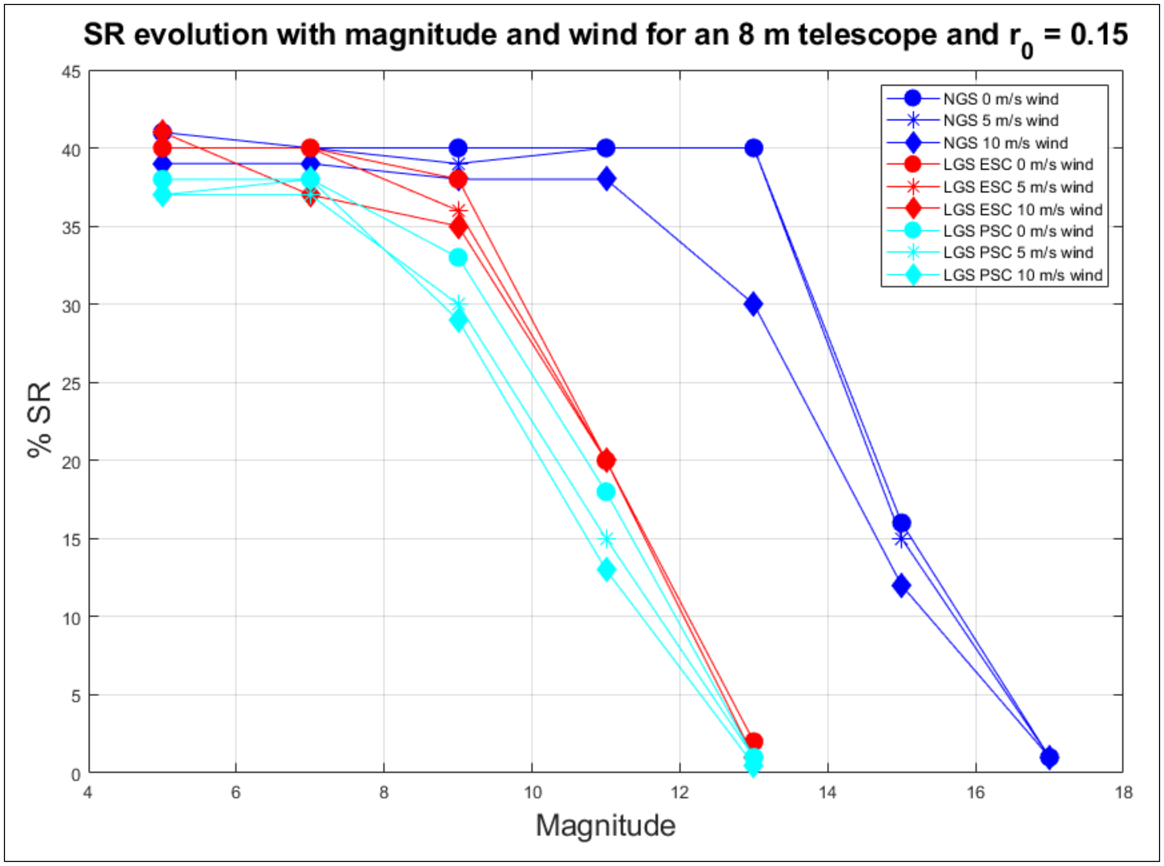

Figure 4.34: SR evolution with magnitude and wind speeds for NGS, LGS with elongated source calibration and LGS with point source calibration.

Looking at figure 4.34 it is possible to observe that for every wind condition and for low magnitude value (near 5) all of the test cases have similar performances. But, as the magnitude of the guide star increases, the LGS starts lowering the quality of the correction before the NGS due to its lower sensitivity to photon noise. Recalling what was obtained in the sensitivity section, an 8 m telescope using a LGS had a lower limiting magnitude (where the SR starts dropping), 4.6 less than when using an NGS. Now, comparing that result with what was obtained in the closed loop operation, it is possible to observe that the difference in limiting magnitude is between 4 and 5, meaning that the prediction using the sensitivity was correct. Extrapolating to a 40 m telescope, the drop in limiting magnitude should be approximately 5.3.

For the Single Conjugate Adaptive Optics (SCAO) system for the Harmoni instrument that will be installed on the ELT, it is expected to have measurements of the wavefront error with an accuracy better than 100 nm at magnitudes less than 12 (using a NGS) (Thatte et al., 2016). If they were to use a LGS, to achieve the same level of correction a 6.7 magnitude source should be used, which may not be feasible.

This loss in sensitivity may be a reason not to use the pyramid wavefront sensor when using LGS for the new generation of extremely large telescopes. Other alternatives should be considered, ideally ones that take into account the 3D nature of the LGS, such as the Ingot wavefront sensor or other tilted alternatives.

5. CONCLUSIONS

5.1 Conclusions

This work presented an extensive study of the performance of the pyramid wavefront sensor using LGS. For this, optical gains were computed, finding that it was possible to go from a point source calibrated interaction matrix to an interaction matrix optimized for reconstructing the signal coming from a LGS. This proves to be very useful, because building a point source calibration unit for a telescope is much easier than building an elongated source calibration, that also takes into account the structure of the sodium layer. The possibility to go from one matrix to another means that is feasible to optimize in real time the reconstructor to the dynamic shape of the elongated spot generated by the LGS.

In terms of linearity, it was found that the NGS can work in linear range much longer than the LGS. This means that for good sky conditions, NGS will have better results than LGS. On the other hand, dynamic range proved to be higher for the LGS, which was expected as the spot elongation acts as a kind of modulation.

If photon noise is considered, NGS have an advantage due to its higher sensitivity. The sensitivity drop for LGS can affect the signal-to-noise ratio in a similar way to an increase in magnitude of a NGS from 4.6 for an 8 m telescope and in the order of 5 for an 40 m one. This effect poses a constraint on the level of correction that can be obtained using a pyramid with LGS.

When performing closed loop operations without noise (or equivalently using a bright source), it was possible to observe that for good sky conditions the NGS performed slightly better than the LGS, but for poorer sky both were similar. Also, it was proven that it is possible to close the loop for a LGS using a complete point source calibration, and that by optimizing the optical gains the level of correction can even be similar to those of obtained with a NGS.

Finally, when photon noise was added to the closed loop, the difference in limiting magnitudes for the LGS and NGS matched the one obtained using the sensitivity analysis. Then, extrapolating the data to a 40 m telescope and using a real instrument's expected performance (Harmoni), this drop in sensitivity meant that a 6.7 magnitude laser guide star was needed to achieve a similar performance, which might not be feasible in reality, meaning that the pyramid wavefront sensor might not be the best alternative for the new generation of extremely large telescopes.

This drop in sensitivity has led other scientists to develop new wavefront sensors specially design to deal with the elongation of the LGS.

5.2 Future work

5.2.1 Convolutional model

The convolutional model (Fauvarque et al., 2019) is an approximation for the computation that allows to obtain the measurement for the pyramid using the convolution of the phase with an impulse response (IR). For this work, I had to propagate every sample of the LGS for every iteration, taking hours or even days to compute some of the graphs. Instead, using the convolutional model it would be necessary to propagate each sample only once, and using the LGS PSF to compute the IR. Then, the measurement of the pyramid can be obtained by convolving the IR with the phase, which can be achieved using only two FFTs, speeding up the computation several thousand times. This was not used in this work because it is not well known if this model works with LGS.

5.2.2 Laboratory tests

Using the *spatial light modulator approach to the LAM/ONERA on-sky pyramid sensor testbed* (LOOPS) (Janin-Potiron et al., 2019) it might be possible to perform laboratory tests using a real glass pyramid. Using a fast tip/tilt mirror, a deformable mirror, and a long exposure of the detector, it is possible to generate the shape of the LGS. This would provide useful information, allowing the cross check with real data.

5.2.3 Other WFS

Another interesting wavefront sensor to study is the Shearing interferometer. As mentioned in the sensitivity section, as the samples of the LGS get further away from the center near the focus layers, sensitivity drops quickly. Using a repeating phase mask, it is possible to generate a translation invariant Fourier filter that acts as a Shearing interferometer. This would recover much of the lost sensitivity. Also, this mask could be tilted to account for the elongation of the LGS, improving the sensitivity even more.

REFERENCES

H. W. Babcock. The Possibility of Compensating Astronomical Seeing. *Publications of the Astronomical Society of the Pacific*, 65(386):229, October 1953. doi: 10.1086/126606.

Celia Blain, Simone Esposito, Alfio Puglisi, Guido Agapito, and Enrico Pinna. Use of laser guide star with pyramid wavefront sensor. In *Adaptive Optics for Extremely Large Telescopes 4–Conference Proceedings*, volume 1, 2015.

Jason CY Chin, Peter Wizinowich, Ed Wetherell, Scott Lilley, Sylvain Cetre, Sam Ragland, Drew Medeiros, Kevin Tsubota, Greg Doppmann, Angel Otarola, et al. Keck ii laser guide star ao system and performance with the toptica/mpbc laser. In *Adaptive Optics Systems V*, volume 9909, page 99090S. International Society for Optics and Photonics, 2016.

R. Conan and C. Correia. Object-oriented Matlab adaptive optics toolbox. In Enrico Marchetti, Laird M. Close, and Jean-Pierre Vran, editors, *Adaptive Optics Systems IV*, volume 9148 of *Society of Photo-Optical Instrumentation Engineers (SPIE) Conference Series*, page 91486C, August 2014. doi: 10.1117/12.2054470.

Carlos M Correia, Olivier Fauvarque, Charlotte Z Bond, Vincent Chambouleyron, Jean-François Sauvage, and Thierry Fusco. Performance limits of adaptive-optics/high-contrast imagers with pyramid wavefront sensors. *Monthly Notices of the Royal Astronomical Society*, 495(4):4380–4391, 2020.

Guang-Ming Dai. Modal compensation of atmospheric turbulence with the use of Zernike polynomials and Karhunen-Loeve functions. *Journal of the Optical Society of America A*, 12(10):2182–2193, October 1995. doi: 10.1364/JOSAA.12.002182.

ESO. Laser guide stars in action — eso españa. `https://www.eso.org/public/spain/images/2017_11_18_upr_IMG_3321-laser-ok-CC/?lang`, 2017. (Accessed on 08/30/2021).

S. Esposito and A. Riccardi. Pyramid Wavefront Sensor behavior in partial correction Adaptive Optic systems. *Astronomy & Astrophysics*, 369:L9–L12, April 2001. doi: 10.1051/0004-6361:20010219.

S. Esposito, G. Agapito, C. Giordano, A. Puglisi, E. Pinna, C. Blain, and C. Bradley. Pyramid wavefront sensing using Laser Guide Star for 8m and ELT class telescopes. In Enrico Marchetti, Laird M. Close, and Jean-Pierre Véran, editors, *Adaptive Optics Systems V*, volume 9909 of *Society of Photo-Optical Instrumentation Engineers (SPIE) Conference Series*, page 99096B, July 2016. doi: 10.1117/12.2234423.

Olivier Fauvarque, Benoit Neichel, Thierry Fusco, Jean-Francois Sauvage, and Orion Girault. General formalism for Fourier-based wave front sensing: application to the pyramid wave front sensors. *Journal of Astronomical Telescopes, Instruments, and Systems*, 3:019001, January 2017. doi: 10.1117/1.JATIS.3.1.019001.

Olivier Fauvarque, Pierre Janin-Potiron, Carlos Correia, Yoann Brûlé, Benoit Neichel, Vincent Chambouleyron, Jean-Francois Sauvage, and Thierry Fusco. Kernel formalism applied to Fourier-based wave-front sensing in presence of residual phases. *Journal of the Optical Society of America A*, 36(7):1241, July 2019. doi: 10.1364/JOSAA.36.001241.

David L Fried. Optical resolution through a randomly inhomogeneous medium for very long and very short exposures. *JOSA*, 56(10):1372–1379, 1966.

David L Fried. Anisoplanatism in adaptive optics. *JOSA*, 72(1):52–61, 1982.

Thierry Fusco, Benoit Neichel, Carlos Correia, Leonardo Blanco, Anne Costille, Kjetil Dohlen, François Rigaut, Edgard Renaud, Anne Bonnefoi, Zibo Ke, et al. A story of errors and bias: The optimization of the lgs wfs for harmoni. In *AO4ELT6*, 2019.

John W Hardy. *Adaptive optics for astronomical telescopes*, volume 16. Oxford University Press on Demand, 1998.

Pierre Janin-Potiron, Vincent Chambouleyron, Lauren Schatz, Olivier Fauvarque, Charlotte Z. Bond, Yannick Abautret, Eduard Muslimov, Kacem El-Hadi, Jean-François Sauvage, Kjetil Dohlen, Benoît Neichel, Carlos M. Correia, and Thierry Fusco. Adaptive optics with programmable Fourier-based wavefront sensors: a spatial light modulator approach to the LAM/ONERA on-sky pyramid sensor testbed. *Journal of Astronomical Telescopes, Instruments, and Systems*, 5:039001, July 2019. doi: 10.1117/1.JATIS.5.3.039001.

A. Kolmogorov. The Local Structure of Turbulence in Incompressible Viscous Fluid for Very Large Reynolds' Numbers. *Akademiia Nauk SSSR Doklady*, 30:301–305, January 1941.

Virendra N. Mahajan. Strehl ratio for primary aberrations in terms of their aberration variance. *Journal of the Optical Society of America (1917-1983)*, 73:860, January 1983.

Daniel Malacara. *Optical shop testing*. 2007.

David Mas, Javier Garcia, Carlos Ferreira, Luis M. Bernardo, and Francisco Marinho. Fast algorithms for free-space diffraction patterns calculation. *Optics Communications*, 164(4-6):233–245, June 1999. doi: 10.1016/S0030-4018(99)00201-1.

NOIRLab. Background information: Laser guide stars — noirlab. `https://noirlab.edu/public/es/images/gemini0504d/`, 2017. (Accessed on 08/30/2021).

Robert J Noll. Zernike polynomials and atmospheric turbulence. *JOsA*, 66(3):207–211, 1976.

H. Nyquist. Certain Topics in Telegraph Transmission Theory. *Transactions of the American Institute of Electrical Engineers*, 47(2):617–624, April 1928. doi: 10.1109/T-AIEE.1928.5055024.

Alexander Mikhailovich Oboukhov. Some specific features of atmospheric tubulence. *Journal of Fluid Mechanics*, 13(1):77–81, 1962.

S. S. Olivier and C. E. Max. Laser guide star adaptive optics: present and future [invited]. In J. G. Robertson and William J. Tango, editors, *Very High Angular Resolution Imaging*, volume 158, page 283, January 1994.

Byoungyoul Park. Development of a low voltage and large stroke mems-based lorentz force continuous deformable polymer mirror system. 2018.

T. Pfrommer and P. Hickson. High resolution mesospheric sodium properties for adaptive optics applications. *Astronomy & Astrophysics*, 565:A102, May 2014. doi: 10.1051/0004-6361/201423460.

E Pinna1a, AT Puglisi, J Argomedo, F Quiros-Pacheco, A Riccardi, and S Esposito. The pyramid wavefront sensor with extended reference source. In *AO4ELT2 Conference*, 2011.

Fernando Quiros-Pacheco, Enrico Pinna, Alfio Puglisi, Lorenzo Busoni, Guido Agapito, Sebastian Rabien, and Simone Esposito. Pyramid wavefront sensor performance with laser guide stars. In Simone Esposito and Luca Fini, editors, *Proceedings of the Third AO4ELT Conference*, page 15, December 2013. doi: 10.12839/AO4ELT3.13138.

Roberto Ragazzoni. Pupil plane wavefront sensing with an oscillating prism. *Journal of Modern Optics*, 43(2):289–293, February 1996. doi: 10.1080/09500349608232742.

Roberto Ragazzoni and J Farinato. Sensitivity of a pyramidic wave front sensor in closed loop adaptive optics. *Astronomy and Astrophysics*, 350:L23–L26, 1999.

Roberto Ragazzoni, Elisa Portaluri, Valentina Viotto, Marco Dima, Maria Bergomi, Federico Biondi, Jacopo Farinato, Elena Carolo, Simonetta Chinellato, Davide Greggio, Marco Gullieuszik, Demetrio Magrin, Luca Marafatto, and Daniele Vassallo. Ingot Laser Guide Stars Wavefront Sensing. *arXiv e-prints*, art. arXiv:1808.03685, August 2018.

Armando Riccardi, N. Bindi, Roberto Ragazzoni, Simone Esposito, and Paolo Stefanini. Laboratory characterization of a Foucault-like wavefront sensor for adaptive optics. In Domenico Bonaccini and Robert K. Tyson, editors, *Adaptive Optical System Technologies*, volume 3353 of *Society of Photo-Optical Instrumentation Engineers (SPIE) Conference Series*, pages 941–951, September 1998. doi: 10.1117/12.321702.

François Roddier. Adaptive optics in astronomy. 1999.

Karl Strehl. Aplanatische und fehlerhafte abbildung im fernrohr. *Zeitschrift für Instrumentenkunde*, 15(7):362–370, 1895.

Valerian Ilich Tatarskii. *Wave Propagation in Turbulent Medium*. 1961.

Niranjan A Thatte, Fraser Clarke, Ian Bryson, Hermine Shnetler, Matthias Tecza, Thierry Fusco, Roland M Bacon, Johan Richard, Evencio Mediavilla, Benoît Neichel, et al. The e-elt first light spectrograph harmoni: capabilities and modes. In *Ground-based and Airborne Instrumentation for Astronomy VI*, volume 9908, page 99081X. International Society for Optics and Photonics, 2016.

Robert K Tyson. *Introduction to adaptive optics*, volume 41. SPIE press, 2000.

Kristina Uhlendorf, Brady Espeland, Rusty Gardhouse, Rodolphe Conan, and Antonin Bouchez. The opto-mechanical design of the LTAO WFS for the Giant Magellan Telescope. In Simone Esposito and Luca Fini, editors, *Proceedings of the Third AO4ELT Conference*, page 10, December 2013. doi: 10.12839/AO4ELT3.12835.

J. P. Veran, F. Rigaut, H. Maitre, and D. Rouan. Estimation of the adaptive optics long-exposure point-spread function using control loop data. *Journal of the Optical Society of America A*, 14(11):3057–3069, November 1997. doi: 10.1364/JOSAA.14.003057.

Theodore von Kármán. Progress in the Statistical Theory of Turbulence. *Proceedings of the National Academy of Science*, 34(11):530–539, November 1948. doi: 10.1073/pnas.34.11.530.

Christophe Vérinaud. On the nature of the measurements provided by a pyramid wavefront sensor. *Optics Communications*, 233(1-3):27–38, March 2004. doi: 10.1016/j.optcom.2004.01.038.

von F. Zernike. Beugungstheorie des schneidenver-fahrens und seiner verbesserten form, der phasenkontrastmethode. *Physica*, 1(7):689–704, May 1934. doi: 10.1016/S0031-8914(34)80259-5.